

MASTER

**Design of an Evaporator/Condenser for a Thermochemical Storage System
An Experimental Investigation on the Influence of Hydrostatic Pressure**

Laumen, N.J.

Award date:
2021

[Link to publication](#)

Disclaimer

This document contains a student thesis (bachelor's or master's), as authored by a student at Eindhoven University of Technology. Student theses are made available in the TU/e repository upon obtaining the required degree. The grade received is not published on the document as presented in the repository. The required complexity or quality of research of student theses may vary by program, and the required minimum study period may vary in duration.

General rights

Copyright and moral rights for the publications made accessible in the public portal are retained by the authors and/or other copyright owners and it is a condition of accessing publications that users recognise and abide by the legal requirements associated with these rights.

- Users may download and print one copy of any publication from the public portal for the purpose of private study or research.
- You may not further distribute the material or use it for any profit-making activity or commercial gain

De Beijer RTB B.V.



TU/e EINDHOVEN
UNIVERSITY OF
TECHNOLOGY

**Design of an Evaporator/Condenser for a
Thermochemical Storage System:
An Experimental Investigation on the Influence
of Hydrostatic Pressure**

written by

N.J. Laumen
0999222

A thesis submitted in partial fulfilment of the requirements for the degree of

Master of Science
(*M. Sc.*)

in the discipline of
Mechanical Engineering

submitted on 20th of May 2021 to the
Energy Technology Group within the
Department of Mechanical Engineering of
Eindhoven University of Technology

Thesis Supervisor: dr. ir. C.C.M. Rindt
Company Supervisor: H.A. De Beijer

Abstract

Closed thermochemical storage has great potential to be implemented in high energy density heat storage systems. A surplus of renewable energy can be stored in closed thermochemical storage for times of renewable energy scarcity. The discharge of the TCS system is fully dependent on the evaporator performance of the heat exchanger in the liquid absorbate. The energy density of the system is determined by the amount of reactants: absorbent and absorbate, that can be fitted in a volume. Under subatmospheric conditions a liquid column creates a hydrostatic head which induces a non-negligible pressure gradient in the fluid. In this thesis, the influence of the hydrostatic pressure on evaporation performance of water in a subatmospheric thermochemical energy storage framework is researched. This was done in using an experimental setup. This setup consisted out of a transparent vacuum chamber in which two different heat exchangers were tested on their boiling performance for various initial water heights. The measurement data in combination with the observations concluded that the boiling behaviour in a single experiment is very different at the start than later in time. Two distinct boiling regimes were detected and the influence of the water column height on each regime was analysed on its own. The results suggest that increasing the water height increases the heat exchanger power but decreases the average heat flux. Experiments conducted with a heat exchanger with larger surface area resulted in an improvement of the power and a worsening of the heat flux. The hydrostatic pressure acts as a barrier for vapor bubble formation, from a certain depth onward no nucleate pool boiling is observed. Increasing the surface area of the heat exchanger does not influence the position of this barrier.

Acknowledgments

I first would like to thank the Eindhoven University of Technology for providing me with the relevant knowledge and tools during my bachelor and master. The skills obtained during my academic education allowed me to face and tackle the challenges encountered during the course of this graduation project. I would especially like to thank my thesis supervisor Camilo Rindt for his guidance in this project. I appreciate the amount of freedom I have been given, when it comes to the direction of the research and I am thankful for the amount of critical feedback I have received during the meetings. I would also like to say a word of thanks to Cees van der Geld, who made time to discuss the research approach and experimental results with me, despite already being retired.

My gratitude goes out to the people working at De Beijer RTB BV. In a short time span I have learnt a great deal in an innovative and collegiate environment. I had a pleasant time and will not soon forget my experience in Duiven. I want to thank my company supervisor Henk de Beijer in particular, not only for his advise and support on the topic of my research, but also for helping me to better understand the reality of innovation, product development and the energy transition. Also a word of thanks to Erik Veenstra, who helped me greatly with the construction of the evaporator test chamber.

I also want to thank my friends. Even though they have not helped me with any of the content in this thesis, they consciously and unconsciously helped me clear my mind at times when my thoughts were stuck on the research subject. This often benefited the progress of the graduation project.

Above all, I want to thank my parents for all the support I have received from them during my academic carrier. They have motivated me to take steps in life, I would not have made on my own. Thank you for always believing in me.

Niek Laumen
Sint Joost, May 2021

List of Tables

| | | |
|-----|---|----|
| 4.1 | The set values for flow (\dot{V}) and inlet temperature (T_{in}) and the maximum observed fluctuations during all experiments | 28 |
| 4.2 | List of measurement devices used in the experimental phase, including their operating range | 29 |
| 4.3 | Measurement devices with their maximum random error and the standard deviation of the random error based on the calibration data | 31 |
| B.1 | Results of the numerical stress study compared to the yield stress per part . . . | 75 |

List of Figures

| | | |
|------|---|----|
| 1.1 | Typical household energy consumption and solar irradiation over a year in the Netherlands [7] | 1 |
| 3.1 | Equilibrium curves for different materials, the dotted horizontal resembles atmospheric pressure [15] | 6 |
| 3.2 | Pressure against temperature plot of charging and discharging for a TCS system with a schematic heat flows in system during the two cycles [16] [17] | 7 |
| 3.3 | Schematic drawing of the MODESTORE set-up [19] | 8 |
| 3.4 | Pressure against temperature phase diagram for most substances. With the equilibrium lines between solid and gaseous phase (red), between solid and liquid phase (green) and between liquid and gaseous phase (blue) [23] | 10 |
| 3.5 | A double logarithmic plot of the pressure against the specific volume during phase change between liquid and vapor. With an isothermal line in red and the saturation curve of water in black [24]. | 11 |
| 3.6 | Visualization of bubble formation at nucleation site [27] | 12 |
| 3.7 | Change in Gibbs free energy as a function of the bubble radius (green), with the contribution due to the surface (red) and due to the volume (blue) [29] | 13 |
| 3.8 | Pool boiling curve for saturated water at atmospheric pressure [32] | 14 |
| 3.9 | Different types of vapor bubble formation for the regimes in Figure 3.8 [33] | 15 |
| 3.10 | Snapshots of vapor bubble formation process: above under subatmospheric conditions (5.6 <i>kPa</i>), below under atmospheric conditions (101.4 <i>kPa</i>) [36] | 15 |
| 3.11 | Experimental pool boiling curves obtained with a water height of 20 <i>cm</i> for 100 <i>kPa</i> , 15 <i>kPa</i> , 4.2 <i>kPa</i> and 1.2 <i>kPa</i> [37] | 16 |
| 3.12 | Influence of contact angel on the droplet shape [44] | 18 |
| 3.13 | Influence of column height on the pressure (blue) and saturation temperature (red) for $T = 20^{\circ}\text{C}$ at the water surface | 19 |
| 3.14 | Experimental apparatus used in the research of Wojtasik et al. [11] | 20 |
| 3.15 | Boiling regime maps for vapor pressures of 2.4 <i>kPa</i> and 3.1 <i>kPa</i> [11] | 21 |
| 4.1 | Schematic drawing of the experimental setup, including a legend. The thick arrows represent the water flow: the in and outflow of the evaporator (red), the in and outflow of the condenser (blue) and flow of the condensed water to the water collection vessel (black). The thin lines represent the gaseous flow. The lines with the square end represent thermocouples, which measure the water temperature at different heights | 24 |
| 4.2 | Technical drawing of the cylindrical vessel which will be used for the test chamber. The different couplings are denoted by different letters. The dimensions are in millimeters. | 25 |
| 4.3 | Shape of the copper heat exchanger which is installed in the cylindrical vessel. In the red circles the 15x10 <i>mm</i> reducers and in the blue circle the solder fitting. | 25 |
| 4.4 | The water collection vessel (in the red dotted square) connected to the condenser (during experimentation) and to the evaporator (between experiments) | 27 |

| | | |
|------|---|----|
| 4.5 | A typical measurement of the water height: The underside of the spirit level needs to align with the water level, the spirit level also needs to be level, which is indicated by the bubble near the hand. The height is measured at the intersection between the ruler and the underside of the spirit level. | 29 |
| 4.6 | The calibration line for one thermocouple: on the x-axis the temperature measured by the thermocouple which requires calibration and on the y-axis the temperature determined by a certified measurement device. In blue the data points and in red the regression line through these points. | 30 |
| 4.7 | Random error for all thermocouples within the temperature range of the experiments. | 31 |
| 4.8 | Relation between the height and the contact area between heat exchanger and water | 32 |
| 4.9 | The confidence intervals for experiment data. The thicker lines are the upper and lower bound which denote the boundaries of the 95% confidence intervals. | 34 |
| 5.1 | Measured pressures in the evaporator (blue) and the condenser (red) during an experiment with $z_{start} = 19cm$ | 35 |
| 5.2 | Temperature development during two experiments with different initial water heights | 36 |
| 5.3 | The development of the powers during a experiment with $z_{start} = 19cm$ | 37 |
| 5.4 | Three snapshots of the boiling behaviour at the surface, linked to the power curve of Figure 5.3 (a). A: the valve is still closed, each chamber is at its own steady state, negligible heat transfer and no boiling, B: the bath is in the process of cooling, violent bubble formation everywhere on the water surface. C: the bath has reached a steady state temperature, only bubble formation on the heat exchanger surface. | 38 |
| 5.5 | Measured powers in the evaporator (blue), the condenser (red) and the power due to water cooling (yellow) during two experiments with different starting heights. The border between transient and steady regime is given by the black dotted line in both figures. | 39 |
| 5.6 | Contour map of how the power subtracted from the water, during the transient regime of the experiment, is related to the pressure difference between evaporator and condenser and the water height. | 40 |
| 5.7 | Contour maps of the heat exchanger performance variables plotted against the pressure difference between evaporator and condenser and the water height. | 40 |
| 5.8 | Relation between the magnitude of the heat exchanger performance variables and the water height in the steady regime of the experiment. The error bars are chosen to fit 95% of the data distribution. | 41 |
| 5.9 | The steady regime heat exchanger power as a function of water height. In black the experiment results already seen in Figure 5.8 (a) and in red the experiments for the reversed flow direction. | 42 |
| 5.10 | Left: a top view of the spiral heat exchanger. Right: a side view of the spiral heat exchanger. | 44 |
| 5.11 | Contour maps of the transient regime for the experiment with the new heat exchanger. The magnitude of power from the water and heat exchanger power is plotted against the pressure difference between evaporator and condenser and the water height. | 45 |

| | | |
|------|--|----|
| 5.12 | The heat exchanger power of the larger heat exchanger, during the steady regime of the experiment, as a function of the water height. The error bars chosen to fit a 95% of the data distribution. | 46 |
| 5.13 | Snapshot of two experiments: In the green dotted square the observed vapor bubble formation, in the blue circle the thermocouples at the heights where bubble formation is observed, in the red circle the thermocouples at the height where no bubble formation is observed and in the white cross the thermocouples of which the measurements are not included in Figure 5.14. | 47 |
| 5.14 | Boiling regime curves: with nucleate pool boiling represented by the blue data points and no bubble formation was observed by the red points. | 48 |
| 6.1 | Geometry and boundaries of the existing numerical reactor model [59] | 51 |
| 6.2 | Schematic drawing which represents the numerical model. The red arrows represent heat transfer and the green arrows represent mass transfer. The pink dotted square represents the part which will eventually be replaced by the existing numerical reactor. | 53 |
| 6.3 | Schematic enthalpy diagram of the condenser vapor phase during one numerical time step, assuming that $m_{g,c}(t) = m_{g,c}(t + \Delta t)$ for simplicity | 55 |
| 6.4 | Numerical conservation plots: on the left the power as a function of time on the right the masses as a function of time. The blue lines in both figures is the sum of all components. | 56 |
| 6.5 | The total power output which is outputted at the condenser as a function of time. In blue the numerical computation and in red the experiment result. | 57 |
| 6.6 | Numerical validation plots: on the left the calculated against the measured pressures and on the right the calculated against the measured temperatures. | 58 |
| 6.7 | Numerical calculation of the water vapor inlet boundary condition values for respectively the vapor pressure, vapor temperature and vapor concentration in time. These relations are for an evaporator connected to a condenser. The response will be different when when the evaporator is connected to a reactor. | 59 |
| A.1 | Vapor bubble formation under the hose clamp. The time difference between the frames is 50 milliseconds. | 69 |
| A.2 | Picture of the old condenser connected to the setup | 70 |
| A.3 | Picture of the new condenser connected to the setup | 70 |
| A.4 | Figure of the pressure development in the evaporator (solid line) and condenser (dashed line) when the valve is opened. The old configuration is given in blue and the new configuration in red. This data is collected with for the situation where $T_{in} = 30\text{ }^{\circ}\text{C}$ and $z_{start} = 16.9\text{ cm}$ | 71 |
| A.5 | ArmaFlex-isolation applied to the outer surface and edges of the condenser and vapor connection. Compare to Figure A.3 to see the difference with the previous situation. | 72 |
| B.1 | Assembly with realistic colours | 74 |
| B.2 | Mesh of the assembly | 74 |
| B.3 | Surface plot of displacement top view | 76 |
| B.4 | Side view of deformation (scale: 39:1) | 76 |
| B.5 | Stress distribution on bottom ring | 76 |
| B.6 | Stress distribution on top ring | 76 |
| B.7 | Strain under PMMA plate | 76 |
| B.8 | Stress under PMMA plate | 76 |

| | | |
|-----|--|----|
| C.1 | Picture of the heat exchanger mounted in the vessel | 77 |
| C.2 | Black and white image of the heat exchanger, made using photo editing software | 77 |
| C.3 | Above: the binary image of the heat exchanger. Below: the summation of the white pixels in y-direction per pixel in x-direction. | 78 |
| C.4 | Scaled area distribution of the overlapping area (blue) and the visible area (red). The sum of the two gives the real area. | 79 |
| C.5 | Area vs height curves for all 8 images. The curves are all shifted slightly to better match the average peak locations | 81 |
| C.6 | Shows the final curve for surface area distribution against the height | 81 |
| D.1 | Power distribution for $z_{start} = 6.6cm$ | 84 |
| D.2 | Power distribution for $z_{start} = 8.5cm$ | 84 |
| D.3 | Power distribution for $z_{start} = 15.3cm$ | 84 |
| D.4 | Power distribution for $z_{start} = 16.9cm$ | 84 |
| D.5 | Power distribution for $z_{start} = 19.0cm$ | 85 |
| D.6 | Power distribution for $z_{start} = 23.4cm$ | 85 |
| D.7 | Power distribution for $z_{start} = 24.2cm$ | 85 |
| D.8 | Power distribution for $z_{start} = 26.7cm$ | 85 |
| E.1 | Experimental data for the pressure difference between evaporator and condenser in blue. In red the average pressure difference in the steady regime. | 87 |
| E.2 | Numerical results for the output power with different values for β_e , with in black the experimental result. | 88 |
| E.3 | Numerical results for the evaporator pressure with different values for τ , with in black the experimental result | 88 |

Nomenclature

Latin symbols

| Symbol | Unit | Description |
|-----------|---------------------------------|--------------------------------------|
| A | m^2 | area |
| c | $mol \cdot m^{-3}$ | concentration |
| c_p | $J \cdot kg^{-1} \cdot K^{-1}$ | specific heat capacity |
| D | m | diameter |
| E | J | energy |
| G | J | Gibbs free energy |
| h | $J \cdot kg^{-1}$ | specific enthalpy |
| h'' | $W \cdot m^{-2} \cdot K^{-1}$ | heat transfer coefficient |
| H | $J \cdot kg^{-1}$ | enthalpy |
| H_m | $J \cdot mol^{-1}$ | molar enthalpy |
| L | m | length |
| m | kg | mass |
| N | – | population |
| p | Pa | pressure |
| P | W | power |
| q'' | $W \cdot m^{-2}$ | heat flux |
| Q | J | heat |
| R | m | radius of curvature |
| Ra | m | arithmetic average surface roughness |
| S | $J \cdot mol^{-1} \cdot K^{-1}$ | entropy |
| t | s | time |
| T | K | temperature |
| v | $m^3 \cdot kg^{-1}$ | specific volume |
| V | m^3 | volume |
| \dot{V} | $m^3 \cdot s^{-1}$ | volumetric flow rate |
| z | m | height |

Greek symbols

| Symbol | Unit | Description |
|------------|------------------------------|---|
| α | – | volume fraction |
| β | $m^3 \cdot s^{-1}$ | volumetric mass transfer intensity factor |
| γ | $N \cdot m^{-1}$ | surface tension |
| ϵ | <i>same as measured unit</i> | absolute error |
| θ | $^\circ$ | contact angle |
| ρ | $kg \cdot m^{-3}$ | density |
| σ | $N \cdot m^{-2}$ | stress |
| τ | s | relaxation time |

Dimensionless numbers

Ja = Jakob number

Constants

| Symbol | Value | Unit | Description |
|--------|--------|---------------------------------|--------------------------------|
| g | 9.81 | $m \cdot s^{-2}$ | gravitational acceleration |
| R_u | 8.31 | $J \cdot mol^{-1} \cdot K^{-1}$ | universal gas constant |
| R_w | 461.52 | $J \cdot kg^{-1} \cdot K^{-1}$ | specific gas constant of water |

Subscripts

0 = reference

c = condensation

con = condenser

$crit$ = critical

dif = difference

e = evaporation

eva = evaporator

eq = equilibrium

ex = excess

g = gaseous state

i = index

l = liquid state

lv = liquid vapor interface

s = surface

sat = saturation

sl = solid liquid interface

sv = solid vapor interface

vm = von Mises

y = yield

List of abbreviations

CHF = critical heat flux

FEA = finite element analysis

SD = standard deviation

TCM = thermochemical material

TCS = thermochemical storage

TES = thermal energy storage

Contents

| | |
|---|------------|
| Abstract | iii |
| Acknowledgments | v |
| Contents | xv |
| 1 Introduction | 1 |
| 2 Research approach and hypothesis | 3 |
| 3 Review of fundamentals and literature | 5 |
| 3.1 Theory of thermochemical energy storage | 5 |
| 3.1.1 Principle of thermochemical energy storage | 5 |
| 3.1.2 TCS systems | 6 |
| 3.2 Current technological state of closed thermochemical energy storage | 8 |
| 3.3 Phase transition | 9 |
| 3.4 Boiling | 10 |
| 3.4.1 Bubble formation | 10 |
| 3.4.2 Pool boiling | 13 |
| 3.4.3 Boiling under subatmospheric conditions | 15 |
| 3.5 Condensation | 17 |
| 3.6 Influence of hydrostatic pressure | 18 |
| 4 Experimental methodology | 23 |
| 4.1 Experiment choices | 23 |
| 4.2 Experimental setup | 24 |
| 4.2.1 Parts, connections and placement of sensors | 24 |
| 4.2.2 Design of the evaporator test chamber | 24 |
| 4.3 Experiment procedure | 26 |
| 4.3.1 Before and between experiments | 26 |
| 4.3.2 During experiments | 28 |
| 4.4 Measurement techniques | 29 |
| 4.4.1 Measurement devices | 29 |
| 4.4.2 Calibration and error estimation | 30 |
| 4.5 Data conversion | 32 |
| 4.6 Error analysis | 33 |
| 5 Results | 35 |
| 5.1 Typical system behaviour | 35 |
| 5.2 Influence of hydrostatic pressure | 39 |
| 5.2.1 Transient evaporation regime | 39 |
| 5.2.2 Steady evaporation regime | 41 |
| 5.3 Improving evaporation behaviour | 43 |
| 5.3.1 New heat exchanger | 43 |

| | | |
|----------|---|-----------|
| 5.3.2 | Typical system behaviour compared to old heat exchanger | 44 |
| 5.3.3 | Transient evaporation regime | 45 |
| 5.3.4 | Steady evaporation regime | 46 |
| 5.4 | Boiling regimes | 47 |
| 6 | Water vapor inlet boundary condition for numerical reactor model | 51 |
| 6.1 | Background | 51 |
| 6.2 | Model implementation and assumptions | 52 |
| 6.2.1 | Assumptions | 52 |
| 6.2.2 | Model implementation | 52 |
| 6.3 | Numerical results validation | 56 |
| 6.3.1 | Energy and mass conservation | 56 |
| 6.3.2 | Validation with experimental data | 57 |
| 6.4 | Influence of boundary condition | 59 |
| 7 | Conclusion and Recommendations | 61 |
| 7.1 | Conclusions | 61 |
| 7.2 | Recommendations | 62 |
| | Bibliography | 63 |
| A | Experimental setup improvements | 69 |
| A.1 | Hose clamp attachment of thermocouples | 69 |
| A.2 | Upgrading the condenser | 70 |
| A.3 | Additional isolation of the condenser | 72 |
| B | Finite Element Analysis of PMMA plate configuration | 73 |
| B.1 | 3D Model | 73 |
| B.2 | Problem formulation & Assumptions | 73 |
| B.3 | Results & Conclusion | 74 |
| C | Heat exchanger area model | 77 |
| C.1 | Preprocessing | 77 |
| C.2 | Converting image in data | 78 |
| C.3 | Combining multiple data sets | 80 |
| D | Distributions of evaporator power | 83 |
| E | Influence of approximated parameters on numerical model | 87 |
| E.1 | Pressure difference | 87 |
| E.2 | Mass transfer intensity factor | 87 |
| E.3 | Relaxation time | 88 |
| F | Declaration concerning the TU/e Code of Scientific Conduct | 89 |

Global warming is a threat to the world as we know it. It will cause drought, rising sea levels and increase the frequency of extreme weather events [1], [2]. Global warming will effect entire ecosystems, bringing water and food supply in danger and increase the changes of natural disasters [3], [4]. It is a scientific consensus that carbon emissions contribute to the increase of the earths temperature [5]. To reduce the effects of global warming, countries and international organisations are closing agreements to cut CO₂-emissions. To achieve this goal, fossil based energy production must make way for sustainable energy sources, which bring along huge challenges.

Domestic buildings in the Netherlands hugely rely on natural gas for space heating and hot water purposes. In 2019, 70% of the Dutch domestic energy demand was fulfilled by natural gas [6]. Implementing solar heating systems for domestic heating purposes would decarbonize the Dutch energy grid greatly. The main downside of solar heating systems is that there are daily and seasonal mismatches between energy production and energy consumption. The seasonal mismatch is visualized in Figure 1.1. In the darker and colder months more energy is consumed than can be produced, but in the summer a surplus of energy is available. Thermal energy storage (TES) is needed to have fossil free heat all year round. TES can be subdivided in three groups: sensible storage, latent storage and thermochemical storage (TCS).

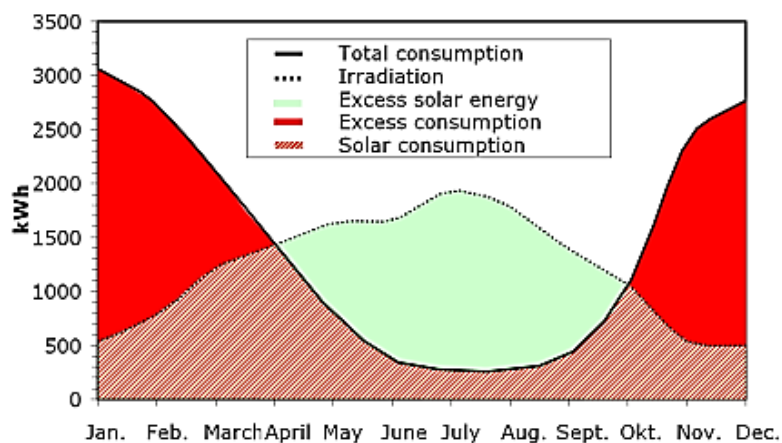


Figure 1.1: Typical household energy consumption and solar irradiation over a year in the Netherlands [7]

TCS, which stores energy in a reversible hydration reaction, has great advantages compared to sensible and latent storage. The effective energy density for storage in thermochemical material (TCM) can be up to $2 \text{ GJ}/\text{m}^3$. This is much higher than the energy densities for sensible and latent storage, which have a maximum of 0.25 and $0.6 \text{ GJ}/\text{m}^3$ respectively [8]. Another advantage is that TCM can store heat for a relative long time. Its storage time is long enough to capture seasonal effects. For sensible and latent storage, the storage time is in the range of several days [9]. Another advantage is that TCS can be used for both domestic heating and cooling, which is impossible for sensible and latent storage.

De Beijer RTB BV is a Dutch research and development company, located in Duiven. The company is developing a closed thermochemical storage system intended for fulfilling the heating and cooling demand of the built environment. The system is under vacuum, which means that the hydration and dehydration of the absorbent in the reactor, as well as the evaporation and condensation of the absorbate, occur under subatmospheric pressures.

In a vacuum the saturation temperature drops, which means water can boil at much lower temperatures than 100°C . However, subatmospheric boiling brings along additional challenges. Existing models based on boiling at higher pressures cannot be extrapolated to predict phase transitions at subatmospheric pressures [10]. At low pressure a relative small column height of liquid can induce a hydrostatic pressure in the same order of magnitude as the vapor pressure [11]. The pressure gradient over the water height under subatmospheric conditions becomes non-negligible, in contrast to the pressure gradient under atmospheric conditions. The pressure gradient due to the water column will cause the saturation temperature of the water to increase. To build a compact TCS system with a competitive energy capacity, compared to existing energy storage systems, a significant amount of column height of liquid absorbate in the evaporator is unavoidable.

Studying the influence of the hydrostatic pressure on evaporation under subatmospheric conditions is essential, for the eventual design of the evaporator/condenser in a thermochemical energy storage system. This thesis will focus on experimental research in order to obtain a relation between hydrostatic pressure and evaporation in a closed thermochemical storage system framework. Also a way to reduce the negative effect water height will have on boiling is investigated. Another goal of this thesis is to obtain a better understanding of the phenomena occurring during subatmospheric boiling in general. From the experimental results and observations a lot more insight is obtained, which could be used to substantiate design choices for the eventual evaporator/condenser for the TCS system.

2

Research approach and hypothesis

The aim of this research is to better understand the effect of hydrostatic pressure on subatmospheric boiling in order to improve the performance of the evaporator/condenser in a closed thermochemical storage system.

It is already known that an increased hydrostatic pressure will increase the required amount of excess temperature needed. This will therefore reduce the amount of power per surface area, which can be used for evaporation. It is important that this relation is quantified. The main aim and research question of this thesis is:

How does the hydrostatic pressure relate to the boiling performance in a subatmospheric thermochemical storage system setting?

To answer this question experimental research needs to be done. An experimental setup will be built, which will study the impact of the hydrostatic pressure in a thermochemical storage system on a fundamental level. The setup will be constructed in such a way that the boiling process can be visualized. It is expected that visualizations accompanied with measurement data will give great insight in the phenomena, which are occurring during steam production.

With the obtained data from the experiments combined with the knowledge from fundamentals and recent literature recommendations can be done for the evaporator/condenser in a subatmospheric TCS system. Additional experiments can be done to prove if whether these recommendations deliver the desired result. This will give an answer to the secondary question of this thesis:

How can the negative effect of hydrostatic pressure be reduced to improve the boiling performance of the evaporator/condenser in a subatmospheric thermochemical storage system?

The hydrostatic pressure is not the only aspect influencing the boiling performance. It is already known from literature, that the heat transfer of heat exchangers during evaporation is influenced by multiple effects. One can think of dropwise evaporation, splashing effects, flashing and many more. It is important that these effects are captured during the experiments. Linking the observations to the measured data can obtain new insights, which can be used to make design choices for the final evaporator/condenser. Therefore analysing and substantiating the phenomena occurring during subatmospheric boiling in the TCS system framework on a more fundamental level is also part of this thesis.

On the basis of the literature and theory review, which will be presented in [chapter 3](#), a hypothesis can be formed on the influence of the hydrostatic pressure on the boiling performance in a subatmospheric thermochemical storage system setting. It is expected that the boiling behaviour will vary over the water height. Since the temperature difference between wall and bath and the absolute pressure will vary over the heat exchanger surface. It is possible that multiple boiling regimes can coexist in the test space. It is expected that near the water surface, where the static pressure is low and thus excess temperature high boiling will occur on the heat exchanger surface. While lower on the heat exchanger surface, the static pressure might be so high that only heat transfer via convection will take place.

3

Review of fundamentals and literature

3.1 Theory of thermochemical energy storage

This section will describe the physical principles which make TCS possible and the components which are needed to create a functioning TCS system.

3.1.1 Principle of thermochemical energy storage

In thermochemical storage heat is stored making use of a reversible sorption reaction. All of these reactions can be written as the general reaction shown in [Equation 3.1](#).

The reaction given in [Equation 3.1](#) could either be an absorption or an adsorption reaction. In absorption the absorbate is being retained by the absorbent [12]. The absorbate is incorporated in the absorbent, changing its structure. An example of an absorption reaction is the hydration reaction of a salt. In adsorption the adsorbate attaches to the adsorbent surface due to cohesive forces. A thin layer of adsorbate molecules surround the adsorbent molecule, but the structure of the adsorbent molecule stays unaltered [13]. An example of an adsorption reaction is the hydration reaction of zeolite. An absorption reaction has a higher energy density than an adsorption reaction due to stronger bonding forces. Absorption in general takes up more absorbate molecules per absorbent molecule, compared to adsorption [14]. From now on this thesis will focus on TCS systems relying on an absorption reaction, since this is the type of system *De Beijer RTB BV* is developing.



In [Equation 3.1](#), A is called the absorbent and B is the absorbate. When A and B react heat is released, because A and B separated have a higher energy level than AB. A is therefore called the charged absorbent and AB the discharged absorbent. The separation of AB is the charging process and the formation of AB the discharging process. Whether the charging or discharging reaction occurs is determined by the temperature and the availability of reactants. If AB is heated above the equilibrium temperature separation will occur. If the mixture is then cooled below the equilibrium temperature the recombination reaction will occur. This can be prevented by storing A and B separated from each other.

To reduce the storage volume the absorbate is condensed most of the times, like visualized in [Equation 3.2](#). The condensation heat is then released to the surroundings. When the absorbent needs to be discharged, the liquid absorbate needs to be evaporated making use of an external heat source. The discharge reaction could also occur when the absorbate is in a liquid state, but this is undesired. Absorbing a liquid instead of a gas would reduce the produced heat significantly because lots of energy would be needed to break up the liquid bonds between the absorbate molecules.



The equilibrium temperature of the reaction between absorbent and absorbate is of great importance for the functioning of a thermochemical heat storage system. The equilibrium temperature is a function of the pressure and can be calculated using Equation 3.3. This relation is based on the Clausius–Clapeyron relation using the assumption that the vapor behaves as an ideal gas.

$$T_{eq} = \frac{\Delta H_m}{\Delta S_0 - R_u \ln \frac{p}{p_0}} \quad (3.3)$$

With T_{eq} the equilibrium temperature (K), ΔH_m the molar enthalpy difference in this case between reaction products and reactants (J/mol), ΔS_0 the entropy difference caused by the reactions at the reference pressure (J/molK), R_u the universal gas constant (J/molK), p the system pressure (Pa) and p_0 the reference pressure (Pa).

Equation 3.3 also applies for the evaporation-condensation reaction of the absorbate (in Equation 3.2). In that case ΔH_m is the enthalpy of vaporization (J/mol) and ΔS_0 is the entropy of vaporization (J/mol/K). Equation 3.3 makes it possible to express the equilibrium pressure as a function of the vapor pressure. The pressure dependency of the equilibrium temperature is plotted in Figure 3.1 for a couple of different substances. These graphs are also called equilibrium curves. In Figure 3.1 it can be seen that water boils at 100°C at atmospheric pressure (intersection with the dotted horizontal line). By reducing the vapor pressure the boiling temperature will go down.

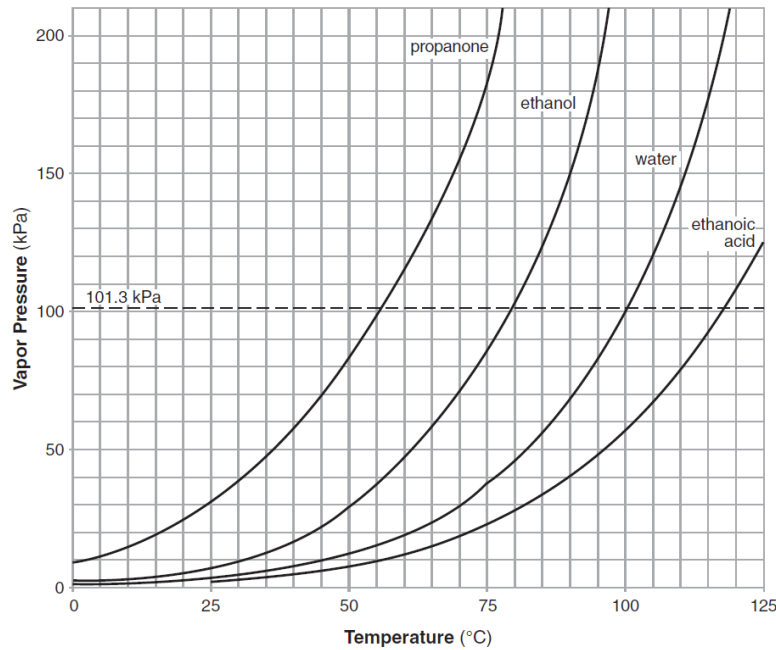


Figure 3.1: Equilibrium curves for different materials, the dotted horizontal resembles atmospheric pressure [15]

3.1.2 TCS systems

The storage systems can be divided into two categories: open systems and closed systems. Open systems are in direct contact with the environment, because of this the system operates at ambient pressure. The absorbate is also restricted, since it must be a gas already present in the

air, so water vapor. The large amount of inert gas present in the air does not contribute to the reaction, but contributes to the mass that needs to be heated. This will decrease the effective temperature difference, which can be achieved. In a close system on the other hand the selection of the absorbate is not restricted. The system could for instance also operate on ammonia or methanol. All other gasses are removed from the system, so the operation pressures of the system are determined by the vapor pressure of the chosen absorbate. The difference in vapor pressures caused by temperature differences within the system governs the transport of the absorbate vapor. The reaction power will be higher for a closed system. Also no mass transfer with the environment takes place which means no additional safety requirements need to be met [9]. Because of the previously named reasons a closed system is preferred for domestic implementation.

The left side of Figure 3.2 shows a typical charging and discharging cycle, visualized in a pressure against temperature plot. The arrows at the line intersections represent the heat flows. The pressure is on a logarithmic axis, which makes the equilibrium lines like those in Figure 3.1 appear straight. On the right side of Figure 3.2 the same heat flows are visualized in the system cycles. During charging, or in other words: during the regeneration cycle, the absorbate is separated from the absorbent at the red arrow Q_{in} . Due to the pressure difference vapor is transported to the condenser. Here the energy Q_{out} is subtracted, causing the vapor to condense. The absorbate loses energy via condensation and moves down the equilibrium line (blue dotted line), the pressure lowers and the temperature decreases. When the TCM needs to be discharged, also called the working cycle, heat is supplied to the evaporator at the blue arrow Q_{in} . The evaporated absorbate is transported to the absorbent due to the difference in pressure. The absorbate discharges and the heat $Q_{heating}$ is released at the yellow arrow.

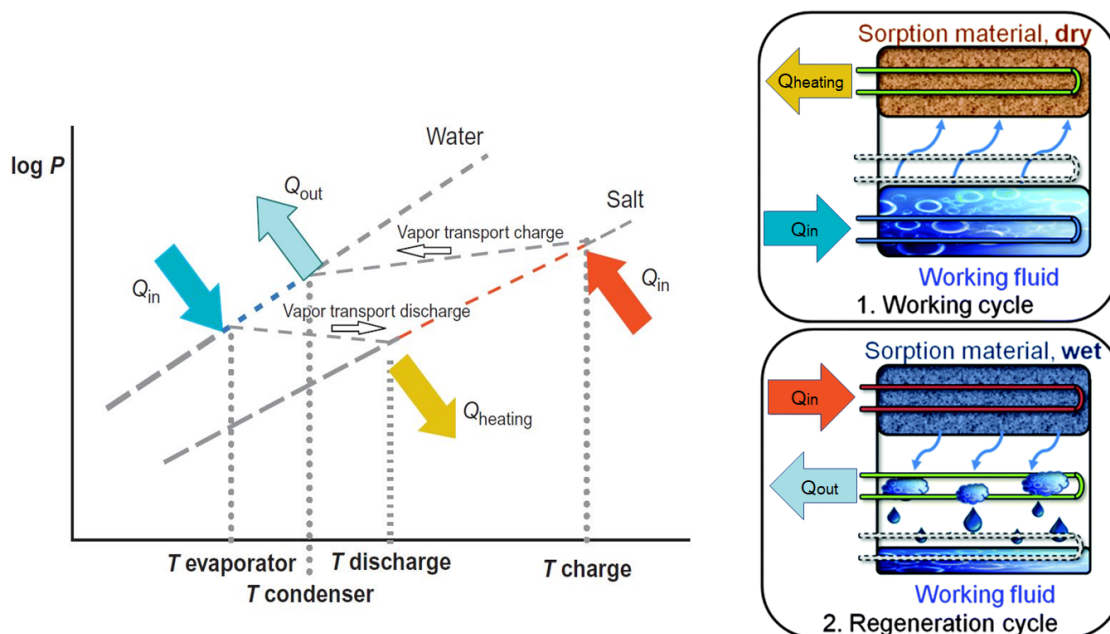


Figure 3.2: Pressure against temperature plot of charging and discharging for a TCS system with a schematic heat flows in system during the two cycles [16] [17]

3.2 Current technological state of closed thermochemical energy storage

The Technology Readiness Level of TCS systems is very low compared to chemical and electrical energy storage systems, it is also lower than sensible and latent TES storage [18]. Universities and research facilities are still in the process of investigating materials and configurations. This chapter will give a few examples of tests with closed TCS systems. It will become apparent that there are still lots of challenges before a commercial system can be realized.

MODESTORE [19]

MODESTORE is a project performed by *AEE Intec*. in Gleisdorf, Austria. It is a closed adsorption system, which uses silica gel as adsorbent and water as adsorbate. The system contains a spiral heat exchanger around the storage material and a water container connected to an evaporator/condenser. The heat source was provided by a flat plate solar collector with an area of 32m^2 . The water buffer could store 900L . There were two containers each containing 500kg of adsorbent material. The setup is schematically drawn in Figure 3.3. The system worked, but the results were far below expectations. The storage density was far lower than expected, this was due to a fast decrease in temperature difference. Only 35% of the storage capacity could be used effectively. To overcome this different tests were done using higher performing adsorbent: 13X zeolite. In the end the system was fully functional with a 750L volume of storage. A enormous volume is needed to store seasonal heat. The energy density of zeolite is too low.

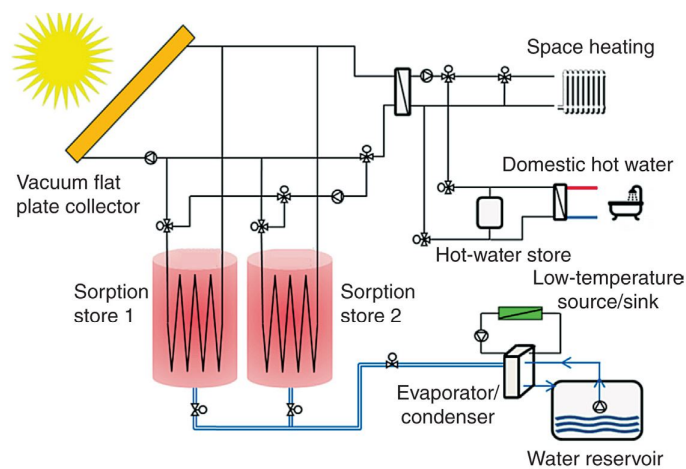


Figure 3.3: Schematic drawing of the MODESTORE set-up [19]

MERTIS [20]

MERTIS was a consortium between universities, research organizations and companies with the goal to design a heat battery for heating, cooling and domestic hot water applications. The adsorbate is water and the adsorbent Na_2S . The setup was almost identical to the one described in the MODESTORE project. The adsorbent was also placed in a shell-and-tube type exchanger with fins. A energy density of $39\text{kWh}/\text{m}^3$ was reached. The system needs to be charged at 90°C and discharges energy at 50°C . Although the technology looks very promising, the energy density was far too low for the system to be implemented in houses. Further development is needed.

MCES [21]

MCES was a project performed at the Chiang Mai University in Thailand. In a small experimental setup (250g of absorbent material) absorbent improvements were researched. The system contained a stainless steel shell-and-tube reactor, filled with Na_2S as absorbent. The system also contained an evaporator and a condenser which are placed in line with the reactor. To improve the thermal conductivity and increase the reaction area, carbon fiber is added to the sodiumsulfide. It was found empirically that a 1:3 ratio of graphite to sodiumsulfide gives the best performance. It was determined that using this composition 2.2kWh per kilogram absorbent composite could be realized. The system is charged at 80°C and discharges energy at 50°C to 60°C . It was proven that additives like graphite can improve the reactor performance of the closed thermochemical storage system.

Tan Yan at Institute of Refrigeration and Cryogenics [22]

An experimental study performed at the Institute of Refrigeration and Cryogenics of Shanghai Jiao Tong University has achieved impressive storage densities between $51\text{kWh}/\text{m}^3$ and $261\text{kWh}/\text{m}^3$. This was realized using ammonia as an absorbate and a mixture between MnCl_2 and SrCl_2 as absorbent. A shell-and-tube type exchanger is used. The tube is equipped with fins for better heat transfer efficiency. Two of these heat exchangers are filled, one with MnCl_2 and one with SrCl_2 . To improve thermal conductivity, cycle stability and ammonia diffusion, the materials are covered in porous expanded graphite. During charging ammonia escapes from MnCl_2 and is captured in SrCl_2 . During discharging this process is reversed. Big disadvantages of this system is that, the system needs to be charged at 177°C and discharges energy at 45°C . For these temperatures it is not possible to charge the system using solar collectors and that the stored energy cannot be used for tap water heating. Also the used absorbent materials are rather expensive.

3.3 Phase transition

Elementary distinctions between the three phases are based on the ability to maintain volume and shape. Solids are known to remain both volume and shape. Liquids remain volume, but its shape is determined by the container it is stored in. Matter in a gaseous state can both vary in shape and volume to fit its container.

Different phases of one substance can be characterised by a phase diagram, like the one presented in [Figure 3.4](#). Stable states of matter are separated by lines. These lines are also called coexistence curves. On these lines two phases coexist. The three different coloured coexistence curves in [Figure 3.4](#) meet in the triple point. Here all three phases coexist. The blue line is also called the boiling curve. This curve was already shown in [Figure 3.1](#) for various substances. The path of this line is essential for the design of an evaporator/condenser.

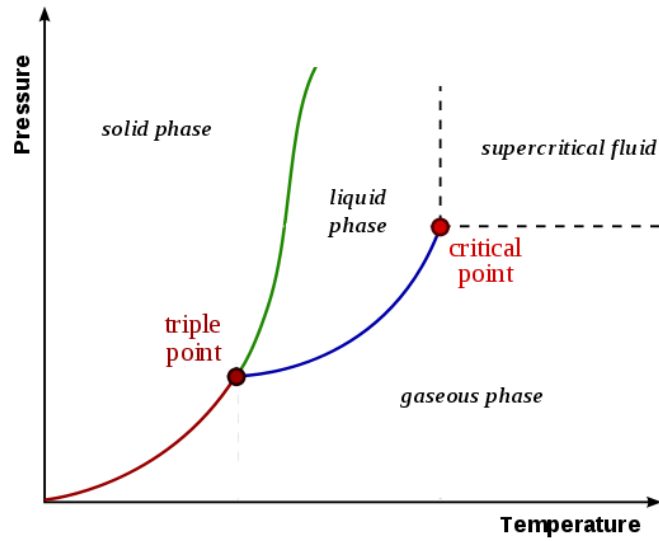


Figure 3.4: Pressure against temperature phase diagram for most substances. With the equilibrium lines between solid and gaseous phase (red), between solid and liquid phase (green) and between liquid and gaseous phase (blue) [23]

The phase transition can also be visualized differently. A vertical line in Figure 3.4 means a constant temperature path. By plotting the pressure of such a path against the specific volume in that particular state Figure 3.5 is created. In this plot the saturation curve of water is plotted in black. An isothermal line for 100°C is plotted in red. Left of the curve the water is fully liquid. Right of the curve the water is fully in a gaseous state. When the isothermal line is below the saturation curve, the water is a mixture of liquid and vapor. It can be seen that the evaporation takes place at a constant temperature and a constant pressure (for 100°C at 1atm). At very high pressures the critical point is reached. Above the critical point no distinction can be made between liquid and gas.

3.4 Boiling

This section will describe the physical principles surrounding boiling. Boiling is an intense vaporization process. When the fluid is heated above its boiling point, boiling can occur within the fluid and on the free surface of the fluid. This is in contrast with evaporation which can only take place on the liquid surface.

3.4.1 Bubble formation

For a spherical vapor bubble to exist within a liquid, the two phases must be in thermal equilibrium, of which the symbolic notation is presented in Equation 3.4.

$$T_{sat} = T_g = T_l \tag{3.4}$$

With T_{sat} the saturation temperature, T_g the temperature of the gaseous state (K) and T_l the temperature of the liquid state (K). Such a bubble should also be in mechanical equilibrium according to the Young–Laplace equation presented in Equation 3.5.

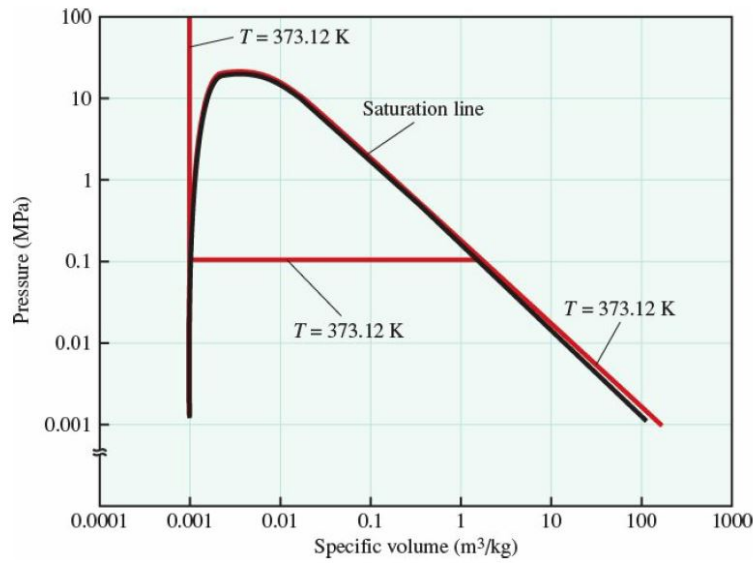


Figure 3.5: A double logarithmic plot of the pressure against the specific volume during phase change between liquid and vapor. With an isothermal line in red and the saturation curve of water in black [24].

$$p_g - p_l = \gamma \frac{2}{R} \quad (3.5)$$

With p_g the pressure in the gaseous state (Pa), p_l the pressure in the liquid state (Pa), γ the surface tension (N/m) and R the radius of curvature (m).

The slope of the equilibrium line between liquid and vapor, or boiling curve, is governed by the Clausius-Clapeyron equation which is presented in Equation 3.6 [25].

$$\frac{dp_{sat}}{dT_{sat}} = \frac{\Delta H}{T_s(v_g - v_l)} \quad (3.6)$$

With $\frac{dp_{sat}}{dT_{sat}}$ the slope of the equilibrium curves like the ones in Figure 3.1, ΔH the enthalpy difference due to vaporization per mass (J/kg), T_s the temperature of the interface surface (K), v_g the specific volume of the gaseous state (m^3/kg) and v_l the specific volume of the liquid state (m^3/kg).

The relations described say something about the existence of bubbles not about the formation of bubbles. By inserting Equation 3.5 in Equation 3.6 and using the fact that the specific volume of vapor is much larger than that of liquid. The amount of excess temperature which is needed for a vapor bubble to form can be calculated using Equation 3.7.

$$\Delta T_{ex} = \frac{2\gamma T_s}{\rho_g \Delta H R} \quad (3.7)$$

With ΔT_{ex} the excess temperature (K) and ρ_g the density of the gaseous state (kg/m^3).

It is observed that vapor bubbles are not formed everywhere within the liquid, aside from extreme cases. Vapor bubbles are formed on the heated surface [26]. It was also observed that bubbles reappear at the exact same place on the heated surface. In reality the surface has a certain surface roughness caused by small imperfections like cavities or bumps. These small spaces function as a catalyst for the formation of vapor bubbles out of superheated liquid. In these dents a small quantity of vapor remains all the time. When enough heat is supplied this small quantity of vapor will increase until a bubble can be observed. At a certain bubble size the vapor will detach from the heated surface. Bubble detachment occurs because the adhesion forces between vapor and surface will be smaller than the buoyancy force. This bubble size is a characteristic of the evaporation process. It is often referred to as the bubble departure diameter. When the vapor bubble detaches, a small quantity of vapor will remain in the cavity. The remaining vapor will be cooled by the fresh colder water which flows in the cavity. The whole process will repeat. This cyclical process is visualized schematically in Figure 3.6. The positions where bubbles are repeatedly formed due to the presence of a bit of remaining vapor are called nucleation sites. The conclusion can be drawn that the composition and structure of the surface is influencing the heat transfer when boiling.



Figure 3.6: Visualization of bubble formation at nucleation site [27]

The amount of energy needed to form a stable vapor bubble can be determined using thermodynamics. This amount of energy is called the critical energy for bubble formation. This critical energy has two contributing parts, one related to the increasing volume and one related to the increasing surface area. The exact relation is presented in Equation 3.8 [28]. The first part stands for the heat which is needed for producing the amount of vapor to create a bubble of the critical size. The second part stands for the energy which is needed to increase the surface area of the bubble to the critical size. In this second part the positive contribution stands for the isothermal work which needs to be done by the surface of the bubble to grow. The negative contribution stands for the heat which is needed to keep the growing surface at a constant temperature equal to the liquid temperature.

$$E_{crit} = \frac{4}{3}\pi R_{crit}^3 \rho_g \Delta H + 4\pi R_{crit}^2 \left(\gamma - T_l \frac{d\gamma}{dT} \right) \quad (3.8)$$

With E_{crit} the energy needed to form a vapor bubble with the critical radius (J) and R_{crit} the critical radius (m).

From Equation 3.8 it becomes apparent that the energy of a bubble consists out of the sum of a quadratic and a cubic relation with the bubble radius. This can also be seen when the Gibbs free energy of the system is plotted against the bubble radius as is done in Figure 3.7.

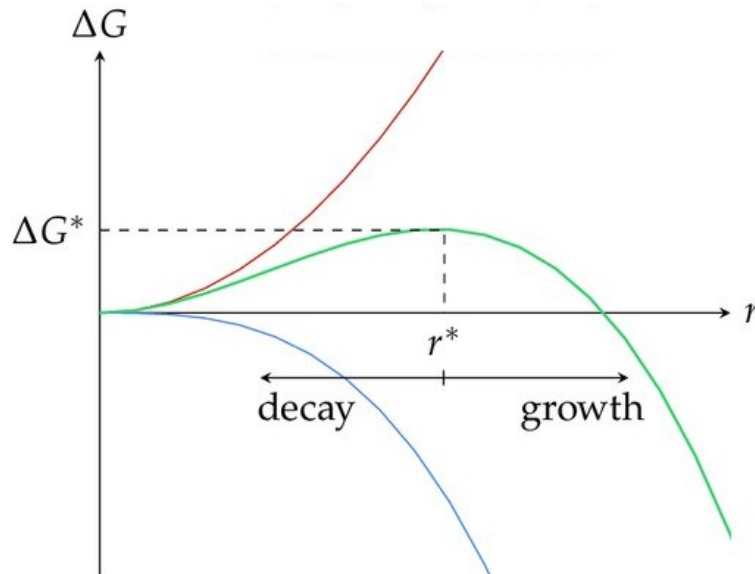


Figure 3.7: Change in Gibbs free energy as a function of the bubble radius (green), with the contribution due to the surface (red) and due to the volume (blue) [29]

In [Figure 3.7](#) the Gibbs free energy of a bubble is plotted as a function of its radius in green. The red line is the Gibbs free energy of the bubble surface with increasing radius and the blue line is the Gibbs free energy of the bubble volume with increasing radius. The green line is simply the sum of the blue and red line. Based on the principle of minimum energy the system forces the Gibbs free energy to be as low as possible. It can be seen from the graph that the volume contribution would like to have a radius as large as possible and the surface contribution would like a radius as small as possible. Both effects can be seen in the green line. If the radius would be below the critical radius (in [Figure 3.7](#) denoted by r^*) then the surface forces would win from the volume forces and the vapor bubble would immediately decay to form liquid again. If the radius would be larger than r^* then the Gibbs free energy can be lowered with increasing radius, causing the vapor bubble to grow larger. So for a stable bubble to form and grow the energy supplied to the bubble must be larger than the critical Gibbs free energy (in [Figure 3.7](#) denoted by ΔG^*).

3.4.2 Pool boiling

Pool boiling is a method of vaporizing liquid, in which the superheated element is small in size compared to the pool of liquid in which it is immersed [30]. The liquid is assumed to be stationary and the velocities introduced by the boiling itself can be neglected.

Nukiyama was the first to discover that there are different pool boiling regimes related to the excess temperature, which influences the heat transfer [31]. [Figure 3.8](#) shows the curve first discovered by Nukiyama including all the different regimes for water at atmospheric pressure. This curve relates the temperature difference between the superheated surface and the bulk of liquid to the heat flux which can be obtained.

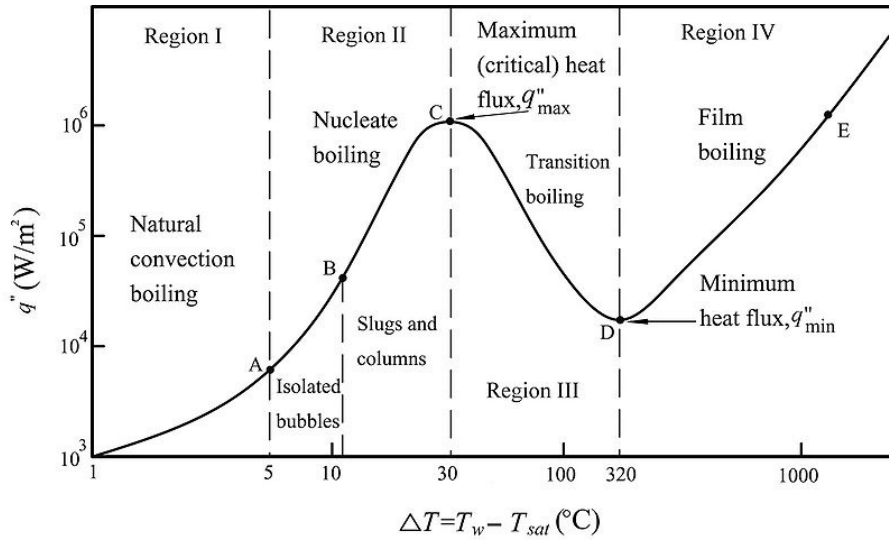


Figure 3.8: Pool boiling curve for saturated water at atmospheric pressure [32]

Region I: If the excess temperature is low, no vapor bubbles will form, The heat is transferred through the liquid via natural convection boiling. Water will evaporate on the surface but bubble formation in the liquid can not be observed.

Region II: If the excess temperature is increased, the nucleate boiling regime is entered. At the nucleation sites vapor bubbles are formed, which detach and travel through the fluid. Depending on the excess temperature the vapor bubbles will have a different geometry. At lower excess temperatures small isolated bubbles are formed. With increasing excess temperature, more nucleation sites will become active and bubbles will merge into larger columns. The differences are visualized in Figure 3.9. Because of the increased amount of vapor at the surface, there is less contact area between the surface and the liquid. This explains the decreasing slope in the nucleate boiling regime of Figure 3.8, when the temperature increases. At some point the slope is decreased to zero. This point, in the figure denoted by C, is called the critical heat flux (CHF).

Region III: If the excess temperature is increased beyond the CHF, bubbles are generated faster than bubbles can detached from the heating surface. This results in a film layer of vapor covering the heating surface. Region III, which is called transition boiling, is an unstable condition. The film layer can detach and nucleation boiling can reoccur, or the excess temperatures will increase and a stable vapor film to form. The point were stable film boiling is first observed is called the Leidenfrost point and in Figure 3.8 it is denoted by D.

Region IV: If the excess temperature is larger than the Leidenfrost temperature the heating surface is completely separated from the liquid by a film of vapor. The evaporation now happens at the liquid-vapor interface, as can also be seen in Figure 3.9. This film boiling regime is continued until the excess temperature is so high that the surface starts melting.

If the pool boiling system is controlled by the heat flux, the temperature of the heating surface follows the curve from Figure 3.8. If the heat flux is increased above the CHF the temperature will jump directly from nucleate boiling to film boiling. This results in an enormous jump in surface temperature with catastrophic consequences. This phenomena is called burnout or boiling crisis [34]. Between the Leidenfrost point and the CHF there are three solutions for the same heat flux, of which the solutions in Region II and Region IV are stable. Historically, boiling crisis was avoided by keeping the heat flux below the Leidenfrost point. In that case there would only be one solution, which would lay in the nucleate boiling regime. Nowadays it is possible to achieve higher heat fluxes safely using careful system control.

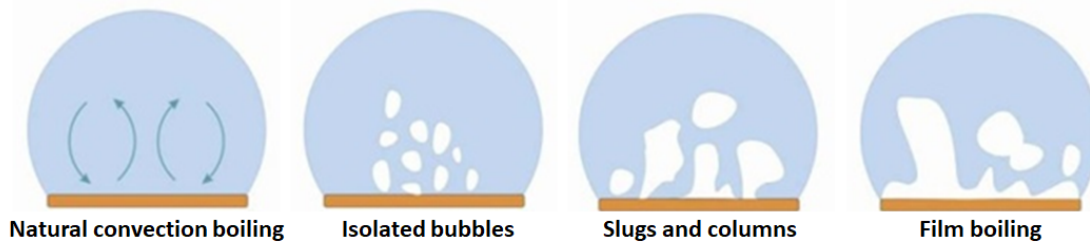


Figure 3.9: Different types of vapor bubble formation for the regimes in Figure 3.8 [33]

3.4.3 Boiling under subatmospheric conditions

The main advantage about subatmospheric boiling is the decrease in saturation temperature, which makes it possible to evaporate at lower temperatures. A disadvantage is the decreased effectiveness of the boiling process. At lower temperatures the surface tension will be higher and the vapor density will be smaller. It can be seen in Equation 3.7 that this will require a higher excess temperature. Larger buoyancy forces will be needed to overcome the increased surface tension. This will result in the formation of larger bubbles and larger bubble departure areas [35]. After the bubble departs a larger quantity of cold water will flow to and cool down the surface. The order of magnitude of these differences can clearly be seen in Figure 3.10. The upper box in Figure 3.10 shows snapshots of the bubble formation, from birth until after detachment at a pressure of 5.6 kPa . The lower box in Figure 3.10 shows snapshots of the bubble formation under atmospheric conditions. Two differences can clearly be seen: under subatmospheric conditions the bubble diameter is much larger and the bubble detachment time is much longer.

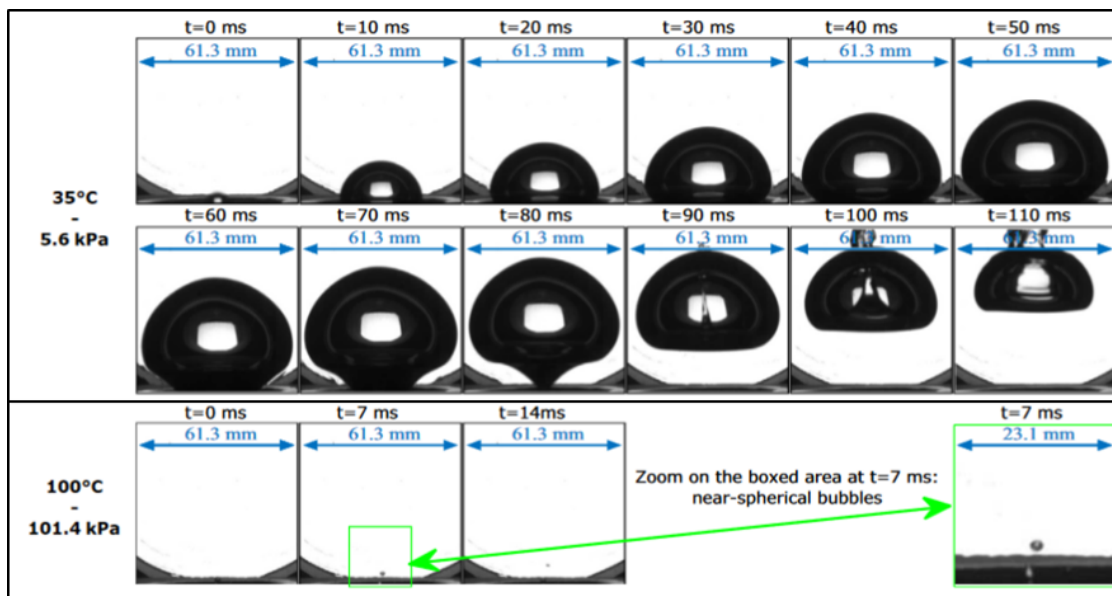


Figure 3.10: Snapshots of vapor bubble formation process: above under subatmospheric conditions (5.6 kPa), below under atmospheric conditions (101.4 kPa) [36]

The heat transfer coefficient relates the heat flux to the excess temperature, as can be seen in Equation 3.9.

$$h'' = \frac{q''}{T_{wall} - T_l} \tag{3.9}$$

With h'' the heat transfer coefficient (W/m^2K), q'' the heat flux (W/m^2) and $T_{wall} - T_l$ the temperature difference between the wall and the liquid (K).

Decreasing the pressure has an influence on the pool boiling curve presented in Figure 3.8. This was proven using experimentation. In the experiments water was heated via a Joule heating element, of which the heat flux can be monitored. The excess temperature was measured using thermocouples. Different experiments were performed under various subatmospheric pressures. Figure 3.11 contains boiling curves for different subatmospheric pressures. It can be seen that the first graph, at a pressure of $100kPa$, follows the curve earlier seen in Figure 3.8 exactly. As the pressure decreases the shape of the curve starts to deviate from the Nukiyama curve. As expected a higher excess temperature is needed to achieve the same amount of heat flux if the pressure is lower. The shape of the curve also changes drastically and the data scatters. It changes from an exponential shape to a cyclic shape. If the pressure is low enough boiling will occur in the cyclic boiling regime [37].

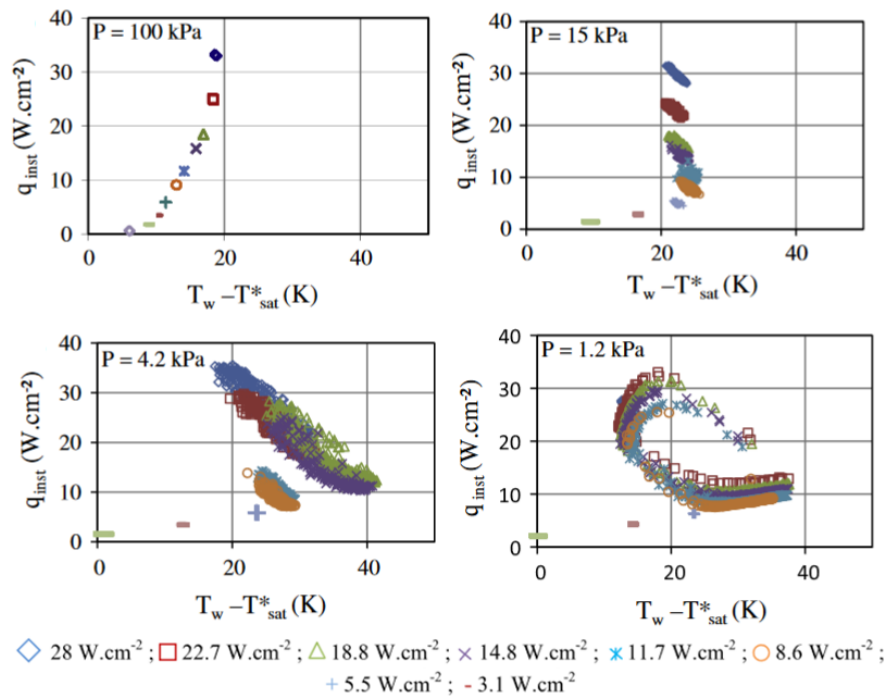


Figure 3.11: Experimental pool boiling curves obtained with a water height of 20 cm for 100 kPa , 15 kPa , 4.2 kPa and 1.2 kPa [37]

The cyclic boiling regime can clearly be seen in Figure 3.11 for a pressure of 1.2 kPa (the last graph). This regime consists out of three repeating phases. The first phase starts in the minimum of the curve. The temperature of the wall starts to increase, but only heat is transferred via convection. As the wall temperature is sufficient for nucleation a large bubble forms. As this bubble detaches the wall temperature quickly drops. This corresponds to the maximum of the

cyclic shape in the boiling curve. The third phase starts after the large bubble has detached. The wall temperature is relatively low but there is still a considerable amount of energy in the wall. Many bubbles with varying sizes and different frequency of detachment are then created over the whole heating surface, also called bubble crisis. If the heat flux has dissipated, the wall starts to heat up again, which is the first phase of the cycle [37].

The Jakob number is a dimensionless quantity used to characterize boiling and condensing. This relation for the Jakob number is presented in Equation 3.10.

$$\mathcal{J}a = \frac{\rho_l c_{p,l} \Delta T_{ex}}{\rho_g \Delta H} \quad (3.10)$$

With $\mathcal{J}a$ the Jakob number (-) and $c_{p,l}$ the specific heat capacity of the liquid (J/kgK).

Equation 3.10 describes the ratio between sensible heat and latent heat during boiling. In other words: $\rho_l c_{p,l} \Delta T_{ex}$ is the amount of heat required for the bubble to form, $\rho_g \Delta h$ is the amount of heat which can be released via the bubble. If the Jakob number is small, latent heat is dominant over sensible heat. This means vapor bubbles will grow slowly and the departure diameter is small. At a low Jakob number bubble formation is controlled by the surface tension. If the Jakob number is large, sensible heat is dominant over latent heat. This results in fast growing vapor bubbles and large departure diameters. The bubble formation will be controlled by inertia forces [38]. In subatmospheric systems the Jakob number is large, and the Jakob number increases rapidly with small decreases in absolute pressure [39].

3.5 Condensation

If vapor contacts a surface which is below the saturation temperature, vapor will turn to the liquid state. This is the most common type of condensation and it is called heterogeneous condensation. The phase change from vapor to liquid is an exothermic process, meaning heat is produced. Condensation can also happen in a medium. If small particles are present within the vapor, these can function as condensation nuclei if the vapor is cooled enough [40]. This is called homogeneous condensation. Condensation can also occur on a liquid surface. This is called mixed condensation. In heterogeneous condensation drops of liquids start to condensate at condensation nuclei on the surface, these drops become larger. This is called drop condensation. If the surface is completely covered with water, vapor no longer condenses at the wall, but on the liquid film. This is called film condensation [41]. Dropwise condensation is desired over filmwise condensation, since heat transfers can be one order of magnitude larger [42].

The wettability of the supercooled surface determines the type of condensation. The contact angle between the liquid and the surface is a measured for the wettability. Its expression is provided in Equation 3.11.

$$\cos \theta = \frac{\gamma_{sv} - \gamma_{sl}}{\gamma_{lv}} \quad (3.11)$$

With θ the contact angle ($^\circ$), γ_{sv} the surface tension of the solid vapor interface (N/m), γ_{sl} the surface tension of the solid liquid interface (N/m) and γ_{lv} the surface tension of the liquid vapor interface (N/m).

Figure 3.12 shows the influence of the contact angle on the droplet shape. Here it is shown that by decreasing the surface tension of the liquid vapor interface (γ_{lv}) the contact angle will decrease and wettability will increase. Dropwise condensation mostly happens if the contact angle is larger than 90° [43].

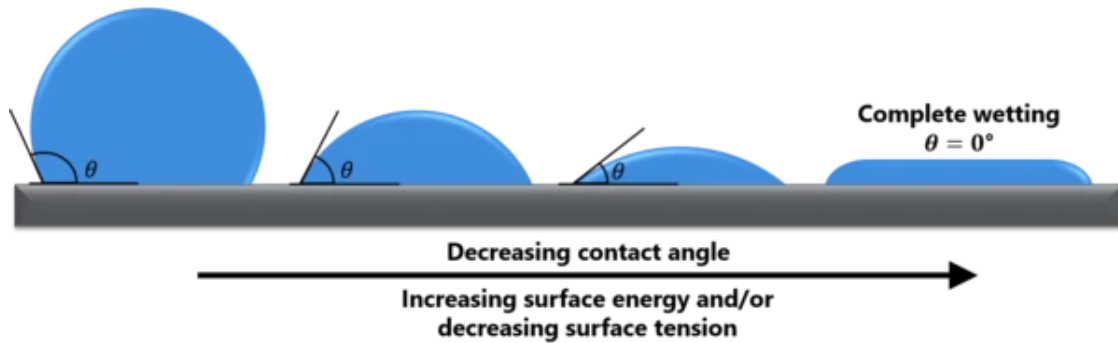


Figure 3.12: Influence of contact angle on the droplet shape [44]

Due to strong hydrogen bonds water has a high surface tension compared to other liquids. Dropwise condensation is therefore common in water vapor systems due to the high contact angle. The wettability of surfaces can be decreased to achieve dropwise condensation. This can be done by lowering the surface energy. This can be done by applying hydrophobic material to the surface, coating it with low free surface material (like polymers) or modification of the surface structure [45].

Droplets are formed on the surface at minima in free surface energy. Droplets will grow and merge with neighbouring droplets until they have accumulated so much weight that they will start to move due to gravity. When the large droplet rolls over the surface it will take up smaller droplets along the way. At these surfaces new droplets can be formed again. This effect contributes to the relatively large heat transfer for dropwise condensation [42].

At low vapor pressures, less mass will be present that can be condensed. This reduces the growth rate of the droplets. Additionally at low vapor pressures droplets will be bigger, before they fall of the surface. This is for the same reason as why subatmospheric boiling will result in bigger vapor bubbles. Namely, at lower temperatures the surface tension will be larger. Increased droplet size causes a larger heat transfer resistance [46]. A lot of empirical relations are constructed to describe the heat transfer coefficient during dropwise condensation [47], [48].

3.6 Influence of hydrostatic pressure

For liquid water to exist in a vacuum system the surface pressure must at least be equal to the saturation pressure for the given temperature. If the pressure would be lower, vaporization would occur. It was already shown in Figure 3.1 that the saturation pressure is a strong function of the temperature. In the case of pool boiling a considerable column of water is above the heating element. With this height the absolute pressure increases because the weight of the water results in hydrostatic pressure. With Equation 3.12 the absolute pressure at a certain depth in the water can be calculated. The pressure needed for pool boiling in a closed system, is the summation of the saturation pressure at the surface and the hydrostatic pressure.

$$p = p_s + \rho_1 g z \quad (3.12)$$

With p_s the pressure at the liquid surface (Pa), g the gravitational acceleration (m/s^2) and z the water column height (m).

A certain temperature is required to achieve boiling at a certain column height (z). This is at least the saturation temperature at the absolute pressure, so the combination of the pressure at the surface and the hydrostatic pressure. Figure 3.13 shows the influence of the column height on the absolute pressure at the heating surface and the required saturation temperature in a vacuum. For the example in the figure the bulk temperature is set to $20^\circ C$.

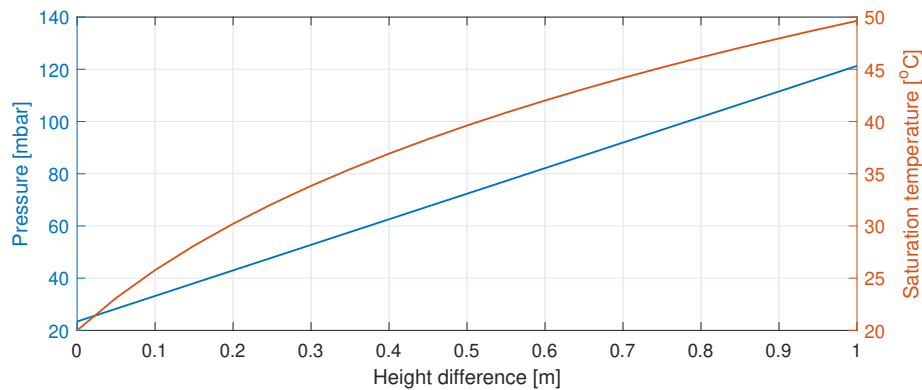


Figure 3.13: Influence of column height on the pressure (blue) and saturation temperature (red) for $T = 20^\circ C$ at the water surface

It can be seen in Figure 3.13 that the absolute pressure (blue) increases linear, which is in line with Equation 3.12. It can also be seen that the saturation temperature (red) increases but nonlinear. A relatively small column height ($\pm 0.25m$) can double the absolute pressure and cause a $13^\circ C$ saturation temperature increase.

The excess temperature is defined as the temperature increase required to realize vaporization. This relation can also be inverted: What is the maximum column height, for a fixed excess temperature to still achieve boiling? As the excess temperature increases this height also increases. This relation is important for the condenser evaporator design. Because it determines how compact the heat exchanger can be. With more excess temperature available a larger column height of water can effectively be boiled by the heat exchanger, which makes it possible to increase the heat exchanger height. The contact area of the heat exchanger needs to be constant to deliver the same amount of power. If more height is available then the width and depth of the evaporator condenser can be decreased, which is desired to keep the total system compact.

A recent numerical study of nucleate pool boiling on a vertical surface [49], validated by experiments [50], has produced results on the influence of water column height on the evaporation mass transfer for various low pressures. It was found that for $10kPa$ the influence of hydrostatic pressure on the mass transfer due to evaporation is negligible. As the pressure decreases the mass transfer also decreases due to less effective evaporation. For pressures of $2kPa$ and lower, the mass transfer starts to vary over the water height. Deep in the water less evaporation takes place than near the surface.

A very recent paper by Wojtsaik et al. studies the influence of hydrostatic pressure on the heat transfer of subatmospheric pool boiling [11]. In this article experimental research was done using the apparatus visualized in Figure 3.14. This particular apparatus is used to map boiling regimes of water under subatmospheric conditions. A bulk of water, of which the column height can be easily controlled, is evaporated via pool boiling using an electric heater. This means that the heat flux can be imposed directly on the heating surface. The setup contains multiple thermocouples measuring the bulk of water at different water heights. At the top of the setup the pressure is measured. A camera is pointed at the heating surface and captures the boiling behaviour. The setup which was built for the experimentation in this thesis, which will be further explained in section 4.2, is inspired by the setup in Figure 3.14.

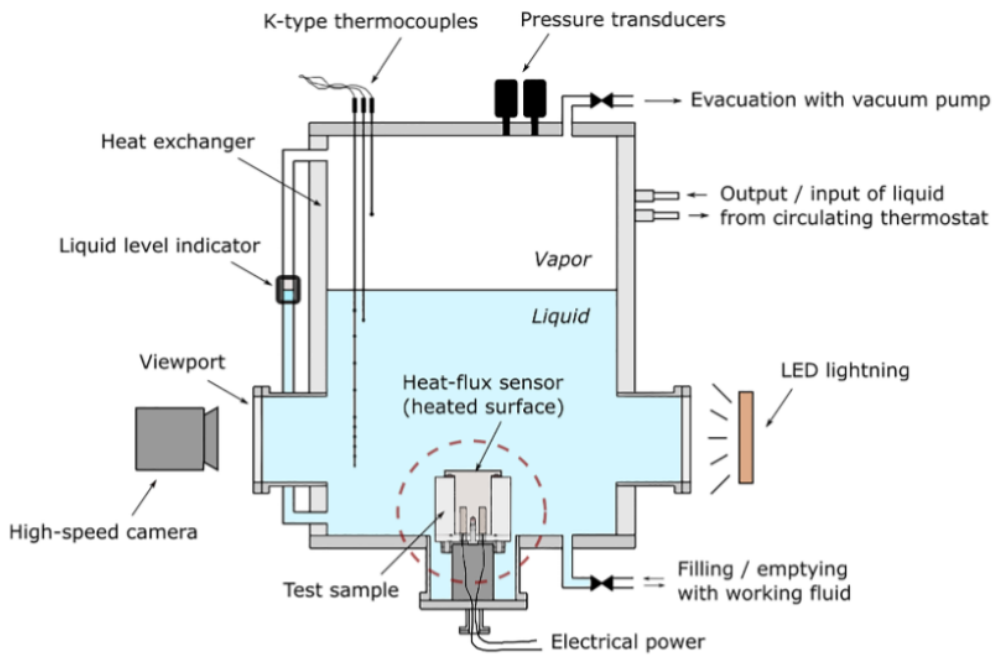


Figure 3.14: Experimental apparatus used in the research of Wojtasik et al. [11]

The thermocouples are there to give an indication when the water temperature has reached a steady state. These thermocouples are also used to calculate the excess temperature. The pressure sensor at the top of the apparatus measures the vapor pressure, which determines the saturation temperature of the water. By applying electrical power the amount of applied heat flux can directly be regulated. Also the vapor pressure can be regulated. The influence of changing these three parameters was researched: three vapor pressures (2.4 kPa, 3.1 kPa, 4.1 kPa), four levels of liquid (15 cm, 28 cm, 35 cm, 60 cm) and five applied heat fluxes (3.6 W/cm², 4.4 W/cm², 5.2 W/cm², 6.1 W/cm² and 7.1 W/cm²). Using statistics and bubble dynamics captured with a high-speed camera, four different boiling regimes were identified and all data results are categorized in these regimes. Three boiling regime maps were made to describe the relation between water column height and applied heat flux, for the three vapor pressures. Two of these maps are visualized in Figure 3.15. These different maps can be combined in one map by plotting the Jakob number, as already seen in Equation 3.10, as a function of the ratio between surface pressure and hydrostatic pressure.

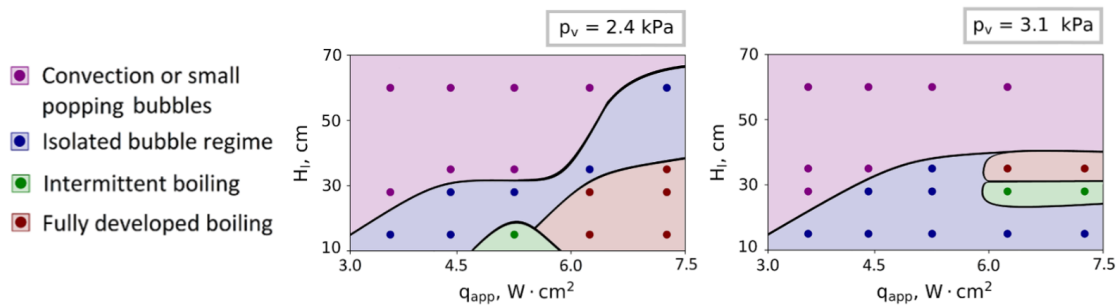


Figure 3.15: Boiling regime maps for vapor pressures of 2.4 kPa and 3.1 kPa [11]

In [Figure 3.15](#) two boiling regime maps can be seen. Each dot represents a measurement point. On the x-axis the applied heat flux is plotted, on the y-axis the water height is plotted. Each measurement set is classified in a regime, based on visual observations and statistical data on the heat exchange. These regimes are similar to the different types visualized in [Figure 3.9](#). Natural convection boiling is visualized in purple, Isolated bubbles in blue, slugs and columns in red and green denotes the transition phase between isolated bubbles and slugs and columns. It can be seen in [Figure 3.15](#) that deep in the fluid only convective boiling take place. Decreasing the water level at the same applied heat flux results in a shift in boiling behaviour and more heat transfer. At higher subatmospheric pressures (the right graph) heat transfer deep in the water will be lower.

This study already gives a lot of insight in what to expect from the experiments done in this thesis. The main difference between Wojtsaik et al. and the research in this thesis lies in the heating element. Because this thesis focuses on the application of subatmospheric evaporation in a thermochemical storage system setting, an electric heating element is not suitable. In closed TCS a heat exchanger is used to evaporate the working fluid. This makes the experiment more complex, since the heat flux is not directly applied to the working fluid, it will not be constant over the heat exchanger. The same is true for the water column height, this will differ over the heat exchanger.

This chapter includes all information surrounding the experimental framework. The original setup was improved multiple times because undesired phenomena occurred during early tests. These improvements are included in [Appendix A](#). This chapter will only include details about the final setup.

4.1 Experiment choices

The experimental research in this thesis focuses on the subatmospheric evaporation, occurring during the discharging of the closed thermochemical storage system. In the discharging cycle of the thermochemical storage system the vapor produced in the evaporator is absorbed by the porous absorbent. The heat produced by the absorption process is transferred to the heat exchanger, which contains the absorbent. The reactor geometry and choice of absorbent material is of great influence on the vapor absorption and thus the boiling behaviour. Vapor transport in porous materials, reaction kinetics in porous materials and thermal conductivity between absorbent and heat exchanger on a system scale are research fields on their own and surpass the scope of this thesis. To keep the results of the experiments generic, no reactor was included in the setup. Instead, an overdimensioned condenser was attached to the evaporator. This will ensure that the vapor absorption is not the limiting factor. With this setup vapor production in the evaporator is barely restricted.

Multiple experiments are performed at different water heights, to research the influence of hydrostatic pressure. Different water heights result in different thermal mass, which will result in different time scales before water has reached a steady temperature during heating. A valve is placed between the evaporator and condenser. To keep individual experiments comparable the valve is opened when the water in the evaporator has reached a steady temperature. When the valve is opened the evaporator and condenser are in contact with each other. This ensures the same initial conditions for all experiments. The use of a valve is in accordance with the working of an actual thermochemical storage system. Without a valve vapor flows can reverse when input temperatures vary between charging and discharging, which cause the system to lose its storage ability.

During preliminary experiments it was observed that some time after the valve was opened a more or less steady state formed, where variations in temperature and pressure are low. The time span of the experiment captures the period from the steady state conditions of the system with a closed valve until far after the steady state conditions with an open valve have been reached. The duration of all experiments was 45 minutes from the moment the valves opened, which is far longer than the time it takes to reach steady open valve conditions.

4.2 Experimental setup

4.2.1 Parts, connections and placement of sensors

Figure 4.1 shows a diagram of the total setup including all sensors. The system consists mainly out of two bodies: the condenser and the evaporator. Both are connected via pipe segments. The thick arrows in Figure 4.1 represent the water flow. The thick red arrows represent the flow of the evaporator. The thick blue arrows represent the flow of the condenser. The thick black arrow represents the flow of the condensed water to the water collection vessel. The thin lines indicate the gaseous flow. The volumetric flow (F) is measured at the inflows of both bodies. The temperature of the flowing water is measured before (T_{in}) and after (T_{out}) going through the bodies. The temperature of the flow is measured in valves. These valves are always open when running an experiment. The pressure (P) in both bodies is also measured on a valve. These valves are always closed during an experiment. If one of these valves is opened, the corresponding body will come in contact with the vacuum pump. Before an experiment the pressures in both bodies are always checked. If the pressure in a body is higher than the vapor pressure for the particular temperature in this vessel, the valve is opened and gas is pumped out of that body. Then the valves to the vacuum pump are kept closed during the length of the experiment. In the evaporator vessel three thermocouples are placed (T_1 , T_2 and T_3). These are placed at different heights and can give insight in the stratification of the bath temperature. It was carefully determined that T_1 is placed at $z = 21.7\text{cm}$, T_2 is placed at $z = 14.0\text{cm}$ and T_3 is placed at $z = 3.1\text{cm}$. Between the condenser and evaporator gaseous transport is regulated via a vacuum valve, which can be opened and closed via the computer. If the valve is closed there is no contact between the bodies and both will reach a steady state temperature and pressure. If the valve is opened the bodies can interact with each other.

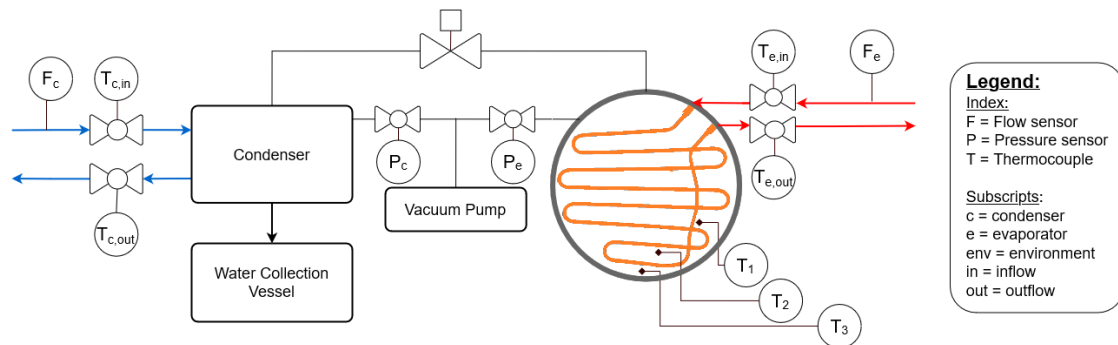


Figure 4.1: Schematic drawing of the experimental setup, including a legend. The thick arrows represent the water flow: the in and outflow of the evaporator (red), the in and outflow of the condenser (blue) and flow of the condensed water to the water collection vessel (black). The thin lines represent the gaseous flow. The lines with the square end represent thermocouples, which measure the water temperature at different heights

4.2.2 Design of the evaporator test chamber

For the experiments a vacuum test chamber with built-in evaporator is constructed that will fulfill the requirements for the experiments. The requirements are:

- The chamber should be transparent, so the boiling process can be observed.
- The heat exchanger should not obstruct the view on the boiling behaviour.

- The chamber should withstand stresses due to the pressure difference of the vacuum within the chamber and atmospheric pressure outside of the chamber.
- The system must run many experiments, so a negligible amount of fatigue should occur when pressurizing and depressurizing the chamber.
- It should be possible to open and close the connection between test chamber and condenser, when both are at subatmospheric pressures.
- Temperature measurements within the subatmospheric chamber should be possible.
- It should be possible to easily adjust the amount of water present in the test chamber.

To save cost a stainless steel cylindrical vessel for an evaporation-condenser, which was used in previous projects of *De Beijer RTB BV*, was converted. In the cylindrical stainless steel vessel five couplings of varying diameters are welded. The technical drawing of this vessel is shown in [Figure 4.2](#). In this drawing the different couplings are denoted by different letters. Two couplings are used to connect the heat exchanger (**A1 & A2**), one to attach the thermocouples in the vessel (**B**), a large connection to discharge the produced water vapor (**C**) and one to connect the vacuum pump and the pressure sensor (**D**).

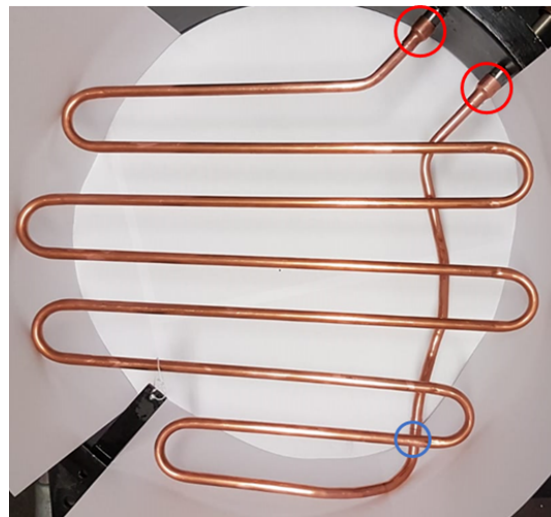
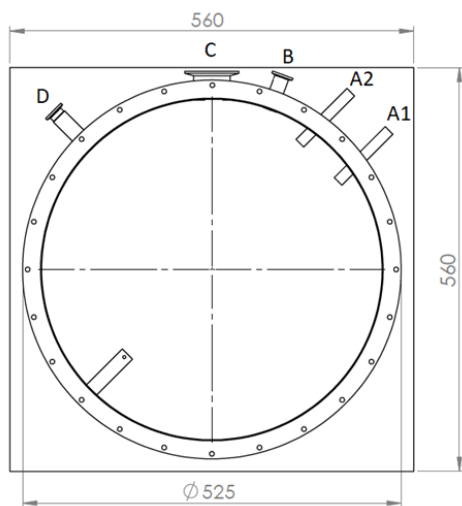


Figure 4.2: Technical drawing of the cylindrical vessel which will be used for the test chamber. The different couplings are denoted by different letters. The dimensions are in millimeters.

Figure 4.3: Shape of the copper heat exchanger which is installed in the cylindrical vessel. In the red circles the 15x10mm reducers and in the blue circle the solder fitting.

The heat exchanger is made out of copper pipe with an outside diameter of 10mm and a wall thickness of 1mm. The copper pipe is smooth: the arithmetic average surface roughness (Ra) is $0.5\mu m$. The total pipe length used in the heat exchanger is 3.15m. Using a 180° pipe bender, the heat exchanger is brought into shape. The heat exchanger shape is designed in such a way, that the structure is more or less two dimensional, while at the same time maximizing the surface area of the exchanger. The particular shape is visualized in [Figure 4.3](#).

A copper 15x10mm reducer is placed over the copper pipe and the stainless steel connection. The reducers are circled in red in [Figure 4.3](#). The copper structure itself consists out of two parts which are connected via a 10x10mm solder fitting. The fitting can barely be seen in [Figure 4.3](#) and is therefore circled in blue. Copper to copper connections are soldered. Copper to stainless steel connections are brazed. The inside of the cylindrical vessel and the copper is then thoroughly cleaned using isopropanol.

The bottom of the cylinder is bolted to a stainless steel plate. Between the cylinder and the steel plate three rings are placed: one stainless steel outer ring, one rubber ring [51] of a smaller diameter and one stainless steel inner ring of an even smaller diameter. The rubber seal is lubricated with high vacuum grease. This prevents that any small inconsistencies in the rubber will cause a leak. On top of the cylinder the same three rings are placed. On top of that a 25mm thick clear PMMA-layer is placed. This PMMA-layer contains 24 drilled holes corresponding to the holes in the outer ring. On top of that another outer ring is placed. These layers are bolted together tight. A rendered image of the top of the assembly is provided in [Appendix B](#).

The system is fully closed now. To locate any leaks in the heat exchanger or the vessel hydrogen leak testing is used. When all leaks were fixed. The chamber was then attached to the vacuum pump and after some degassing cycles it was concluded that the chamber was vacuum tight enough for the experimentation. The lowest pressure that could be reached was 4mbar and the system only gained 3mbar in 15 hours.

Before the vacuum vessel was built a Finite Element Analysis (FEA) was done to prove that the designed configuration of the PMMA-plate and the additional ring could withstand the forces caused by the vacuum. The details of this numerical study can be found in [Appendix B](#). From the study it could be concluded that the deformations would stay far within the elastic regime. The FEA concludes that plastic deformation or failure as a result of the pressure difference, between vacuum inside the vessel and atmospheric pressure outside the vessel, is ruled out.

4.3 Experiment procedure

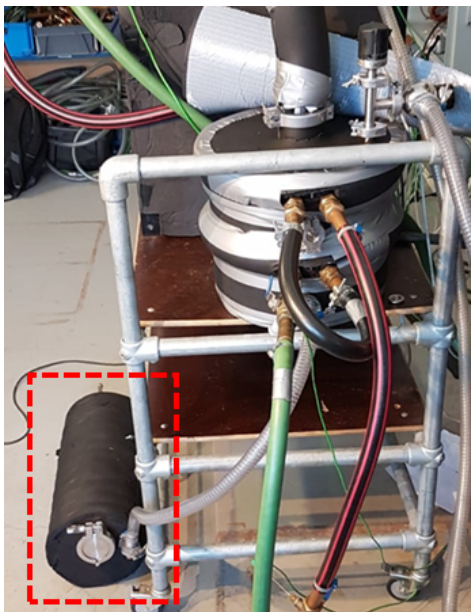
4.3.1 Before and between experiments

Degasification is very important for a successful experiment. When the system is assembled for the first time, the vacuum pump is hooked up to the dry system. When the vacuum pump is activated gas is sucked out of the system. The gas will mainly consist of air. But as the pressure decreases, small quantities of liquid still present in the vessel will start to evaporate. Think of small quantities of water or isopropanol from the cleaning process. When these quantities of water evaporate they are also sucked out by the vacuum pump. It is important that no other substances are present in the system, before the vessel is filled with demineralized water because this influences the subatmospheric boiling behaviour. By closing the valves between the chambers and the vacuum pump, which can be seen in [Figure 4.1](#), the pressure can built up due to evaporation of present liquids. When the pressure is built up slightly, the valves can then be opened again, to remove the residual gasses. This process can be improved by increasing the temperature in the chambers. This is done by letting hot water flow through the heat exchangers.

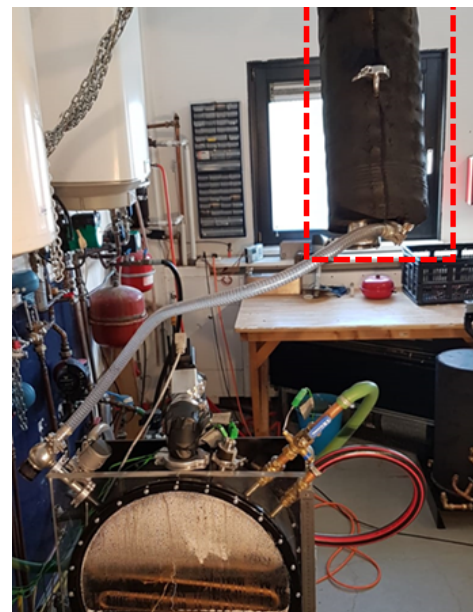
When the empty system is completely degassed the vacuum pump is disconnected and the full system is slowly brought back to atmospheric pressure. Demineralized water is added to the evaporator chamber. The vacuum pump is then hooked up to the system again and the air is

pumped out of the system. This will take longer since a considerable amount of air is entrapped in the water. When the measured pressure corresponds to the vapor pressure at the measured bath temperature, the vacuuming process is completed and the valves can be closed. The test setup is now ready for testing.

During tests water will vaporize in the evaporator room and condense in the condenser. At the bottom of the condenser a passage to the water collection vessel is made. In [Figure 4.4 \(a\)](#) this connection can be seen: the water collection vessel is placed on the floor and connected to the condenser via a transparent hose. This connection will function as an overflow which serves two purposes: Firstly, it improves the condenser performance for larger quantities of water. Normally during a test the condenser vessel will fill up with water. This will reduce the effective condensing surface, causing a decrease in condensing power. When the water height in the condenser equals the height of the passage, liquid will flow to the vessel, keeping the effective heat exchanger area constant from that point on. The second function of the vessel is to reuse the water, when doing multiple experiments. The water collection vessel can easily be detached from the condenser, when the system is brought back to atmospheric pressure. The water collection vessel can then be connected to the evaporator. The connection between the water collection vessel and the evaporator is visualized in [Figure 4.4 \(b\)](#). Water can now freely flow back to the evaporator due to gravity. Using this method batchwise recirculation of the water can easily be realized between experiments. The empty water collection vessel is then connected to the condenser again, as seen in [Figure 4.4 \(a\)](#). After bringing the system back to subatmospheric conditions, it is ready for the next experiment.



(a) Water collection vessel connected to the condenser.



(b) Water collection vessel connected to the evaporator

Figure 4.4: The water collection vessel (in the red dotted square) connected to the condenser (during experimentation) and to the evaporator (between experiments)

4.3.2 During experiments

At the start of the experiment it is important that no gas other than vapor is present within the setup. The measured pressures should equal the vapor pressures associated with the surface temperature. The flows and inlet temperatures can be set using software and hardware. The system has built-in measurement and control features, which will regulate that the flows and inlet temperatures stay at the set values. At the start of the experiment, the vapor valve between the evaporator and condenser is closed. The measured inflow variables will slowly meet the conditions which were set. This will result in heat up of the quantity of water in the evaporator and cool down of the quantity of water in the condenser. Eventually this system will reach steady state: There are barely fluctuations in the water temperature and the difference between inflow temperature and outflow temperature is low. When steady state is reached the vapor valve is opened and vapor will start to flow from the evaporator to the condenser. Rapid changes in outflow and bath temperatures can be observed. One measurement will take 45 minutes. It was observed that after that period of time the temperature differences between inflow and outflow were small and the boiling behaviour barely changed. When the experiment has ended data will no longer be logged and the vapor valve will be closed. A camera is aimed at the heat exchanger and the water surface to capture the boiling behaviour. [Table 4.1](#) contains an overview of all the set input variables for all of the experiments. This table also includes the maximum deviation from the set variable observed in all experiments. Inbuilt system control tries to maintain the set variables, but there will always be overshoot. The differences in fluctuations between evaporator and condenser variables can be explained by the fact that they have a different controller. The condenser variables are regulated using a controller with a higher gain factor when it comes to temperature. This means the controller will react aggressive to an error in temperature. This will result in a high overshoot when it comes to flow. The controller of the evaporator will have a slower response to the temperature error, thus allowing higher temperature differences, but keeping the overshoot in flow low. Fluctuations in these variables are inevitable and since they are carefully measured they will not influence the accuracy of the measurements.

Table 4.1: The set values for flow (\dot{V}) and inlet temperature (T_{in}) and the maximum observed fluctuations during all experiments

| Input variable | Set value | Observed fluctuation |
|-----------------|-----------|----------------------|
| \dot{V}_{eva} | 10 L/min | ± 0.23 L/min |
| \dot{V}_{con} | 10 L/min | ± 1.42 L/min |
| $T_{eva,in}$ | 30°C | ± 2.4 °C |
| $T_{con,in}$ | 10°C | ± 1.3 °C |

Due to the fluctuations in temperature, seen in [Table 4.1](#), the saturation pressures at the start of the experiment, will also be influenced. It was observed that the pressure in the condenser at the start of the experiment will always be between 11.7 and 12.5 mbar. The pressure in the evaporator at the start of the experiment will always be between 34.0 and 37.9 mbar.

4.4 Measurement techniques

4.4.1 Measurement devices

Four different measurement devices are used to collect data. The details about these four devices can be found in [Table 4.2](#). The positions of the thermocouples, flow sensors and pressure sensors are visualized in [Figure 4.1](#). The data of these three devices is collected using a data acquisition system. This system is connected to a computer equipped with a *LabVIEW* program. This software is also used to set the controllers, which regulates the flow and temperature during the experiment. The *LabVIEW*-program also saves the output of the measurement devices every second and saves this raw data in a *MS Excel* sheet, which can be imported and processed using *MATLAB*.

Table 4.2: List of measurement devices used in the experimental phase, including their operating range

| Measurement device | Name | Range | Reference |
|--------------------|---|-----------------|-----------|
| Thermocouple | Type: K Positive wire: NiCr Negative wire: NiAl | -40 - 1000°C | [52] |
| Flow sensor | <i>Kobold</i> : DUK 21G5HL 443L | 0.16 - 40 L/min | [53] |
| Pressure sensor | <i>Leybold</i> : Vacuum Transducer DI200 | 0.1 - 200 mbar | [54] |
| Ruler | <i>Maped</i> : 50cm Stainless Steel Ruler | 0 - 500mm | [55] |

The fourth measurement device, the ruler, is used to measure the height of the water column. This ruler is mounted to the PMMA-layer. A spirit level is aligned with the water surface. The height on the mounted ruler where the underside of the spirit level intersects is noted. [Figure 4.5](#) shows how a measurement of the water height is performed. During an experiment the water height is measured and written down every 5 minutes, started from the opening the valve until the end of the experiment. To increase the precision of the measurement the height is measured twice and the starting and ending time of the measurement is noted. Both values are averaged to improve the precision of the measurement.



Figure 4.5: A typical measurement of the water height: The underside of the spirit level needs to align with the water level, the spirit level also needs to be level, which is indicated by the bubble near the hand. The height is measured at the intersection between the ruler and the underside of the spirit level.

4.4.2 Calibration and error estimation

Calibration of the measurement devices is essential for the accuracy of the measurements. All these devices need to be calibrated before doing the experiment. With the exception of the ruler only digital measurement devices are used. In these devices a signal is outputted. The magnitude of this signal is related to the magnitude of the measured variable via a relation, which is assumed to be linear. During the calibration phase these relations are obtained. The systematic error is included in the calibration [56]. The random error, which is caused by unknown events, is the deviation between the correlation line and the measurement data.

The thermocouples were all calibrated together at fixed temperatures between 0 and 84 °C. The fixed temperatures were measured by a certified measurement device. The temperatures measured by the thermocouples can now individually be plotted against the certified temperature measurements. Using linear regression the calibration lines were constructed. Every thermocouple will have a different calibration line. The calibration line of one thermocouple is presented in Figure 4.6. The calibration lines will be put in *LabVIEW*, so thermocouples will output the calibrated temperatures directly during measurements.

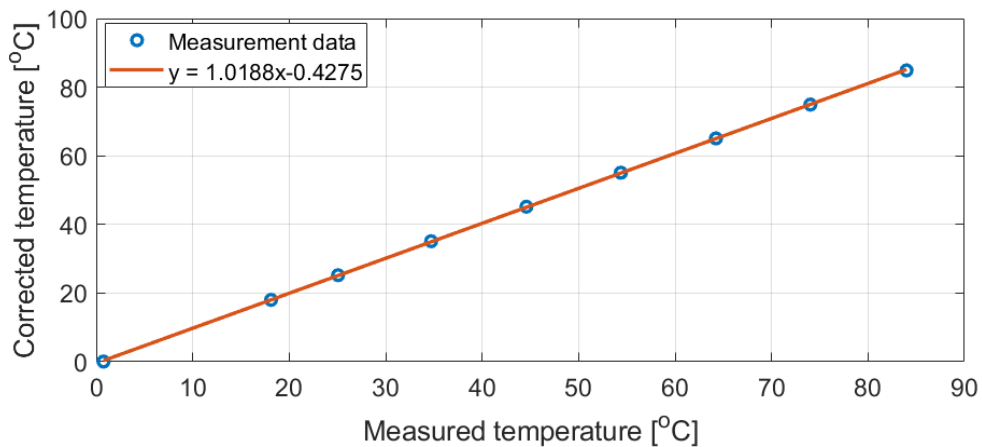


Figure 4.6: The calibration line for one thermocouple: on the x-axis the temperature measured by the thermocouple which requires calibration and on the y-axis the temperature determined by a certified measurement device. In blue the data points and in red the regression line through these points.

The residuals of the calibration line, visualized in Figure 4.7, are the random errors within the measurements. The operating range of all experiments lies between 8 and 35 °C. The random error of all thermocouples within the operating range is visualized in Figure 4.7. It can be seen that maximum random error within the measurements has a magnitude of 0.40 °C. From this distribution of random errors the standard deviation can be calculated using Equation 4.1.

$$SD_{\epsilon} = \sqrt{\frac{1}{N-1} \sum_{i=1}^N \epsilon_i^2} \quad (4.1)$$

In which N is the number of measurements (–) and ϵ is the absolute error, of which the unit is equal to the measured unit.

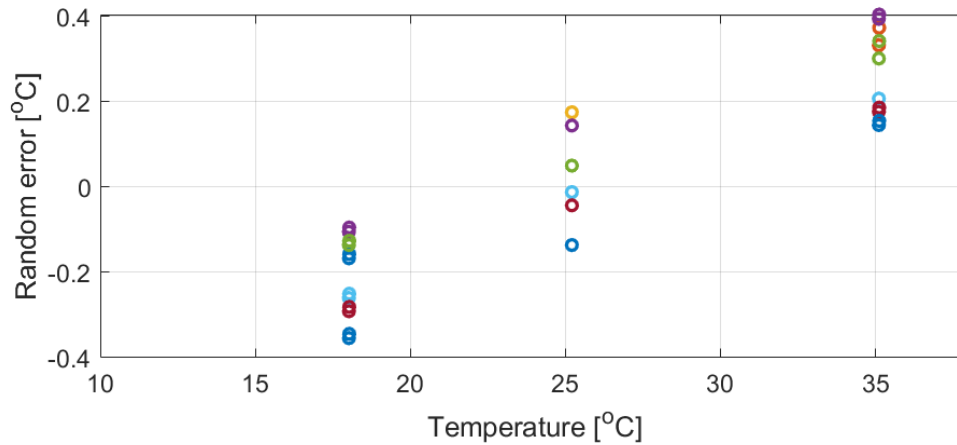


Figure 4.7: Random error for all thermocouples within the temperature range of the experiments.

The calibration of the pressure and flow sensors has been done in a similar fashion as the thermocouples. In the past accurate calibration measurements were done relating the voltage outputted by the sensors to the magnitude of the pressure and flow. The residuals of these calibrations were used to obtain the random error. Table 4.3 gives the maximum random error which were observed during calibration and the standard deviation of the errors. These values will be used in section 4.6. This section is dedicated to the propagation of the measurement error.

Table 4.3: Measurement devices with their maximum random error and the standard deviation of the random error based on the calibration data

| Measurement device | Maximum random error | Standard deviation |
|--------------------|----------------------|--------------------|
| Thermocouple | 0.40°C | 0.224°C |
| Flow sensor | 0.071 L/min | 0.0510 L/min |
| Pressure sensor | 0.18 mbar | 0.0369 mbar |
| Ruler | - | 1.50mm |

Table 4.3 also includes the values for the error of the ruler. The error of this measurement device could not be determined via calibration. It was estimated that the standard deviation of the error is 1.50mm.

The ruler is mounted to the PMMA-layer, which can be seen in Figure 4.5. In this figure it can already be seen that there is an offset between the start of the ruler and the bottom of the steel vessel. After thirty zero measurements it was determined that the offset amounted to 4.71cm. When the height measurement data is digitized, the offset is automatically subtracted from the obtained measured ruler heights.

4.5 Data conversion

From using the flow and temperature measurements the power can be calculated, using Equation 4.2 for the evaporator and using Equation 4.3 for the condenser.

$$P_{eva} = \rho \dot{V}_{eva} c_p (T_{eva,in} - T_{eva,out}) \quad (4.2)$$

$$P_{con} = \rho \dot{V}_{con} c_p (T_{con,in} - T_{con,out}) \quad (4.3)$$

With P the power (W), \dot{V} the volume flow (m^3/s) and $T_{in} - T_{out}$ the temperature difference between in and outflow ($^{\circ}C$).

Calculating the heat exchanger area for different heights is a challenge. It can be seen in Figure 4.3 that the heat exchanger does not have a simple geometry. An image recognition technique was used to determine the contact area between heat exchanger and bath water for different heights. The details of this model are explained in Appendix C. The relation between height and surface area according to the model is shown in Figure 4.8.

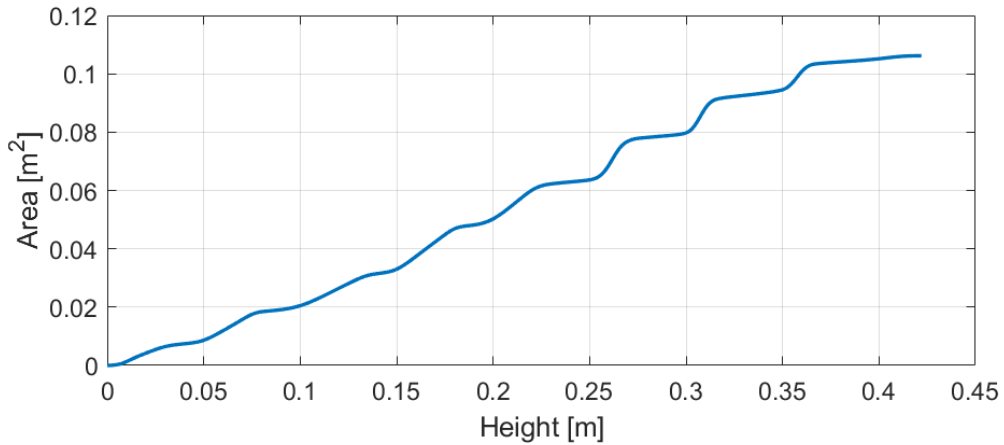


Figure 4.8: Relation between the height and the contact area between heat exchanger and water

The evaporator area (A_{eva}) can be seen as a function of the height (z). The function used in Equation 4.4 is visualized in Figure 4.8.

$$A_{eva} = f(z) \quad (4.4)$$

Using the power calculated in Equation 4.2 and the area calculated in Equation 4.4, the average heat flux of the heat exchanger (q''_{eva}) can be calculated using Equation 4.5.

$$q''_{eva} = \frac{P_{eva}}{A_{eva}} \quad (4.5)$$

The absolute pressure for a certain water column will be calculated using Equation 3.12, which was presented in the literature study. The thermophysical properties of water and steam, like saturation pressure and saturation temperature, were determined using steam tables produced by the IAPWS [57].

4.6 Error analysis

All measurements contain some degree of error. As mentioned in [subsection 4.4.2](#) the systematic error is compensated by the calibration, therefore only random error will be left in the measurements. There is a 95% probability that all random errors fall within the range of plus minus twice the standard deviation of the error [58]. The standard deviations of the random error per measurement device is presented in [Table 4.3](#). When calculations are made based on these measurements, this 95% certainty interval will propagate through the solution. For this research 95% certainty was considered acceptable. The absolute errors which are used for the following calculations are therefore twice the standard deviation.

The error of the power, which is calculated using [Equation 4.6](#), contains contributions of the error in flow ($\varepsilon_{\dot{V}}$) and the error of the two thermocouples ($\varepsilon_{T_{in}}$, $\varepsilon_{T_{out}}$).

$$\varepsilon_P = \sqrt{(\rho c_p (T_{in} - T_{out}) \varepsilon_{\dot{V}})^2 + (\rho \dot{V} c_p \varepsilon_{T_{in}})^2 + (-\rho \dot{V} c_p \varepsilon_{T_{out}})^2} \quad (4.6)$$

The error in area, which is calculated using [Equation 4.7](#), can be estimated by multiplying the derivative of the function given by [Figure 4.8](#) with the error in height (ε_z). The derivative of this function is provided in [Figure C.6](#).

$$\varepsilon_A = \left| \frac{\partial f(z)}{\partial z} \varepsilon_z \right| \quad (4.7)$$

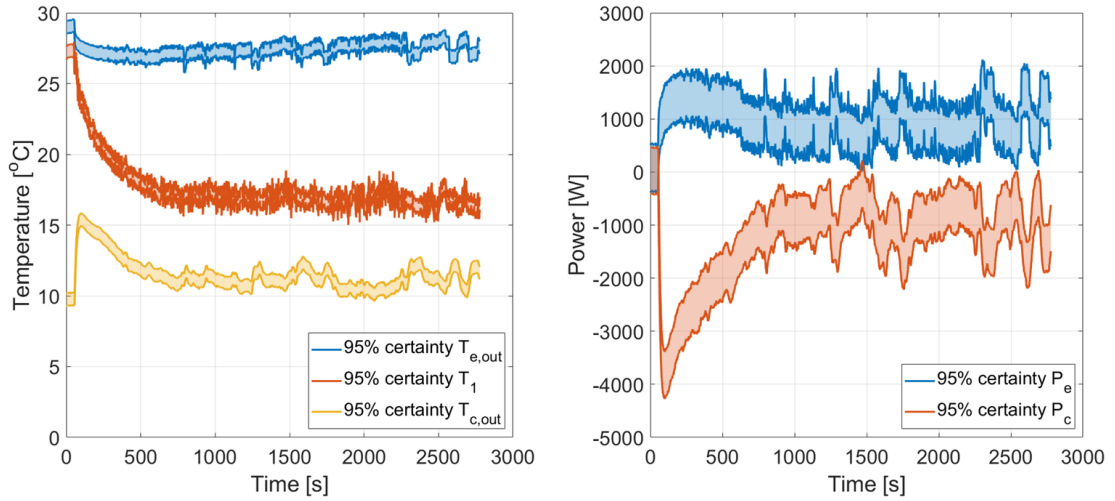
The error in heat flux can be calculated using the error in power (ε_P) and error in area (ε_A). The error equation is given by [Equation 4.8](#).

$$\varepsilon_{\dot{q}} = \dot{q} \sqrt{\left(\frac{\varepsilon_P}{P}\right)^2 + \left(\frac{\varepsilon_A}{A}\right)^2} \quad (4.8)$$

The error in absolute pressure, which is calculated using [Equation 4.9](#), contains contributions of the error in measured surface pressure (ε_{p_s}) and the error in measured height (ε_z).

$$\varepsilon_{p_{tot}} = \sqrt{(\varepsilon_{p_s})^2 + (\rho g \varepsilon_z)^2} \quad (4.9)$$

The 95% confidence intervals of some of the parameters are visualized in [Figure 4.9](#). [Figure 4.9 \(a\)](#) shows three temperatures which were measured during an experiment. A detailed explanation on what is exactly measured will be given in [section 5.1](#). The purpose of [Figure 4.9](#) is to visualize how big the confidence interval of the measurement data is. For every temperature the upper and lower bound is drawn and the area in between spans the 95% confidence interval. It can be observed that the certainty intervals are relatively small compared to the measured value. [Figure 4.9 \(b\)](#) shows the 95% confidence intervals of the calculated power of the evaporator (in blue) and condenser (in red). It can be seen that the certainty interval of the power is relatively larger, than for the temperature in [Figure 4.9 \(a\)](#). This is logical since the power is calculated using three measurement values which all have a random error.



(a) The evaporator outflow temperature (blue), a thermocouple in the water (red) and the condenser outflow temperature (yellow) (b) The power of the evaporator (blue) and condenser (red)

Figure 4.9: The confidence intervals for experiment data. The thicker lines are the upper and lower bound which denote the boundaries of the 95% confidence intervals.

From this point onward in the thesis, certainty intervals will not be included in the graphs. This is done to keep graphs with multiple lines clear and readable.

5.1 Typical system behaviour

Before presenting the influence of the hydrostatic pressure on the subatmospheric evaporation process, it is important to understand what is happening during a single experiment. This section will explain how the system, made up out of the condenser and the evaporator will respond, when the valve is opened.

All experiments follow the procedure described in [subsection 4.3.2](#). When the condenser and evaporator have reached their own steady state, the valve is opened. [Figure 5.1](#) provides a graph of the pressures, which are measured in the evaporator (blue) and in the condenser (red) during a single experiment.

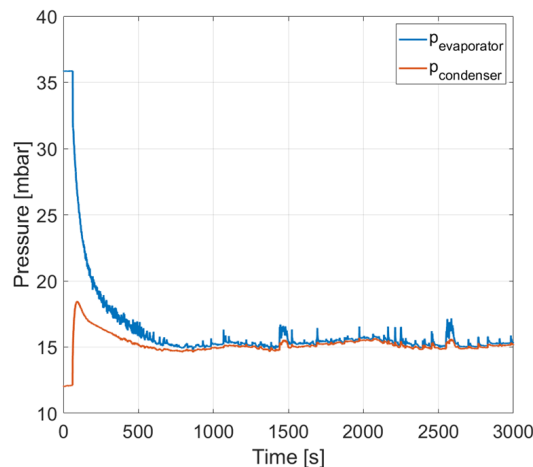
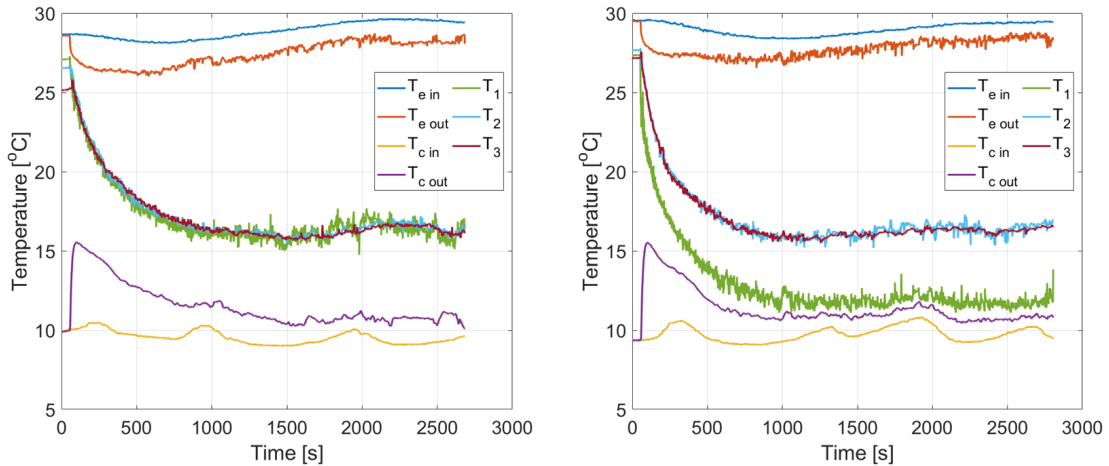


Figure 5.1: Measured pressures in the evaporator (blue) and the condenser (red) during an experiment with $z_{start} = 19\text{cm}$

At $t = 0\text{s}$ in [Figure 5.1](#) the valve is still closed. The pressures in both chambers are constant and equal to the saturation pressures of the water within the respective vessels. The starting pressure for the evaporator (blue) is 35.8mbar and the starting pressure for the condenser (red) is 12.0mbar . The pressure in the evaporator chamber is higher since the temperature of the water in the evaporator is higher than the water in the condenser. Assuming the vapor phases are fully saturated the water temperature of the evaporator is 27.1°C and the water temperature of the condenser is 9.7°C . These temperatures are in line with the measurements which will be presented in [Figure 5.2](#). At $t = 60\text{s}$ the valve is opened, both chambers are in contact with each other and the pressure difference starts to decrease fast. After some time the pressure difference is small. The pressure is around 15.5mbar here.

Figure 5.2 shows what happens to the temperatures in the system during a single experiment. The dark blue and light red line give respectively the inlet and outlet temperature of the evaporator. The yellow and purple line give respectively the inlet and outlet temperature of the condenser. The other lines represents the thermocouples which are placed in the evaporator chamber at different heights. The positions of the thermocouples were presented in subsection 4.2.1. With T_1 in green being the highest thermocouple, T_3 in dark red being the lowest and T_2 in light blue lying in between.



(a) Temperatures for an experiment with $z_{start} = 25\text{ cm}$ (b) Temperatures for an experiment with $z_{start} = 19\text{ cm}$

Figure 5.2: Temperature development during two experiments with different initial water heights

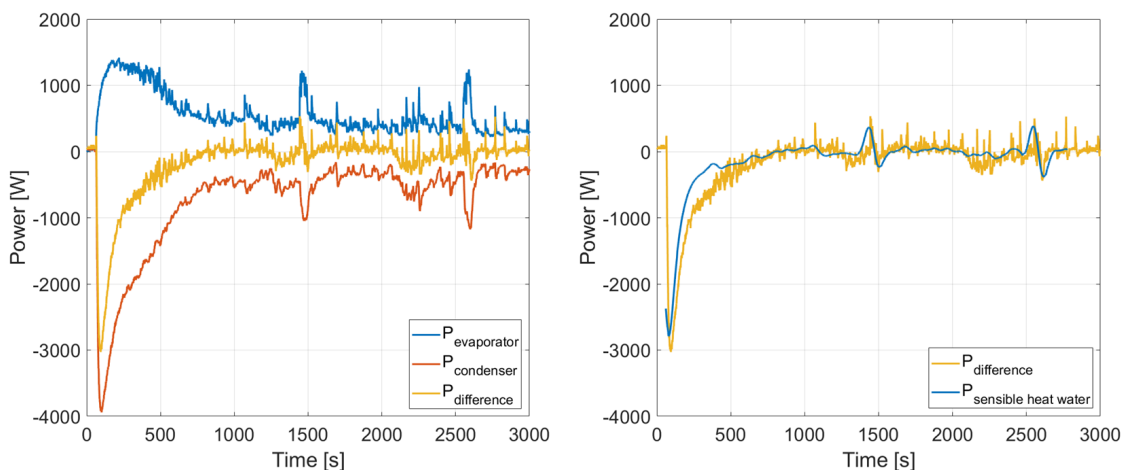
It can be seen in Figure 5.2 (a) that before the valve is opened, the inlet and outlet temperatures of the evaporator as well as the condenser are equal. This is in line with the experiment requirements mentioned in subsection 4.3.2. The experiment is started when both evaporator and condenser are at their own steady state, which means a negligible amount of power is transferred by the heat exchangers. So the inlet and outlet temperatures will be equal just before the valve is opened. It can be seen that the temperatures measured by the thermocouples in the evaporator water are not equal at the start of the experiment. This is due to thermal stratification: increasing the temperature of water will reduce its density. The water high in the bath will therefore be hotter than near the bottom. The temperature measured at T_1 is 2°C higher than at T_3 .

Then at $t = 60\text{ s}$ the valve opens. The evaporator and condenser will start transferring heat. The evaporator is adding heat to the system: the inlet temperature is higher than the outlet temperature. The condenser is subtracting heat from the the system: the inlet temperature is lower than the outlet temperature. The bath temperature will decrease when the valve has opened. The magnitude of the stratification disappears. It can be seen in Figure 5.2 (a), that high in the bath the temperature will reduce faster. During the transient phase the temperature near the water surface is lowest. Eventually the bath temperatures will reach a constant value. Note that the temperature measured near the water surface (T_1) fluctuates heavily compared to the temperature measured deeper in the bath. The magnitude of these temperature fluctuations is 2°C near the surface temperature compared to 0.3°C deep in the bath. It was ruled out that the big fluctuation near the water surface were due to the thermocouple itself. After physically changing the thermocouples, the same behaviour was observed: big fluctuations near the water surface and small fluctuations deeper in the bath.

Figure 5.2 (b) shows the temperature development of another experiment. In Figure 5.2 (a) the starting water height is 25cm and in Figure 5.2 (b) the starting water height is 19cm. It was mentioned in subsection 4.2.1 that T_1 is placed at $z = 21.7\text{cm}$. This means that in Figure 5.2 (b) T_1 is not placed in the fluid but in the gaseous phase. When comparing Figure 5.2 (a) to Figure 5.2 (b) only the temperature development of T_1 is different. The temperature of the vapor is lower than the liquid temperature when the valve is opened.

It can be seen in Figure 5.2 that the temperature differences between inlet and outlet temperature of the condenser and evaporator appear to have the same magnitude, especially at the second half of the experiment. It can also be seen in Figure 5.2 that there are periodic fluctuations in the condenser input temperature. This effect is caused by the control of the input variables and is already explained in subsection 4.3.2: the built-in controller regulating the condenser temperature has a high gain factor, compared to the evaporator temperature. This causes the condenser inlet temperature react more aggressively to an overshoot of the set value of 10°C .

Using Equation 4.2 and Equation 4.3 the powers during an experiment can be calculated. Figure 5.3 (a) shows how the power changes in time when the valve is opened.



(a) Measured powers in the evaporator (blue), the condenser (red) and the difference between the two powers (yellow) during an experiment.

(b) The power difference from Figure 5.3 (a) plotted against the power produced by the sensible heat of the water, calculated using Equation 5.1.

Figure 5.3: The development of the powers during an experiment with $z_{\text{start}} = 19\text{cm}$

It can be seen in Figure 5.3 (a), that before the valve is opened (before $t = 60\text{s}$) the powers are negligible since both condenser and evaporator are at their own closed system steady state. The power of the evaporator (in blue) is positive, since energy is supplied to the system. The power of the condenser (in red) is negative, since energy is subtracted from the system. The yellow line is the sum of both powers.

The yellow line in Figure 5.3 (a) shows that when the valve opens, much more energy is subtracted from the system than supplied to the system. After some time this difference goes to zero. This power difference is due to the cooling of the water. As the valve opens the pressure in the evaporator decreases fast (as seen in Figure 5.1) causing a bath temperature to decrease (as seen in Figure 5.2). The power generated by cooling the liquid can be calculated using Equation 5.1.

$$P_l = \rho_l V_l c_p \frac{\partial T_l}{\partial t} \quad (5.1)$$

In Figure 5.3 (b) the power difference as seen in Figure 5.3 (a) is plotted against the power from cooling the liquid, calculated using Equation 5.1. The water temperature (T_l) was found by smoothing the measurement data of the thermocouple in the water and the volume (V_l) was determined using the water height measurements. More detail on how the volume is calculated from the water height can be found in Appendix C. It can be seen that the curves in Figure 5.3 (b) are in good agreement. This means that at the start of the experiment a considerable amount of energy is subtracted from the water itself. From now on in this thesis the sum of evaporator and condenser power is called the power due to water cooling.

The curves given in Figure 5.3 (a) can also be linked to the boiling behaviour which is observed. In Figure 5.4 on the left side three snapshots of the water surface are given at different times. On the right side the powers at the same times are given. In **snapshot A** the valve is still closed. This results in a negligible amount of heat transfer and no bubble formation. In **snapshot B** the valve has just opened, but there is still a reasonable pressure difference between the evaporator and the condenser. The bath water is in the process of cooling rapidly. Very violent bubble formation is occurring everywhere on the water surface. In **snapshot C** there is barely any pressure difference between the evaporator and the condenser. The bath has reached a steady temperature. Bubble formation only occurs on the heat exchanger near the water surface (like the vapor bubble in the lower left corner in Figure 5.4).

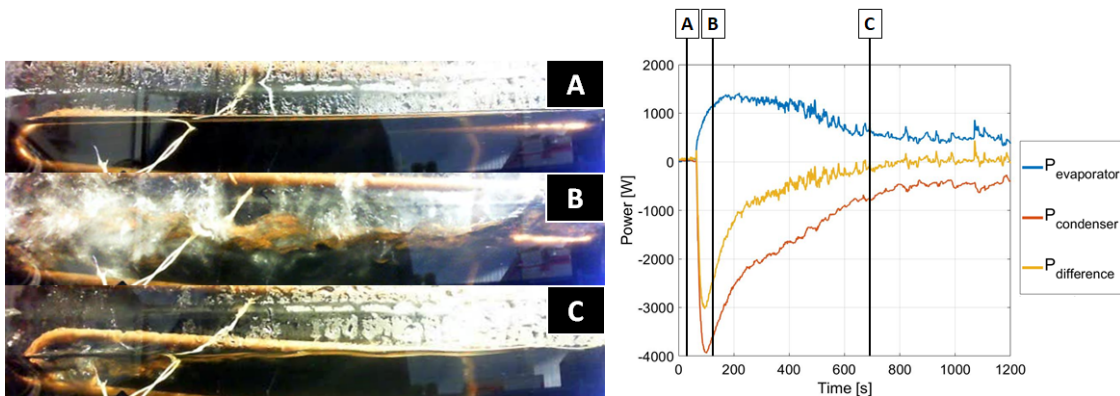


Figure 5.4: Three snapshots of the boiling behaviour at the surface, linked to the power curve of Figure 5.3 (a). **A:** the valve is still closed, each chamber is at its own steady state, negligible heat transfer and no boiling, **B:** the bath is in the process of cooling, violent bubble formation everywhere on the water surface. **C:** the bath has reached a steady state temperature, only bubble formation on the heat exchanger surface.

It is becoming clear that two distinct phenomena are occurring, when the valve opens: cooling of the volume of water due to the pressure decrease and heating of the volume of water due to the heat transfer from the heat exchanger. When the system is in imbalance the boiling behaviour is very different from when the water has reached a steady state. Therefore it was chosen to split up the measurement data in a transient and a steady water temperature part and study the influence of the hydrostatic pressure on both regimes.

The border between the transient and steady regime is determined in this thesis using the pressure difference between the evaporator and condenser. When this pressure difference goes

below a threshold value the data is split up. For the data up until [section 5.3](#) this threshold pressure difference was chosen to be 0.9mbar . This value was chosen based on the observed boiling behaviour and the power curves for all experiments. [Figure 5.5](#) provides the location of the data split (the vertical dotted line), on top of the power curves, for two different experiments with different starting heights.

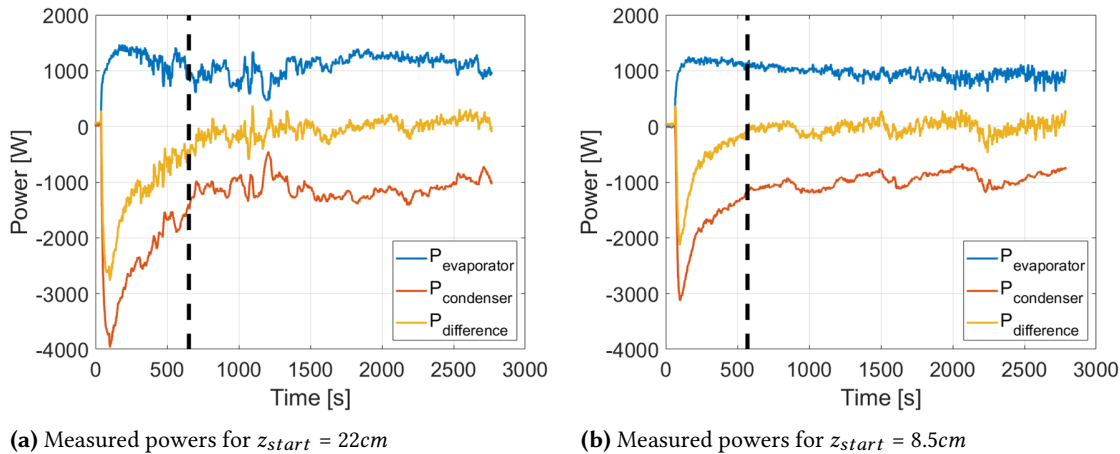


Figure 5.5: Measured powers in the evaporator (blue), the condenser (red) and the power due to water cooling (yellow) during two experiments with different starting heights. The border between transient and steady regime is given by the black dotted line in both figures.

It can be seen in [Figure 5.5](#) that the course of the power curve is indeed very different left and right of the black dotted border. Left of the dotted line is what will be called the transient regime in this thesis. Right of the dotted line is what will be called the steady regime in this thesis. When comparing the location of the border of [Figure 5.5 \(a\)](#) and [Figure 5.5 \(b\)](#) it can be seen that for a larger water height it takes longer to reach the steady regime. This is logical since more sensible heat is stored in the larger quantity of water. It will take longer for the water to cool down and therefore longer for the pressure difference to decrease.

5.2 Influence of hydrostatic pressure

5.2.1 Transient evaporation regime

In the transient regime the water is cooling. As long as the water has not reached a steady temperature, there still is a considerable amount of pressure difference between the evaporator and condenser. It was decided to plot the data in the transient regime as three dimensional contour plots. The water column height (which scales linearly with the hydrostatic pressure) was placed on the x-axis, the pressure difference on the y-axis and the relevant parameter was mapped on this grid with isosurfaces. The colours of these isosurfaces correspond to the minimum values observed within the indicated areas. These maps are based on 8 experiments with different initial heights.

The power provided to the condenser due to the cooling of water (which is defined by [Equation 5.1](#)) is mapped in [Figure 5.6](#), for different heights. The power is defined as positive when the water gives off energy to the condenser.

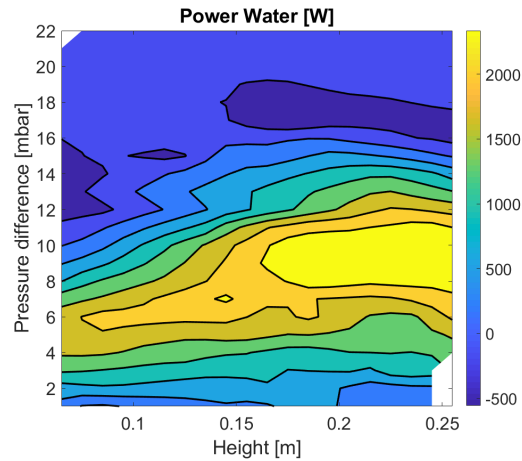
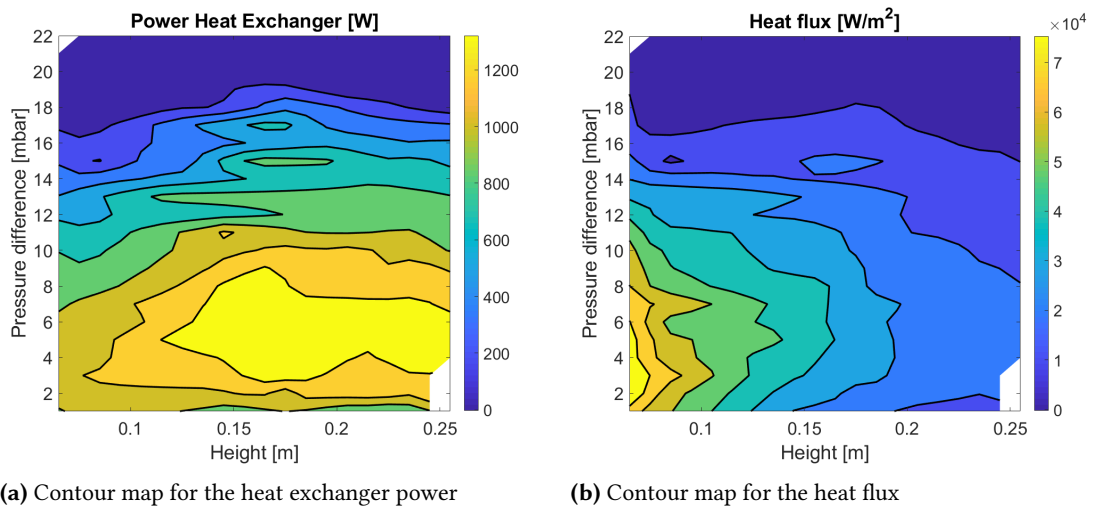


Figure 5.6: Contour map of how the power subtracted from the water, during the transient regime of the experiment, is related to the pressure difference between evaporator and condenser and the water height.

From Figure 5.6 a few conclusions can be drawn. At a certain pressure difference there is a maximum amount of power subtracted from the water. With increasing water height the pressure at which the maximum power is subtracted also increases slightly. Also the magnitude of the power increases with increasing water height, but from 17cm onward the increase is small. The increase in power is logical since more energy is stored in a larger volume of water. The water surface can only transfer a limited amount of power for a certain pressure difference. This explains why the magnitude of the power barely increases over 17cm and stays between 2500 and 2700W here. It can be seen in Figure 5.6 that when the valve has just opened and the pressure difference is still relatively high, power is actually being supplied to the water. This is most likely due to the measurement error when the valve has just opened.

Figure 5.7 shows the contour maps of the transient regime for the heat exchanger performance variables: power and heat flux. The definition of the heat exchanger power in Figure 5.7 (a) was given in Equation 4.2. The definition of the heat flux in Figure 5.7 (b) was given in Equation 4.5.



(a) Contour map for the heat exchanger power

(b) Contour map for the heat flux

Figure 5.7: Contour maps of the heat exchanger performance variables plotted against the pressure difference between evaporator and condenser and the water height.

Figure 5.7 (a) shows the contour map for the transient response of the heat exchanger power to the water cooling for different water heights. It can be seen that the maximum heat exchanger power increases with increasing water height but from 14cm onward the maximum power stays relatively constant between 1350 and 1450W.

Figure 5.7 (b) shows the contour map for the heat flux during water cooling for different heights. It can be clearly seen that the heat flux increases with decreasing water height. This is logical result since it was observed in Figure 5.7 (a) that the values for heat exchanger power are relatively constant. The effective heat exchanger area, on the other hand, increases relatively a lot with increasing water height, as can be seen in Figure 4.8. The heat transfer appears to be much more effective for lower water levels.

5.2.2 Steady evaporation regime

This subsection presents the effect of the hydrostatic pressure (which scales linearly with the water height) on the evaporation behaviour, when the bath water has reached a steady temperature. There are still some fluctuations in bath temperature visible, especially near the water surface (as seen in Figure 5.2), but the difference between evaporator and condenser power is negligible. In contrast with the transient evaporation regime bubble formation is only observed on the heat exchanger surface near the water surface. The data of the heat exchanger performance variables as a function of the water height is presented in Figure 5.8.

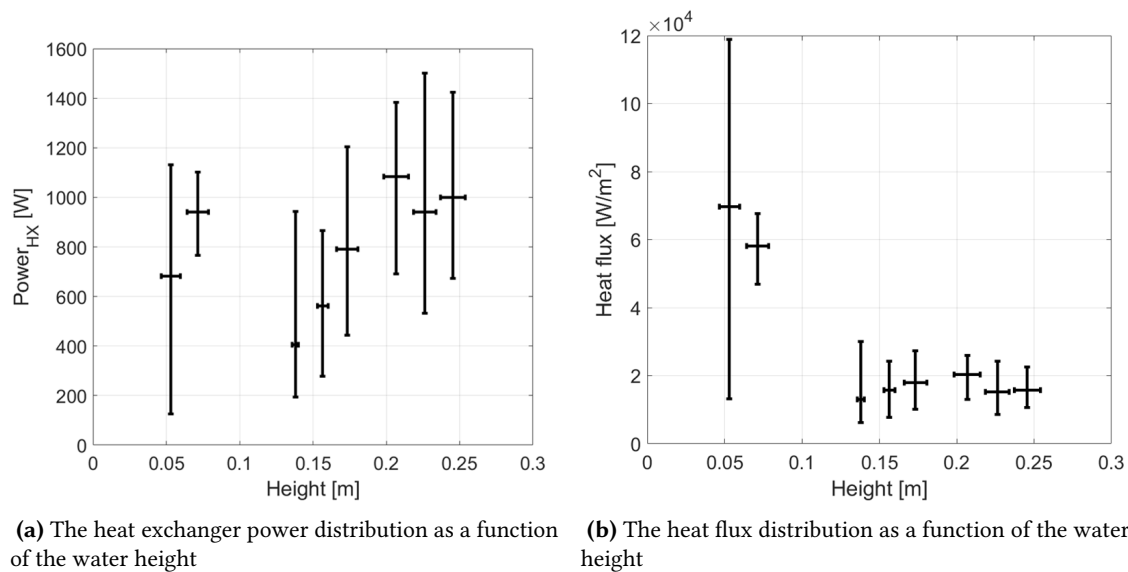


Figure 5.8: Relation between the magnitude of the heat exchanger performance variables and the water height in the steady regime of the experiment. The error bars are chosen to fit 95% of the data distribution.

During the steady regime both the power and water height vary in time. If all this data was plotted in Figure 5.8 as individual data points the figure would become cluttered, especially for 8 separate data sets. To turn the data into a readable graph it was chosen to visualize the data as 2D error bars. The centre point of every error bar is the mean value of the height and power during the measurement. It is assumed that the decrease of water height follows a normal distribution. The total span of the horizontal error bars is 4 times the standard deviation of the height data.

The distributions of the steady regime power data was also analysed. It turned out, that in particular the power measurements for a low column height, did not match a normal distribution. Most of them could better be described using a bimodal distribution. Appendix D contains graphs of the power distributions and an explanation where the bimodal distribution might originate from. The span of the vertical error bars in Figure 5.8 (a) was chosen in such a way that 95% of the data points are covered by the error bars. The same thing is done for the heat flux in Figure 5.8 (b).

Figure 5.8 (a) shows the power of the heat exchanger, as defined by Equation 4.2, for 8 different heights in the steady regime. Figure 5.8 (a) shows on average an increase of heat exchanger power with increasing water height. It can be seen that the three experiments with the highest water column have generally more power than the lower ones. This increase in power is most likely caused by the increase in effective heat exchanger area. It has to be noted that although the average heat exchanger power increases with increasing water height, the spread of the power data is large.

Figure 5.8 (b) shows how the heat flux rapidly decreases with increasing water height, a phenomenon also observed in the transient relation between the heat flux and the water height in Figure 5.7 (b). After a rapid decrease in average heat flux the value stays relatively constant from 14cm onward between 14 and 20 kW/m^2 . It can be concluded that the heat transfer and therefore steam production is much more effective for low water levels. The reason behind this effect will be further investigated in section 5.4.

One could argue that nucleate pool boiling is only occurring near the water surface because of the flow direction of the hot flow through the heat exchanger. As seen in the schematic setup in Figure 4.1, the hot flow enters the bends of the heat exchanger from the top. This means that the heat exchanger surface is the hottest near the water surface. One could therefore argue that nucleate pool boiling is occurring near the water surface because the heat exchanger is simply the hottest here. According to this reasoning the bottom of the heat exchanger would simply have too little excess temperature for nucleate pool boiling. To examine this theory the flow direction, through the evaporator, was reversed. In the new experiments the bends of the heat exchanger at greater depth are hotter than the bends near the water surface. Four experiments with the reversed flow direction were performed for different water heights to see if the results or the

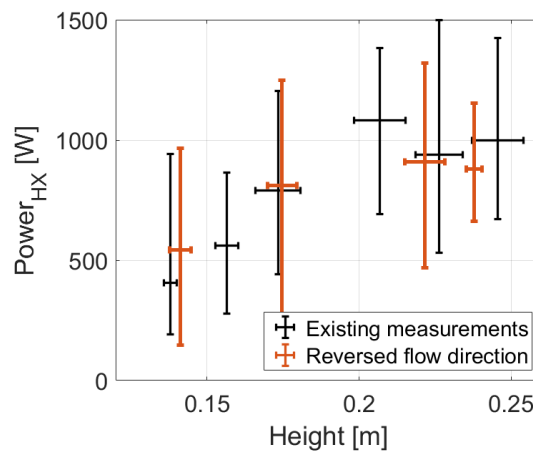


Figure 5.9: The steady regime heat exchanger power as a function of water height. In black the experiment results already seen in Figure 5.8 (a) and in red the experiments for the reversed flow direction.

observations changed. [Figure 5.9](#) contains the heat exchanger power distributions against water height for the reversed flow direction in red. These are compared to the data of [Figure 5.8 \(a\)](#) in black.

In [Figure 5.9](#) it can very clearly be seen that the power of the heat exchanger is not influenced by the flow direction. The red and black error bars nicely coincide. From the observations it was concluded that the height at which vapor bubbles were formed did not change, compared to the other flow direction. Even though the bottom of the heat exchanger was hotter, only nucleate pool boiling was observed near the water surface. This experiment rejects one of the assumptions made in the hypothesis presented in [chapter 2](#): The temperature difference over the heat exchanger does not influence the way how convection pool boiling and nucleate pool boiling coexist in the water.

5.3 Improving evaporation behaviour

From the experimental results so far, a lot of insight was gained in the subatmospheric boiling behaviour in a thermochemical storage system setting. Nucleate pool boiling was only observed in a small layer near the water surface. The vast majority of the water transfers heat via convection pool boiling, which transfers far less heat per surface area than nucleate pool boiling (as seen in [Figure 3.8](#)).

5.3.1 New heat exchanger

A new heat exchanger was created with the idea to increase the section of water in which nucleate pool boiling takes place. [Figure 5.10](#) shows the new heat exchanger. It is made out of the exact same material as the previous heat exchanger: Copper pipe with the same surface roughness ($Ra = 0.5\mu m$), an outside diameter of $10mm$ and a wall thickness of $1mm$. The total length of pipe used is $13.8m$. This makes the surface area a factor 4.4 larger compared to the previous heat exchanger. The copper pipe is wound in a spiral with varying diameters. The copper pipes are bent in such a way that there is a clearance between the pipes. Touching pipes could create nucleation points which would locally enhance the boiling performance. But this would influence the experiment data in such a way that the relation between boiling performance and hydrostatic pressure would become distorted. Because of the three dimensional shape of the heat exchanger it is not possible to construct a surface area model using the technique presented in [Appendix C](#). Therefore the experimental results for the spiral heat exchanger will only be presented in terms of power and not heat flux.

The idea behind the new heat exchanger in [Figure 5.10](#) is that more power can be transferred, deeper in the bath. The three dimensional spiral shape could increase the temperature deeper in the bath, which would result in a larger section of the water contributing to the pool boiling, thus transferring more heat. With the spiral heat exchanger the ratio between heat exchanger and amount of water becomes more realistic, since the volume of the evaporator chamber is more effectively used.



Figure 5.10: Left: a top view of the spiral heat exchanger. Right: a side view of the spiral heat exchanger.

Because the new heat exchanger needs to be installed in the evaporator test chamber, the thermocouples in chamber as schematically seen in Figure 4.1 need to be detached. The thermocouples are reattached at different heights, which were carefully measured. For the second set of experiments the heights of the thermocouples were: T_1 at $z = 18.8\text{cm}$, T_2 at $z = 10.3\text{cm}$ and T_3 at $z = 0.2\text{cm}$. All these heights were measured from the bottom of the evaporator test chamber.

5.3.2 Typical system behaviour compared to old heat exchanger

A few differences can be observed when comparing the typical system behaviour of the new heat exchanger with the old one. These differences are summed up in words instead of figures, to keep the subsection concise:

- The heat exchanger power is much higher for the new evaporator. The larger surface area can transfer a lot more heat. For the new heat exchanger the typical steady state powers are around 1.9kW instead of around 0.8kW for the old heat exchanger.
- The starting temperatures of the bath (when the valve is still closed) are higher for the new heat exchanger. The larger heat exchanger area results in a higher steady state temperature of the water. For the new heat exchanger the maximum initial temperature is 31°C instead of 28°C for the old heat exchanger.
- The higher starting temperatures do also result in higher starting pressures in the evaporator chamber. Since the saturation pressure increases with temperature. For the new heat exchanger the initial pressures are around 43mbar instead of 35mbar for the old heat exchanger.
- The bath temperature in the steady regime is higher for the new heat exchanger. The higher heat exchanger power causes the steady state temperature to settle at a higher value. For the new heat exchanger the typical steady state temperature is around 21°C instead of around 16°C for the old heat exchanger.
- During the steady regime of the experiment the pressure difference between evaporator and condenser is around 3mbar with the new heat exchanger. With the old heat exchanger the pressure difference was around 0.5mbar . The higher heat exchanger power can keep the bath at a higher steady state temperature. The water in the condenser is also at a higher steady temperature 13.5°C instead of 11°C , but the temperature difference between the two baths is higher for the new heat exchanger.

- The threshold pressure difference, which is used to split the data in a transient and steady regime, is determined to be 3mbar for the new heat exchanger. For the old this threshold pressure difference was 0.9mbar .

5.3.3 Transient evaporation regime

In the transient regime the water is cooling down due to the fact that the pressure at the water surface is lower than the saturation pressure of the water. Eventually these pressures will stabilize and the water temperature will be relatively constant in the steady regime. The contour maps for the new heat exchanger are presented in [Figure 5.11](#).

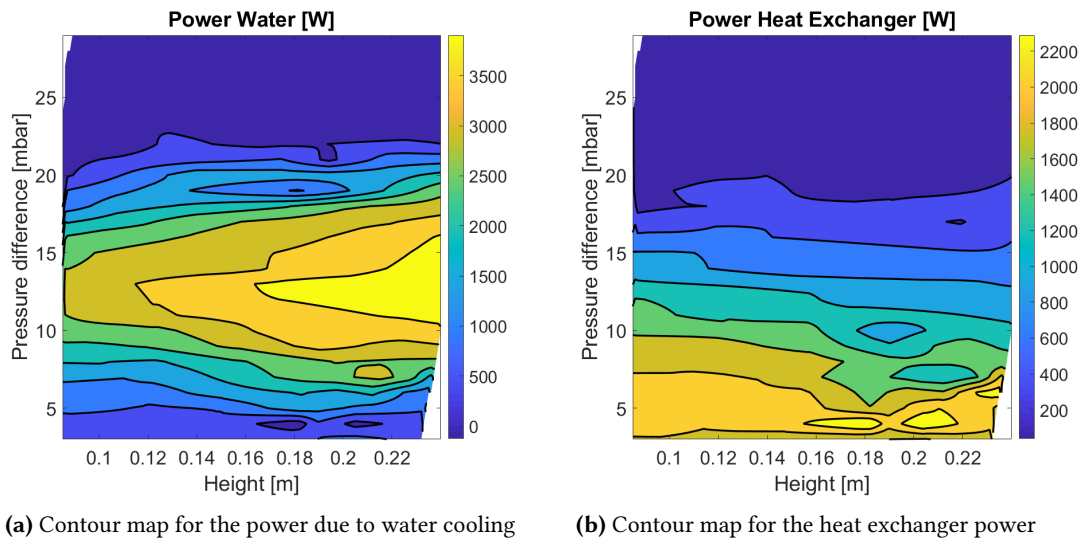


Figure 5.11: Contour maps of the transient regime for the experiment with the new heat exchanger. The magnitude of power from the water and heat exchanger power is plotted against the pressure difference between evaporator and condenser and the water height.

[Figure 5.11 \(a\)](#) gives a contour map on how the pressure difference and water height will relate to the power from the water, based on 6 experiments with varying height. Comparing this contour map to the contour map of the old evaporator in [Figure 5.6](#), it becomes apparent that the shapes are equal. For the new condenser the maximum occurs at a higher pressure difference (13mbar instead of 9mbar) and the magnitude of the power is much higher (4.3kW instead of 2.6kW). Due to the higher starting temperature, the pressure difference at the start is higher and more power is transferred over the water surface. This explains both the shift of the maximum compared to the old heat exchanger and the increased magnitude.

[Figure 5.11 \(b\)](#) contains the contour map of the heat exchanger power during the transient regime. When comparing the map to the contour plot of the old heat exchanger in [Figure 5.7 \(a\)](#), it can be seen that the magnitude of the power has increased massively (2.5kW instead of 1.4kW). The pressure difference at which the maximum occurs has stayed the same.

5.3.4 Steady evaporation regime

In the steady regime the water temperature is no longer cooling. There are still fluctuations in water temperature, but the average power from the water is equal to zero. Figure 5.12 shows the relation between the heat exchanger power and the water height, which scales linearly with the hydrostatic pressure. The error bars are there to illustrate the magnitude of the fluctuations in power and height. The length of the bars are constructed using the method which is explained in subsection 5.2.2.

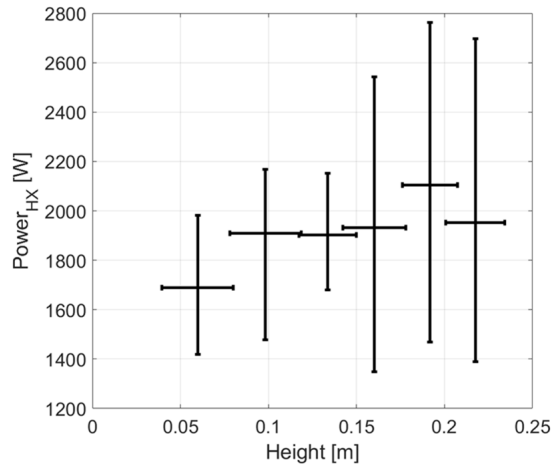


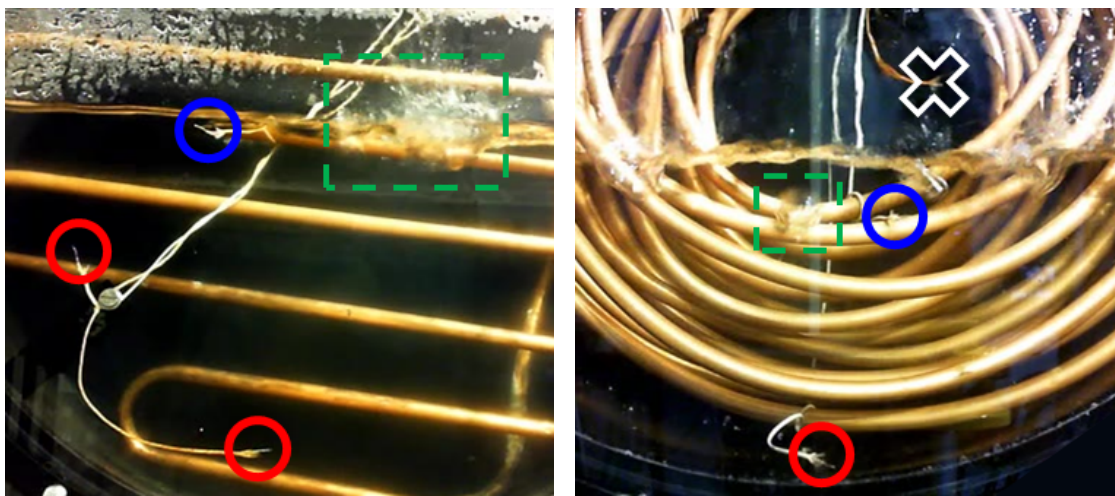
Figure 5.12: The heat exchanger power of the larger heat exchanger, during the steady regime of the experiment, as a function of the water height. The error bars chosen to fit a 95% of the data distribution.

It can be seen in Figure 5.12, that the power increases with increasing water height due to the larger contact area between water and the heat exchanger. There appears to be a linear relation between the average power and the water height. It must be said that the spread of the power data is big compared to the increase in average power due to the increasing water height. A comparison of the steady regime of the new heat exchanger (in Figure 5.12) to the old heat exchanger (in Figure 5.8 (b)) shows that on average the magnitude of power has more than doubled. Also the error bars in horizontal direction are much wider for the new heat exchanger. This is logical since higher powers will result in more evaporation, causing a larger water height decrease during the span of the experiment.

It was mentioned earlier that the shape of the heat exchanger was so complex that no relation describing effective surface area as a function of water height could be constructed. Nevertheless, an estimation can be made on how the heat flux of the new exchanger compares to the heat flux of the old exchanger. The surface area of the new heat exchanger is a factor 4.4 larger compared to the old heat exchanger, but the heat exchanger power is only 2.4 times larger. It can therefore be concluded that the heat flux for the new heat exchanger is far lower compared to the old heat exchanger. Increasing the surface area deeper in the bath did not have the desired effect, discussed in section 5.3. The excess temperature deeper in the bath did not increase and no vapor bubble formation could be detected at any points deeper when compared to the experiments with the old heat exchanger. Actually the opposite effect occurred: the increased surface area of the new heat exchanger contributed far more to convection pool boiling than to nucleate pool boiling, resulting in an on average lower heat exchange per surface area.

5.4 Boiling regimes

Using the measured height of the water level, the height of the thermocouples and the measured pressure at the surface, it is possible to calculate the absolute pressure at the thermocouples using Equation 3.12. In the steady regime the temperature is relatively constant. The absolute pressure can be plotted against the measured temperature. These data points can be plotted alongside the equilibrium curve for water, as is done in Figure 5.14 (a). The data points can also be combined with visual observations. All experiments were filmed. By watching the time lapse of the experiments it is possible to distinguish whether nucleation boiling is occurring at the height of each thermocouple. Figure 5.13 shows how it was determined whether nucleate pool boiling occurred at a certain height. Figure 5.13 is based on a snapshot of the time lapse for illustrative purposes. In reality the boiling behaviour classification is based on the whole time lapse of the steady regime.



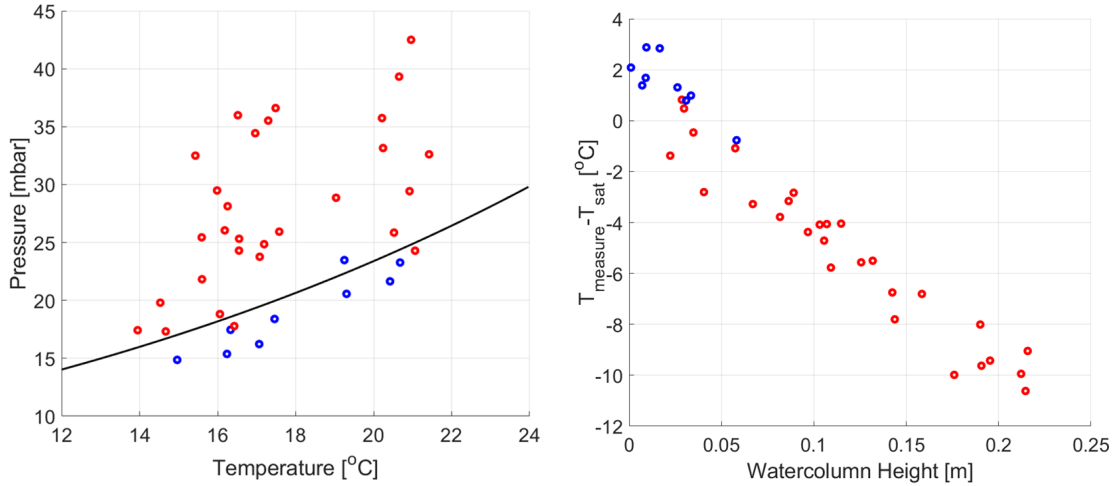
(a) Nucleate pool boiling observed for experiment with the 2D heat exchanger

(b) Nucleate pool boiling observed for experiment with the 3D spiral heat exchanger

Figure 5.13: Snapshot of two experiments: In the green dotted square the observed vapor bubble formation, in the blue circle the thermocouples at the heights where bubble formation is observed, in the red circle the thermocouples at the height where no bubble formation is observed and in the white cross the thermocouples of which the measurements are not included in Figure 5.14.

Figure 5.13 shows snapshots of two experiments with different heat exchangers in which nucleate pool boiling was observed. The observed pool boiling phenomena are in the green squares. The other indicators in Figure 5.13 are there to point out the thermocouples in the test chamber. The blue circles are placed at the height where nucleate pool boiling was observed. The red circles are placed at the heights where no bubble formation was observed during the entire duration of the steady regime. The white cross indicates the thermocouples which are not in the liquid phase. These thermocouples measure the temperature of the vapor phase and are therefore not included in the boiling regime curves in Figure 5.14.

Figure 5.14 (a) shows a pressure versus temperature diagram. The black line is the equilibrium curve for water. The colours of the data point correspond to the colours with which the thermocouples are indicated in Figure 5.13. The red points are the data points where no bubble formation was observed, so at these points convection pool boiling is occurring. At the blue data points bubble formation is observed, so nucleate pool boiling is observed at these heights.



(a) Absolute pressure against the measured temperature for the experiment data. The black line is the equilibrium line for water. (b) The temperature difference between the measured value and the saturation temperature for the absolute pressure against the water depth.

Figure 5.14: Boiling regime curves: with nucleate pool boiling represented by the blue data points and no bubble formation was observed by the red points.

It can be seen in Figure 5.14 (a) that at most data points below the equilibrium line nucleate pool boiling was observed, while at the vast majority of the points above the equilibrium line no vapor bubble formation were observed. Red points below the equilibrium line can be explained: The observations are based on a time lapse which captures one frame rate per second. It would theoretically be possible that no bubble formation is observed even though bubbles were actually formed at that height during the experiment. Blue points above the equilibrium line can also be explained. The data points resemble the average pressure and average temperature which were observed during the experiment. To keep the graph readable no distributions were included. It would be possible that in time the conditions would be such that the absolute pressure would be under the equilibrium line (making nucleate pool boiling possible), while on average the absolute pressure in the experiment is above the equilibrium line.

Figure 5.14 (a) also says something about how changing the heat exchanger influences the boiling regimes. All data points between 14 and 18°C belong to the experiments with the small 2D heat exchanger. All data points between 19 and 22°C belong to experiments with the large spiral heat exchanger. It can be seen that by increasing the power the data points shift to a higher temperature along the equilibrium line. This disproves the idea proposed in section 5.3, that increasing the surface area and the power, could locally result in higher temperatures, which would make nucleate pool boiling deeper in the bath possible. Instead, increasing the surface area results in an overall temperature shift of the data points along the equilibrium curve.

Figure 5.14 (a) says something about the absolute pressure but not about the contribution of the water column height. Figure 5.14 (b) presents the influence of the water column height on the boiling behaviour. On the x-axis the water height above the thermocouple is given and on the y-axis the difference between the measured water temperature and the saturation temperature for each point in Figure 5.14 (a) is given. If $T_{measure} - T_{sat}$ is positive the data point is below the equilibrium curve. If $T_{measure} - T_{sat}$ is negative the data point is above the equilibrium curve. In Figure 5.14 (b), like in Figure 5.14 (a), nucleate pool boiling is represented by blue dots and convection pool boiling is represented by red dots.

At water depths between 0 and 2.2cm only nucleate pool boiling was observed. At water depths between 2.2 and 5.8cm both nucleate pool boiling and convection pool boiling can occur. Deeper than 5.8cm no vapor bubble formation could be observed.

6

Water vapor inlet boundary condition for numerical reactor model

6.1 Background

Previously a numerical study was performed, commissioned by *De Beijer RTB BV*, which focused on the interaction between the vapor and the reactor material [59]. In that numerical study coarse approximations were made about the evaporation behaviour. These approximations do not match with the results obtained in the experimental study presented in section 5.1. The goal of this chapter is to present a method to better model subatmospheric evaporation. This will result in a more realistic interaction between evaporator and reactor, compared to the current model.

Figure 6.1 presents the geometry and boundary conditions of the existing model [59]. This particular reactor has a so called E-Pad shape: a scale-shaped copper fin which is filled with TCM. The centre of the copper fin is connected to a heat exchanger tube, through which water flows. The E-Pad is made in such a way that multiple scale-shaped fins filled with TCM can be connected in series to the heat exchanger pipe. This configuration makes up the entire reactor. This reactor is placed above the evaporator/condenser in a vacuum. This reactor configuration is modeled as a single 2D axisymmetric E-Pad, which is seen in Figure 6.1. All boundaries are numbered and explained in the diagram legend. This part of the thesis will focus on improving boundary condition 1: the water vapor inlet. The exact configuration of the reactor is not important for the analytical model, which will be presented in this chapter, to describe the evaporation behaviour. As long as the models with different reactor configurations are built up the same way, any reactor can be connected to the analytical model describing the subatmospheric evaporator behaviour.

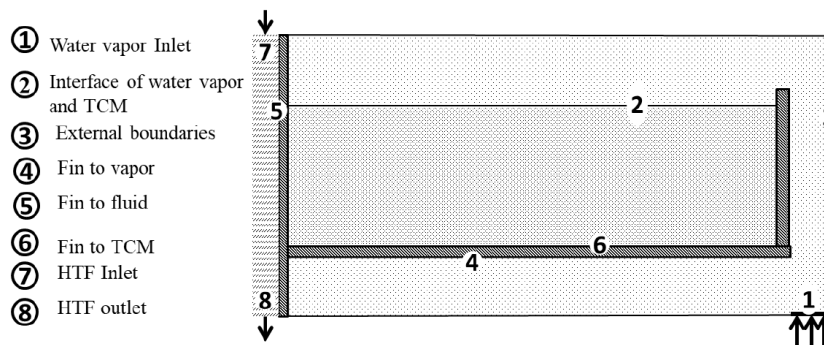


Figure 6.1: Geometry and boundaries of the existing numerical reactor model [59]

Boundary 1 in Figure 6.1 is the connection between the reactor and the evaporator. On this boundary the evaporator pressure (p_{eva}), evaporator temperature (T_{eva}) and vapor concentration (c_{eva}) are prescribed. In the current numerical reactor model all these parameters are assumed to be constant, but it became clear from the experiments that all three parameters differ in time. To make the water vapor inlet boundary for the existing model more realistic, a simple analytical model is created.

6.2 Model implementation and assumptions

The analytical model is built to represent the experimental setup described in [chapter 4](#). This way the analytical results can be validated against the experiment data. The experimental setup contains a condenser instead on a reactor. The evaporator and condenser are modeled. The idea is that after the model is verified, the condenser could be exchanged for the existing numerical reactor model.

6.2.1 Assumptions

The following rough assumptions were made in the analytical model:

- Water vapor behaves as an ideal gas. This means that the water vapor concentration can be calculated using [Equation 6.1](#).

$$c_{eva} = \frac{p_{eva}}{R_u T_{eva}} \quad (6.1)$$

With c_{eva} the vapor concentration (mol/m^3), p_{eva} the evaporator pressure (Pa) and T_{eva} the evaporator gas temperature (K).

- The water vapor is fully saturated at every point in time.
- The condenser is overdimensioned: The water temperature in the condenser will be constant during the whole course of the simulation. All energy absorbed by the water will be directly discharged by the heat exchanger.
- The system is modeled as 4 lumped masses, which can exchange mass and energy. The 4 masses are the liquid and vapor in the evaporator and the liquid and vapor in the condenser. This simplification indicates that there are no temperature gradients within each mass and all masses are stationary.
- The volumes available for the vapor phases are assumed to be constant during the simulation.
- The vapor transport between the two chambers is based on free expansion. The pressures in both chambers will evolve to an equilibrium pressure, with an exponential decay caused by the production and consumption of vapor.
- The steady state pressure difference between the two chambers, caused by the pressure drop over the valve, is assumed to be constant.

6.2.2 Model implementation

The model of the evaporator and condenser setup is schematically drawn in [Figure 6.2](#). The four lumped masses are visualized by the blue rectangles, dark blue for liquid and light blue for vapor. In each lumped mass the corresponding variables are visualized in white circles. For the liquid masses the temperature and the mass are given. For the vapor masses the temperature, mass and pressure are important. The green arrows indicate the vapor fluxes in the model. The red arrows represent the energy fluxes in the model. The pink dotted square represents the part of the model which could be exchanged for the existing numerical reactor model.

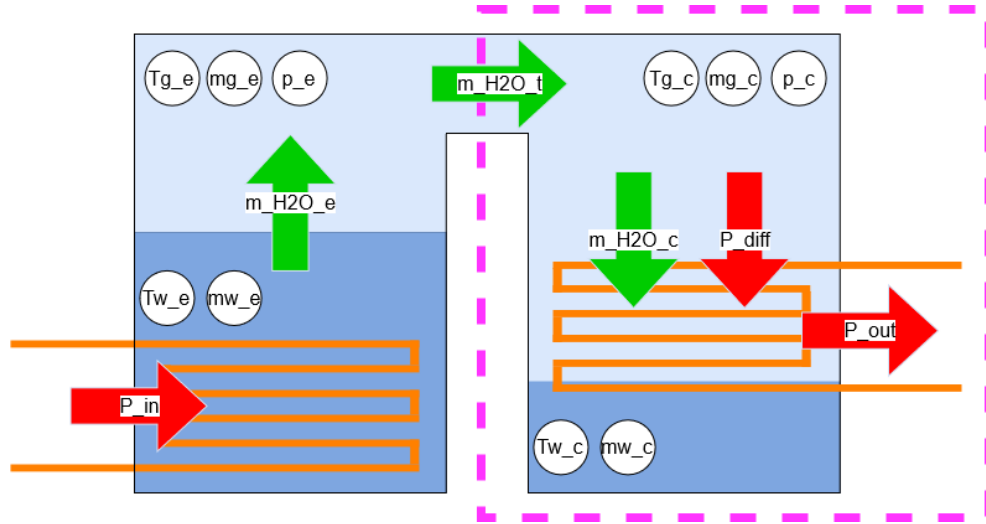


Figure 6.2: Schematic drawing which represents the numerical model. The red arrows represent heat transfer and the green arrows represent mass transfer. The pink dotted square represents the part which will eventually be replaced by the existing numerical reactor.

One of the most widely used phase change models is the Lee model [60]. The Lee phase change model is used in this simulation to calculate the amount of vapor produced in the evaporator. Its expression is presented in Equation 6.2.

$$\frac{\partial m_{g,e}}{\partial t} = \beta_e \alpha_l \rho_l \frac{T_{w,e} - T_{sat}}{T_{sat}} \quad (6.2)$$

With $m_{g,e}$ the amount of vapor mass above the evaporator (kg). β_e is the so called volumetric mass transfer intensity factor for evaporation (m^3/s). This factor is influenced by many physical and numerical variables [61]. Finding right empirical relations for the mass transfer intensity factor is essential for the reliability of the model. For this model β_e is approximated based on the experimental results. Normally β_e is the mass transfer intensity factor and has the dimension of s^{-1} . Since in this case the value will be determined from experiments, it was chosen to include the volume in the variable β_e so the mass vapor mass transport can directly be calculated using Equation 6.2. α_l is the volume fraction of liquid ($-$) for these simulations this value is assumed to be 1.

The liquid water temperature in the evaporator ($T_{w,e}$) is calculated using the energy balance, which is presented in Equation 6.3.

$$m_{w,e} c_{p,l} \frac{\partial T_{w,e}}{\partial t} = P_{in} - \frac{\partial m_{g,e}}{\partial t} \Delta H \quad (6.3)$$

With P_{in} the power supplied to the water by the heat exchanger (W). In this model the experiment data is interpolated to construct a time dependent P_{in} , ΔH is the heat of vaporization (J/kg).

The pressure development is based on Joule expansion, also called free expansion. A valve is opened between two containers with constant volumes but different pressures. When the valve opens the system will strive to achieve an equilibrium pressure [62]. The expression for the equilibrium pressure as a function of time is given in Equation 6.4.

$$p_{eq}(t) = \frac{V_{g,eva}p_e(t) + V_{g,con}p_c(t)}{V_{g,eva} + V_{g,con}} \quad (6.4)$$

With $V_{g,eva}$ and $V_{g,con}$ being the volumes occupied by the gas phase in respectively the evaporator and the condenser (m^3).

The modeled system is more complex than free expansion, because in every time step new vapor is produced in the evaporator and consumed in the condenser. The produced vapor temperature is cooling down in time. This causes a gradual development of the initial condition to the equilibrium pressure. A new time scale, called the relaxation time (τ), is introduced to better describe the decrease in pressure from the initial value to the eventual equilibrium pressure. In Equation 6.5 the relation which describes the pressure development from the moment the valve opens to the end of the simulation is presented.

$$p_e(t) = p_{eq}(t) + (p_e(t_{valve}) - p_{eq}(t_{valve}) - \Delta p_{steady}) \exp\left(-\frac{t - t_{valve}}{\tau}\right) + \Delta p_{steady} \quad (6.5)$$

With t_{valve} the point in time when the valve opens (s), τ the relaxation time characterising the time needed to reach a steady pressure (s). This is at 60s in all these simulations. Δp_{steady} is the pressure difference between the vapor evaporator and condenser due to the pressure drop over the valve (Pa).

The evaporator vapor temperature can be found by interpolating the calculated pressure with the steam table data. It is assumed that the vapor phase is always fully saturated. The amount of mass in the vapor phase can be calculated using the ideal gas law, which is given in Equation 6.6.

$$pV = mR_w T \quad (6.6)$$

With R_w the specific gas constant of water (J/kgK).

The specific enthalpy of each quantity of vapor can be calculated using Equation 6.7. By multiplying the specific enthalpy by the corresponding mass, the total enthalpy can be calculated. Figure 6.3 shows a schematic enthalpy plot, which is used to clarify the computation of an additional energy term which is needed to close the energy balance according to the laws of thermodynamics.

$$h_g = c_{p,g} T \quad (6.7)$$

With h_g the specific enthalpy of the vapor (J/kg)

The starting point in Figure 6.3 is at t . Here the total enthalpy is the specific enthalpy of the condenser vapor times the condenser vapor mass. Then the quantity of vapor mass from above the evaporator flows into the condenser vapor, because the pressure is lower in the condenser. The temperature of the inflowing evaporator vapor is higher than the condenser vapor temperature. The total enthalpy of the system if no vapor would be condensed is given at $t_{intermediate}$. Due to the inflow of vapor the total vapor mass has increased to m_{mix} . The temperature at $t_{intermediate}$, T_{mix} is the mass averaged temperature of the initial vapor and the inflowing vapor. In $t + \Delta t$ an amount of the vapor is condensed. This reduces the amount of enthalpy of the vapor phase above the condenser. But the enthalpy at t will always lower than at $t + \Delta t$ because T_{mix} is larger than $T_{g,c}$. The overdimensioned condenser assumption imposes that the condenser vapor

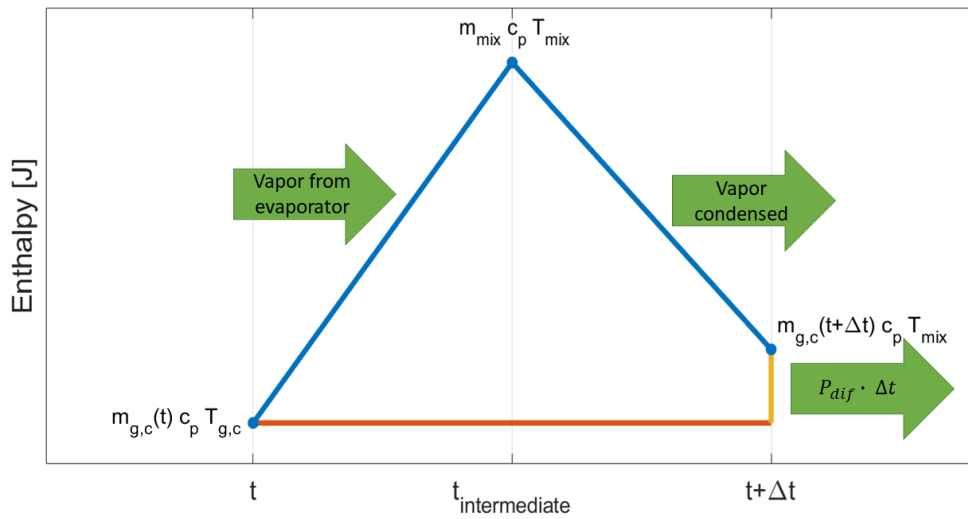


Figure 6.3: Schematic enthalpy diagram of the condenser vapor phase during one numerical time step, assuming that $m_{g,c}(t) = m_{g,c}(t + \Delta t)$ for simplicity

temperature remains constant. According to the laws of thermodynamics an additional energy flux is needed to bring down the temperature in $t + \Delta t$ to the temperature in t . This energy flux is called P_{dif} in this model. The analytical expression is given in Equation 6.8. This vapor cooling power P_{dif} comes from the condenser. Because Figure 6.3 shows the enthalpy per time step, the amount of energy that needs to be subtracted to close the energy balance is P_{dif} times Δt . To keep Figure 6.3 simple it was chosen that $m_{g,c}(t) = m_{g,c}(t + \Delta t)$ but this does not have to be so.

$$P_{dif} = m_{g,c} c_{p,g} \frac{\partial T_{g,c}}{\partial t} \quad (6.8)$$

The energy which is dissipated by the condenser can now be calculated using the energy balance for the condenser Equation 6.9.

$$P_{out} = P_{dif} + \frac{\partial m_{g,c}}{\partial t} \Delta H \quad (6.9)$$

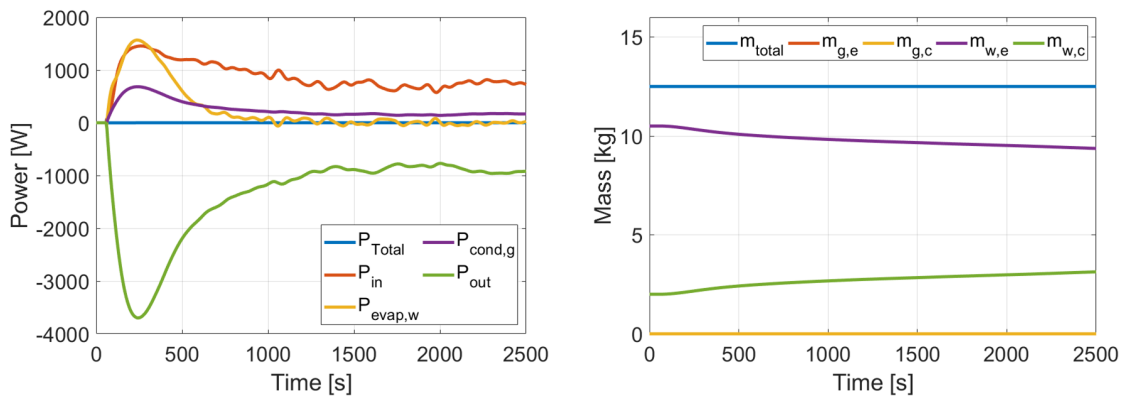
This model contains three parameters which need to be approximated. These parameters are: the volumetric mass transfer intensity factor β_e , the relaxation time τ and the steady state pressure difference Δp_{steady} . For this particular analytical model the values of these parameters are: $\beta_e = 9.0 \cdot 10^{-5} m^3/s$, $\tau = 150s$ and $\Delta p_{steady} = 0.5 mbar$. Appendix E contains details on how the values of these parameters were found. The appendix also contains figures which show how changing these parameters influences the computational results.

6.3 Numerical results validation

To obtain reliable results it is important to determine whether the model represents the system accurately, therefore validation is important. The model itself must be physically correct, meaning that total mass and total energy within the system is conserved. In addition the model results should agree with the measurements obtained in the experiments.

6.3.1 Energy and mass conservation

In Figure 6.4 the plots that demonstrate the conservation of energy and mass are presented. Figure 6.4 (a) shows the computed powers in time: in blue the sum of all powers, in red the heat exchanger power, in yellow the power due to the cooling of the water in the evaporator, in purple the power due to the cooling of the vapor above the condenser (calculated by Equation 6.8) and in green the power outputted at the condenser.



(a) The numerical computed powers as a function. In blue the sum of all powers, in red the input power, in yellow the power due to the water cooling and in purple the outputted power.

(b) The numerical computed masses as a function. In blue the sum of all masses, in yellow and purple the mass of the liquid in respectively the evaporator and the condenser, in green and red the mass of vapor above respectively the evaporator and the condenser.

Figure 6.4: Numerical conservation plots: on the left the power as a function of time on the right the masses as a function of time. The blue lines in both figures is the sum of all components.

It can be seen in Figure 6.4 (a) that the sum of all powers (the blue line) is zero for every time step. This means that in every time step energy is conserved. It can be seen that the power due to the water cooling (yellow) peaks when the valve opens, but after some time the value goes to zero. This is exactly the behaviour observed in the experiments. Similar to the water cooling the vapor cooling above the condenser (purple) also peaks when the valve has just opened. This is logical because when the valve has just opened a relative large amount of steam is transported and it has a high temperature. In contrast with the yellow line the purple line does not go to zero. This is because a temperature difference keeps existing between the evaporator and condenser vapor in this model. In reality this temperature difference will be close to zero, but due to the overdimensioned condenser assumption, the vapor will need to be cooled during the whole simulation. The powers due to the temperature differences of the vapor phases themselves are not included since they are negligibly small.

Figure 6.4 (b) shows the computed masses in time. In blue the sum of all masses in the system can be seen. The purple line gives the mass of liquid in the evaporator and the green line the mass of liquid in the condenser. The mass of vapor above the evaporator is in red and the mass of vapor above the condenser is in yellow.

In Figure 6.4 (b) the total mass of the system (blue) is a constant value throughout the simulation, which means a conservation of mass. As expected the mass of liquid in the evaporator (the purple line) decreases in time due to the evaporation. The mass of liquid in the condenser (the green line) increases in time due to the condensation. The mass of vapor above the evaporator (the red line) and above the condenser (the yellow line) are so small, that they can barely be seen in Figure 6.4 (b). The maximum mass in the vapor phase during the simulation was 0.48g compared to 12.5kg in the liquid phase.

6.3.2 Validation with experimental data

Figure 6.5 shows the power which is outputted at the condenser in time. The figure includes the experimentally obtained value in red and the numerical computation in blue.

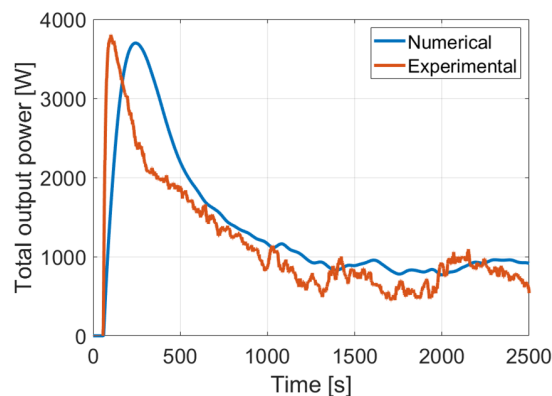
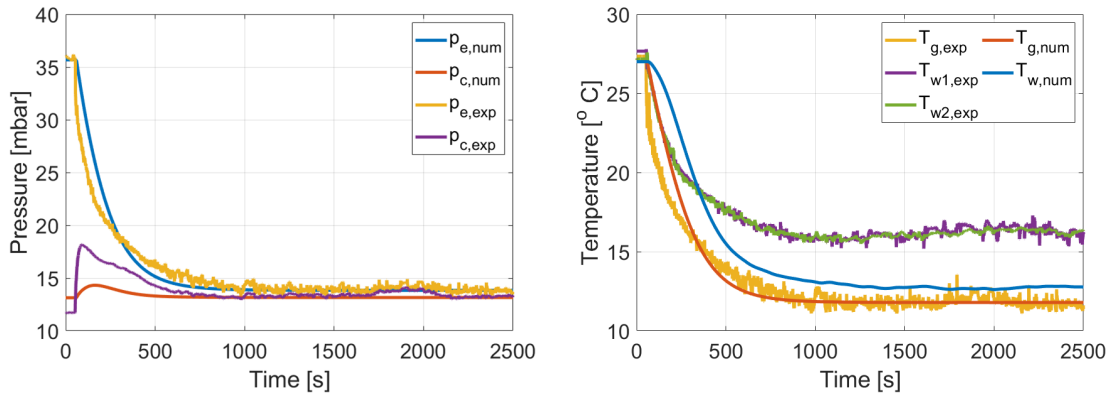


Figure 6.5: The total power output which is outputted at the condenser as a function of time. In blue the numerical computation and in red the experiment result.

It can be seen in Figure 6.5 that the lines fit nicely. Logically the experimental results contain much more fluctuations. The numerical result reacts slower to the opening of the valve. This can be seen by the lower slope of the curve when the valve opens and a maximum later in time. The numerical model slightly overpredicts the output power, but the overall behaviour is similar.

The validation plots for the numerically computed pressures and temperatures are presented in Figure 6.6.



(a) The pressures in the system: the numerical computed evaporator pressure (blue) and condenser pressure (red) and the measured evaporator pressure (yellow) and condenser pressure (purple).

(b) The temperatures in the evaporator: the numerical computed vapor temperature (red) and water temperature (blue) and the measured vapor temperature (yellow) and water temperature (purple and green).

Figure 6.6: Numerical validation plots: on the left the calculated against the measured pressures and on the right the calculated against the measured temperatures.

Figure 6.6 (a) presents the pressures in the system. The figure contains the numerical solution and the experimental results. The numerical computation of the evaporator pressure is in blue and the numerical computation of the condenser is in red. The pressure measurements of the evaporator and condenser pressure are respectively in yellow and purple. A few things can be observed in Figure 6.6 (a). It can be seen that the peak in condenser pressure is much lower for the numerical calculation. This is because of the overdimensioned condenser assumption. In every numerical time step the vapor enthalpy above the condenser is cooled by the water temperature, which is kept constant by the overdimensioned heat exchanger. In reality the condenser water will heat up, allowing for a much larger vapor pressures above the condenser. The numerical evaporator pressure has a slightly different course in the transient part compared to the experimental result, but on average the calculation matches the measurement. The evaporator pressure is one of the boundary condition inputs for the existing numerical reactor model.

Figure 6.6 (b) presents the temperatures in the evaporator in time. The figure contains the thermocouple measurements. The measured vapor temperature is in yellow. The green and purple lines are the measured liquid temperatures at two different heights in the bath. The red line is the vapor temperature as computed by the numerical model. The blue line is the liquid temperature as calculated by the numerical model. The most prominent observation in Figure 6.6 (b) is the underprediction of the liquid temperature by the numerical model. It can be concluded that the numerical model can not be used for predicting the liquid temperature. The liquid is modeled as one lumped mass, to which heat is supplied and withdrawn every time step. This is a very rough approximation, since there can be internal temperature gradients, convection currents and heat exchange with the steel vessel. The numerical computation of the vapor temperature matches the experimental observations nicely, with the exception of a small time period at the start of the experiment, when the valve has just opened. It can be concluded that the vapor temperature can be modeled using this numerical computation. This vapor temperature is one of the boundary condition inputs for the existing numerical reactor model.

6.4 Influence of boundary condition

Figure 6.7 shows the three parameters which need to be prescribed on the water vapor inlet boundary condition of the existing model (boundary 1 in Figure 6.1): the vapor pressure, vapor temperature and vapor concentration as a function of time.

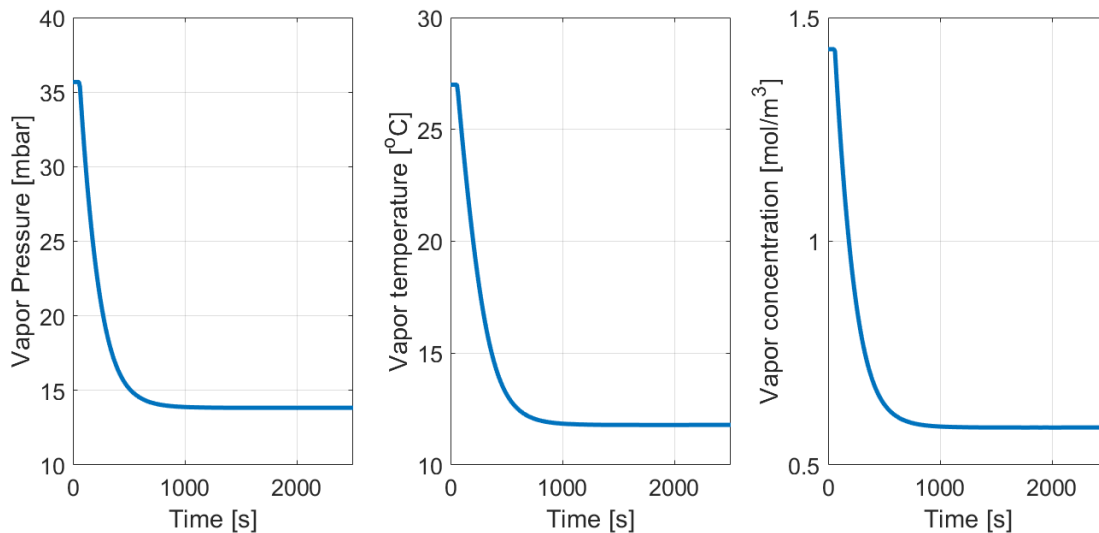


Figure 6.7: Numerical calculation of the water vapor inlet boundary condition values for respectively the vapor pressure, vapor temperature and vapor concentration in time. These relations are for an evaporator connected to a condenser. The response will be different when the evaporator is connected to a reactor.

The parameters in Figure 6.7 all have a similar development in time. The resemblance between the pressure and temperature curve is logical, since the saturation line of water almost has a constant slope for vapor pressures between 10 and 35 mbar. The similar shape for the concentration curve is also logical since the concentration is calculated with the ideal gas law. As seen in Equation 6.1 the concentration is only a function of the temperature and pressure. The influence of the pressure on the concentration is much larger, than the influence of the temperature, because the temperature in Kelvin barely changes. A 5% decrease in temperature is observed during the course of the simulation. Whereas the pressure decreases with 61%.

A remark needs to be made. The time dependent parameters of Figure 6.7 would be the water vapor inlet boundary conditions only if the reactor would behave the same as the condenser. This is certainly incorrect. The reactor would be at a much lower pressure when the valve is closed. So one can imagine that the eventually equilibrium pressure lies much lower. It is also expected that the relaxation time would be much higher, since the reaction kinetics of the absorbent would be much slower than condensation on a cold surface.

7.1 Conclusions

The goals of this thesis were: to capture new insights in the phenomena taking place during subatmospheric evaporation in a TCS system framework, establish a relation on how hydrostatic pressure influences subatmospheric evaporation in a TCS system framework and research methods to reduce the negative effect caused by the hydrostatic pressure for TCS.

An experimental setup was created to observe and measure subatmospheric evaporation behaviour for different water heights. The evaporator is connect to a condenser instead of a reactor for controllability and a reduction of the complexity of the system. The side of the evaporator vessel is covered by a transparent cover which makes it possible to see the evaporator water and the heat exchanger. Multiple experiments were done with two different heat exchangers. The starting conditions were the same except for the varying water height.

During all experiments it became apparent that two distinct evaporation regimes could be distinguished. When the valve opens the transient regime starts. The pressure decrease above the evaporator causes a violent boiling process in which sensible heat of the water is dissipated via boiling on the water surface. In this regime the power subtracted by the condenser is greater than the power supplied to the evaporator. After some time a new equilibrium pressure is reached: the pressures and temperatures are relatively constant and the evaporator and condenser power are equal. It was decided to split up the data and study the effect of hydrostatic pressure on both regimes.

In the transient phase the power increases with increasing water height, because more sensible heat is stored in the larger quantity of water. A maximum for the power due to the cooling of the water was observed at a near constant pressure difference between evaporator and condenser. The location of the peak was not influenced by the amount of water. The same is true for the transient heat exchanger power: The value of the maximum increases with increasing water height and the maximum occurs at the same pressure difference. In the steady regime the average heat exchanger power increases with increasing water height. The heat flux decreases rapidly with increasing water height, to a more or less constant value. Only a small section of the water, just below the surface, contributes to nucleate pool boiling. Increasing the water height results in relative more water experiencing convection pool boiling, thus lowering the average heat flux of the heat exchanger. It was also observed that changing the flow direction of the heat exchanger, and thereby increasing the wall temperature at the bottom of the heat exchanger, did not influence the boiling behaviour. In the steady regime nucleate pool boiling was observed in all experiments 2.2cm below the water surface. In none of the experiments nucleate pool boiling was observed anywhere deeper than 5.8cm below the water surface.

Increasing the surface area of the heat exchanger does not result in bubble formation deeper in the bath, instead the overall bath temperature increases. With a factor 4.4 larger surface area the produced power more than doubled ($1.9kW$ instead of $0.8kW$). The effective heat flux for larger heat exchanger is far lower compared to the small heat exchanger. The larger surface area contributed more to the convection pool boiling than to the nucleate pool boiling resulting in an on average lower heat exchange per surface area.

An analytical model was built to better describe the evaporator behaviour for an already existing numerical reactor model. The model is based on the Lee phase change model and free expansion, it outputs time dependent boundary conditions for an existing numerical reactor model. The analytical model does a reasonable job for modeling the output power, evaporator pressure and evaporator vapor temperature, but fails to accurately model the condenser pressure and evaporator liquid temperature.

7.2 Recommendations

A method of enhancing the boiling performance is changing the heat exchanger properties. It is possible to coat the heat exchanger in such a way that new nucleation sites will be formed on the surface. In the future, experiments could be done to see if changing the heat exchanger surface properties could reduce the decreased effectiveness due to the hydrostatic pressure and allow nucleate pool boiling deeper in the water bath. Another concept which could be experimentally investigated is a heating element floating on the water surface. This way, the heat exchanging surface is only in the low hydrostatic pressure part during the whole experiment. This would make subatmospheric boiling process much more effective since the amount of heat exchanger which is obliged to take part in convection pool boiling could be minimized.

The experimental work could have been extended with the performance of the heat exchanger as a condenser. The eventual heat exchanger for the TCS system should function both as a condenser and an evaporator. It must be kept in mind that the evaporator must be enhanced, but not at the expense of the condenser performance. It was chosen to leave condensation out the scope of this thesis because hydrostatic pressure is only a problem occurring during subatmospheric evaporation.

In future experimental research on hydrostatic pressures it is recommended to use a digital water height measurement device, like a time domain reflectometer or a level pressure sensor. Measuring the water height by hand turned out to be very labor intensive and has bad accuracy and sample time. A 3D laser scan of the heat exchangers could be made. This would make it possible to calculate the effective heat flux accurately even for complex shapes. A way to measure the heat exchanger surface temperature, could potentially result in much more insight in the driving forces behind the phenomena occurring during an experiment. The problem is that measuring the surface temperature will effect the boiling phenomena themselves, making the measurements unrealistic for a normal heat exchanger.

Bibliography

- [1] A. Dai, *Drought under global warming: A review*, Jan. 2011. DOI: 10.1002/wcc.81. [Online]. Available: <https://onlinelibrary.wiley.com/doi/full/10.1002/wcc.81> <https://onlinelibrary.wiley.com/doi/abs/10.1002/wcc.81> (see page 1).
- [2] K. Zhang, B. C. Douglas, and S. P. Leatherman, **Global warming and coastal erosion**, *Climatic Change*, vol. 64: no. 1-2, 41–58, ISSN: 01650009. DOI: 10.1023/B:CLIM.0000024690.32682.48. [Online]. Available: www.ipcc.ch (see page 1).
- [3] C. Rosenzweig and M. L. Parry, **Potential impact of climate change on world food supply**, *Nature*, vol. 367, 133–138 (see page 1).
- [4] M. K. van Aalst, **The impacts of climate change on the risk of natural disasters**, *Disasters*, vol. 30: no. 1, 5–18, ISSN: 03613666. DOI: 10.1111/j.1467-9523.2006.00303.x (see page 1).
- [5] J. Cook, D. Nuccitelli, S. A. Green, M. Richardson, B. Winkler, R. Painting, R. Way, P. Jacobs, and A. Skuce, **Quantifying the consensus on anthropogenic global warming in the scientific literature**, *Environmental Research Letters*, vol. 8: no. 2, ISSN: 17489326. DOI: 10.1088/1748-9326/8/2/024024 (see page 1).
- [6] Rijksoverheid, *Energieverbruik door huishoudens, 1990-2016 | Compendium voor de Leefomgeving*, 2018. [Online]. Available: <https://www.clo.nl/indicatoren/nl0035-energieverbruik-door-de-huishoudens> (see page 1).
- [7] C. J. Ferchaud, H. A. Zondag, A. Rubino, and R. De Boer, **Seasonal sorption heat storage – Research on thermochemical materials and storage performance**, *Proceedings of Heat Power Cycle 2012*: no. September, 1–7. [Online]. Available: <https://pure.tue.nl/ws/files/3821108/572851890456641.pdf> (see page 1).
- [8] C. J. Ferchaud, **Experimental study of salt hydrates for thermochemical seasonal heat storage**, PhD thesis, Technische Universiteit Eindhoven, 2016 (see page 2).
- [9] A. Palacios, M. Elena Navarro, C. Barreneche, and Y. Ding, **Hybrid 3 in 1 thermal energy storage system – Outlook for a novel storage strategy**, *Applied Energy*, vol. 274: no. December 2019, 115024, ISSN: 03062619. DOI: 10.1016/j.apenergy.2020.115024. [Online]. Available: <https://doi.org/10.1016/j.apenergy.2020.115024> (see pages 2, 7).
- [10] S. Michaie, R. Rullière, and J. Bonjour, **Experimental study of bubble dynamics of isolated bubbles in water pool boiling at subatmospheric pressures**, *Experimental Thermal and Fluid Science*, vol. 87, 117–128, ISSN: 08941777. DOI: 10.1016/j.expthermflusci.2017.04.030 (see page 2).
- [11] K. Wojtasik, R. Rullière, Z. Krolicki, B. Zajackowski, and J. Bonjour, **Subcooled boiling regime map for water at low saturation temperature and subatmospheric pressure**, *Experimental Thermal and Fluid Science*, vol. 118: no. April, 110150, ISSN: 08941777. DOI: 10.1016/j.expthermflusci.2020.110150. [Online]. Available: <https://doi.org/10.1016/j.expthermflusci.2020.110150> (see pages 2, 20, 21).
- [12] J. G. Calvert, **Glossary of atmospheric chemistry terms**, *Pure and Applied Chemistry*, vol. 62: no. 11, 2167–2219, ISSN: 13653075. DOI: 10.1351/pac199062112167 (see page 5).
- [13] N. C. Srivastava and I. W. Eames, **A review of adsorbents and adsorbates in solid-vapour adsorption heat pump systems**, *Applied Thermal Engineering*, vol. 18: no. 9-10, 707–714, ISSN: 13594311. DOI: 10.1016/S1359-4311(97)00106-3 (see page 5).
- [14] L. Scapino, **Sorption thermal energy storage for smart grids - A system-scale analysis**, *Thesis*: no. 2019, 255. DOI: 10.13140/RG.2.2.15498.00964. [Online]. Available: https://pure.tue.nl/ws/portalfiles/portal/136194901/20191025_Scapino.pdf (see page 5).

- [15] R. Pasto and W. Docekal, **Chemistry Reference Tables Workbook**. Topical Review Book Company, 2011 (see page 6).
- [16] H. A. Zondag, **Sorption Heat Storage**. Elsevier Ltd., 2015, 135–154, ISBN: 9780124095403. DOI: [10.1016/B978-0-12-409540-3.00006-2](https://doi.org/10.1016/B978-0-12-409540-3.00006-2). [Online]. Available: <http://dx.doi.org/10.1016/B978-0-12-409540-3.00006-2> (see page 7).
- [17] F. Jeremias, D. Fröhlich, C. Janiak, and S. K. Henninger, **Water and methanol adsorption on MOFs for cycling heat transformation processes**, *New Journal of Chemistry*, vol. 38:no. 5, 1846–1852, ISSN: 13699261. DOI: [10.1039/c3nj01556d](https://doi.org/10.1039/c3nj01556d). [Online]. Available: www.rsc.org/njc (see page 7).
- [18] T.-T. Nguyen, V. Martin, A. Malmquist, and C. A. Silva, **A review on technology maturity of small scale energy storage technologies**, *Renewable Energy and Environmental Sustainability*, vol. 2, 36, ISSN: 2493-9439. DOI: [10.1051/rees/2017039](https://doi.org/10.1051/rees/2017039) (see page 8).
- [19] A. H. Abedin, **Chapter 17 - Thermochemical energy storage systems: Modelling, analysis and design**, July. Elsevier Inc., 2010, vol. M. Sc, 146, ISBN: 9780128034408. DOI: [10.1016/B978-0-12-803440-8/00017-8](https://doi.org/10.1016/B978-0-12-803440-8/00017-8). [Online]. Available: https://ir.library.queensu.ca/bitstream/10155/119/1/Haji%20Abedin_Ali.pdf (see page 8).
- [20] A. J. De Jong, L. Van Vliet, C. Hoegaerts, M. Roelands, and R. Cuypers, **Thermochemical Heat Storage - From Reaction Storage Density to System Storage Density**, *Energy Procedia*, vol. 91:no. 0, 128–137, ISSN: 18766102. DOI: [10.1016/j.egypro.2016.06.187](https://doi.org/10.1016/j.egypro.2016.06.187). [Online]. Available: <http://dx.doi.org/10.1016/j.egypro.2016.06.187> (see page 8).
- [21] K. Iammak, W. Wongsuwan, and T. Kiatsiriroj, **Investigation of Modular Chemical Energy Storage Performance**, *Proceedings of the Joint International Conference on Energy and Environment*, vol. 022:no. December, 504–507 (see page 9).
- [22] T. Yan, Z. H. Kuai, and S. F. Wu, **Experimental investigation on a MnCl₂-SrCl₂/NH₃ thermochemical resorption heat storage system**, *Renewable Energy*, vol. 147, 874–883, ISSN: 18790682. DOI: [10.1016/j.renene.2019.09.033](https://doi.org/10.1016/j.renene.2019.09.033) (see page 9).
- [23] N. Oldridge, *Phase Diagrams - ChemistNate*. [Online]. Available: <https://www.chemistnate.com/phase-diagrams.html> (see page 10).
- [24] S. R. Turns, “Thermodynamic Properties, Property relationships, and Processes,” in *Thermodynamics: Concepts and Applications*, Cambridge University Press, 2006, ch. Chapter 2, 88–264 (see page 11).
- [25] J. J. Zhao, Y. Y. Duan, X. D. Wang, and B. X. Wang, **Effects of superheat and temperature-dependent thermophysical properties on evaporating thin liquid films in microchannels**, *International Journal of Heat and Mass Transfer*, vol. 54:no. 5-6, 1259–1267, ISSN: 00179310. DOI: [10.1016/j.ijheatmasstransfer.2010.10.026](https://doi.org/10.1016/j.ijheatmasstransfer.2010.10.026). [Online]. Available: <http://dx.doi.org/10.1016/j.ijheatmasstransfer.2010.10.026> (see page 11).
- [26] K. Stephan, **Heat Transfer in Condensation and Boiling**, ser. International Series in Heat and Mass Transfer. Berlin, Heidelberg: Springer Berlin Heidelberg, 1992, ISBN: 978-3-642-52459-2. DOI: [10.1007/978-3-642-52457-8](https://doi.org/10.1007/978-3-642-52457-8). [Online]. Available: <http://link.springer.com/10.1007/978-3-642-52457-8> (see page 12).
- [27] P. D. Dunn and D. A. Reay, **Heat Pipes**, Third Edit. Pergamon Press, 1982, ISBN: 0-08-029355-7 (see page 12).
- [28] G. Bruno, N. Burgio, M. Corcione, L. Cretara, M. Frullini, W. Fulgione, L. Manara, A. Quintino, A. Santagata, and L. Zanotti, **On the critical energy required for homogeneous nucleation in bubble chambers employed in dark matter searches**, *European Physical Journal C*, vol. 79:no. 3, ISSN: 14346052. DOI: [10.1140/epjc/s10052-019-6689-4](https://doi.org/10.1140/epjc/s10052-019-6689-4) (see page 12).
- [29] D. Heinze, **Physically-Based Models for Two-Phase Flow Phenomena in Steam Injectors A One-Dimensional Simulation Approach**, October 2015. 2015, 72, ISBN: 9783731504276. DOI: [10.5445/KSP/1000048586](https://doi.org/10.5445/KSP/1000048586) (see page 13).

- [30] D. B. R. Kenning, "POOL BOILING," in *A-to-Z Guide to Thermodynamics, Heat and Mass Transfer, and Fluids Engineering*, Begellhouse. DOI: 10.1615/AtoZ.p.pool{_}boiling. [Online]. Available: <http://www.thermopedia.com/content/1046/> (see page 13).
- [31] S. Nukiyama, **The maximum and minimum values of the heat Q transmitted from metal to boiling water under atmospheric pressure**, *International Journal of Heat and Mass Transfer*, vol. 9:no. 12, 1419–1433, ISSN: 00179310. DOI: 10.1016/0017-9310(66)90138-4 (see page 13).
- [32] *Thermal-FluidsPedia | Pool Boiling Regimes | Thermal-Fluids Central*. [Online]. Available: https://www.thermalfluidscentral.org/encyclopedia/index.php/Pool_Boiling_Regimes (see page 14).
- [33] A. Mehralzadeh, S. Reza Shabani, and G. Bakeri, *Effect of modified surfaces on bubble dynamics and pool boiling heat transfer enhancement: A review*, Mar. 2020. DOI: 10.1016/j.tsep.2019.100451 (see page 15).
- [34] T. G. Theofanous, J. P. Tu, A. T. Dinh, and T. N. Dinh, **The boiling crisis phenomenon part I: Nucleation and nucleate boiling heat transfer**, *Experimental Thermal and Fluid Science*, vol. 26:no. 6-7, 775–792, ISSN: 08941777. DOI: 10.1016/S0894-1777(02)00192-9 (see page 14).
- [35] B. Zajackowski, T. Halon, and Z. Krolicki, **Experimental verification of heat transfer coefficient for nucleate boiling at sub-atmospheric pressure and small heat fluxes**, *Heat and Mass Transfer/Waerme- und Stoffuebertragung*, vol. 52:no. 2, 205–215, ISSN: 14321181. DOI: 10.1007/s00231-015-1549-8. [Online]. Available: <http://dx.doi.org/10.1007/s00231-015-1549-8> (see page 15).
- [36] S. Michaie, R. Rullière, and J. Bonjour, **Experimental study of bubble dynamics of isolated bubbles in water pool boiling at subatmospheric pressures**, *Experimental Thermal and Fluid Science*, vol. 87, 117–128, ISSN: 08941777. DOI: 10.1016/j.expthermflusci.2017.04.030. [Online]. Available: <http://dx.doi.org/10.1016/j.expthermflusci.2017.04.030> (see page 15).
- [37] F. Giraud, R. Rullière, C. Toubanc, M. Clausse, and J. Bonjour, **Experimental evidence of a new regime for boiling of water at subatmospheric pressure**, *Experimental Thermal and Fluid Science*, vol. 60, 45–53, ISSN: 08941777. DOI: 10.1016/j.expthermflusci.2014.07.011. [Online]. Available: <http://dx.doi.org/10.1016/j.expthermflusci.2014.07.011> (see pages 16, 17).
- [38] J. S. Saini, C. P. Gupta, and S. Lal, **Effect of jakob number on forces controlling bubble departure in nucleate pool boiling**, *International Journal of Heat and Mass Transfer*, vol. 18:no. 3, 472–474, ISSN: 00179310. DOI: 10.1016/0017-9310(75)90035-6 (see page 17).
- [39] S. J. van Stralen, R. Cole, W. M. Sluyter, and M. S. Sohal, **Bubble growth rates in nucleate boiling of water at subatmospheric pressures**, *International Journal of Heat and Mass Transfer*, vol. 18:no. 5, 655–669, ISSN: 00179310. DOI: 10.1016/0017-9310(75)90277-X (see page 17).
- [40] J. Karl, **Spontaneous condensation in boundary layers**, *Warme- und Stoffuebertragung Zeitschrift*, vol. 36:no. 1, 37–44, ISSN: 00429929. DOI: 10.1007/s002310050361. [Online]. Available: <https://link.springer.com/article/10.1007/s002310050361> (see page 17).
- [41] J. W. Rose, "Film and dropwise condensation," in *Handbook of Thermal Science and Engineering*, Springer International Publishing, Jul. 2018, 2031–2074, ISBN: 9783319266954. DOI: 10.1007/978-3-319-26695-4{_}50. [Online]. Available: https://doi.org/10.1007/978-3-319-26695-4_50 (see page 17).
- [42] A. Leipertz, "Dropwise Condensation," in *VDI Heat Atlas*, Erlangen, 2010, ch. J3, 933–938, ISBN: 9783540778776. DOI: 10.1007/978-3-540-77877-6 (see pages 17, 18).
- [43] W. Kast, **Wärmeübertragung bei Tropfenkondensation**, *Chemie Ingenieur Technik*, vol. 35:no. 3, 163–168, ISSN: 15222640. DOI: 10.1002/cite.330350308. [Online]. Available: <http://doi.wiley.com/10.1002/cite.330350308> (see page 18).
- [44] E. Spooner, *What is Surface Energy? Calculation Models and More Explained | Ossila*. [Online]. Available: <https://www.ossila.com/pages/a-guide-to-surface-energy> (see page 18).
- [45] G. Koch, D. C. Zhang, A. Leipertz, M. Grischke, K. Trojan, and H. Dimigen, **Study on plasma enhanced CVD coated material to promote dropwise condensation of steam**, *International Journal of Heat and Mass Transfer*, vol. 41:no. 13, 1899–1906, ISSN: 00179310. DOI: 10.1016/S0017-9310(97)00356-6 (see page 18).

- [46] R. Wen, Z. Lan, B. Peng, W. Xu, and X. Ma, **Droplet dynamics and heat transfer for dropwise condensation at lower and ultra-lower pressure**, *Applied Thermal Engineering*, vol. 88, 265–273, ISSN: 13594311. DOI: 10.1016/j.applthermaleng.2014.09.069 (see page 18).
- [47] R. W. Bonner, **Correlation for dropwise condensation heat transfer: Water, organic fluids, and inclination**, *International Journal of Heat and Mass Transfer*, vol. 61: no. 1, 245–253, ISSN: 00179310. DOI: 10.1016/j.ijheatmasstransfer.2012.12.045 (see page 18).
- [48] S. H. Hoenig, S. Modak, Z. Chen, M. Kaviany, J. F. Gilchrist, and R. W. Bonner, **Role of substrate thermal conductivity and vapor pressure in dropwise condensation**, *Applied Thermal Engineering*, vol. 178, 115529, ISSN: 13594311. DOI: 10.1016/j.applthermaleng.2020.115529 (see page 18).
- [49] S. Ren and W. Zhou, **Numerical investigation of nucleate pool boiling outside a vertical tube under sub-atmospheric pressures**, *International Communications in Heat and Mass Transfer*, vol. 116, 104662, ISSN: 07351933. DOI: 10.1016/j.icheatmasstransfer.2020.104662 (see page 19).
- [50] L. Schnabel, C. Scherr, and C. Weber, **Water As Refrigerant – Experimental Evaluation of Boiling Characteristics At Low Temperatures and Pressures**, *VII Minsk International Seminar “Heat Pipes, Heat Pumps, Refrigerators, Power Sources”*: no. January, 322–330 (see page 19).
- [51] ERIKS, **Genuine Viton® 75-compound 51414 black - Technical Data Sheet**. [Online]. Available: o-ring.info/en/datasheets%20o-ring/viton-fkm/eriks%20-%20datasheet%20-%20genuine%20viton%2075-compound%2051414%20black.pdf (see page 26).
- [52] “Reference Section,” in *The New Labfacility Temperature Handbook*, 2006, ch. 9, 139. [Online]. Available: <https://www.labfacility.com/pub/media/pdf/temperature-handbook-9-to-13.pdf> (see page 29).
- [53] Kobold, **Operating Instructions for Ultrasonic Flowmeter / -Monitor / -Counter / -Dosing Unit Model : DUK**. [Online]. Available: <https://koboldusa.com/media/flow/DUK/manual-ultrasonic-flowmeter-compact-duk.pdf> (see page 29).
- [54] Leybold, **Vacuum Transducer DI200 DI201 DU200 DU201**, 1–16. [Online]. Available: https://www.leyboldproducts.us/media/pdf/b9/15/92/300360487_002_C0_DI_DU_200_201_EN.pdf (see page 29).
- [55] *bol.com | Stalen 50 cm liniaal met gegraveerde maatverdeling*. [Online]. Available: <https://www.bol.com/nl/p/stalen-50-cm-liniaal-met-gegraveerde-maatverdeling/9200000035522496/> (see page 29).
- [56] S. Papavinasam, “Measurements,” in *Corrosion Control in the Oil and Gas Industry*, Elsevier, Jan. 2014, 751–800. DOI: 10.1016/B978-0-12-397022-0.00012-1. [Online]. Available: <https://linkinghub.elsevier.com/retrieve/pii/B9780123970220000121> (see page 30).
- [57] W. Wagner, J. R. Cooper, A. Dittmann, J. Kijima, H. J. Kretzschmar, A. Kruse, R. Mareš, K. Oguchi, H. Sato, I. Stöcker, O. Šifner, Y. Takaishi, I. Tanishita, J. Trübenbach, and T. Willkommen, **The IAPWS industrial formulation 1997 for the thermodynamic properties of water and steam**, *Journal of Engineering for Gas Turbines and Power*, vol. 122: no. 1, 150–180, ISSN: 07424795. DOI: 10.1115/1.483186 (see page 32).
- [58] *Statistical data treatment*. [Online]. Available: <http://ion.chem.usu.edu/~sbialkow/Classes/160/Lab3/chem160-3.html> (see page 33).
- [59] K. Kant, **TKI Project (SWeKOS): Numerical heat transfer analysis of a thermochemical Energy Pad**, Tech. Rep., 2019, 60 (see page 51).
- [60] D. Sun, J. Xu, and Q. Chen, **Modeling of the evaporation and condensation phase-change problems with FLUENT**, *Numerical Heat Transfer, Part B: Fundamentals*, vol. 66: no. 4, 326–342, ISSN: 15210626. DOI: 10.1080/10407790.2014.915681 (see page 53).
- [61] J. Wang, Y. Li, L. Wang, S. Xia, J. Ren, H. Mao, and Y. Xu, **Numerical investigation on subcooled pool film boiling of liquid hydrogen in different gravities**, *International Journal of Hydrogen Energy*, vol. 46: no. 2, 2646–2657, ISSN: 03603199. DOI: 10.1016/j.ijhydene.2020.10.079. [Online]. Available: <https://doi.org/10.1016/j.ijhydene.2020.10.079> (see page 53).

- [62] J. Anacleto and J. M. Ferreira, **On the representation of thermodynamic processes**, *European Journal of Physics*, vol. 36:no. 3, 1–11, ISSN: 13616404. DOI: 10.1088/0143-0807/36/3/035006. [Online]. Available: <http://dx.doi.org/10.1088/0143-0807/36/3/035006> (see page 53).
- [63] *AF/ArmaFlex - Armacell Netherlands*. [Online]. Available: <https://local.armacell.com/en/armacell-netherlands/products/technical-insulation/afarmaflex/> (see page 72).

A

Experimental setup improvements

Based on observations during the experiments, changes were made to the setup. It was chosen to discuss these changes in an appendix to keep [chapter 4](#) readable. This appendix contains an overview of these changes, the original idea behind this implementation and the reason for changing it.

A.1 Hose clamp attachment of thermocouples

In an attempt to measure the wall temperature of the heat exchanger at a certain point, a thermocouple was clamped to the copper pipe using a hose clamp. Another thermocouple would be placed in the bath of water at the same water height. Calculating the difference between these two temperatures would result in the excess temperature. This could relate the measurement results at a certain height to the literature, like the curves presented in [Figure 3.11](#).

From the first tests it became apparent that the attachment of the thermocouple interfered with the boiling behaviour. During tests under subatmospheric conditions bubble formation would only occur under the hose clamp. Nowhere on the uncovered copper vapor bubbles could be observed. [Figure A.1](#) shows a few frames of the bubble formation under the hose clamp.

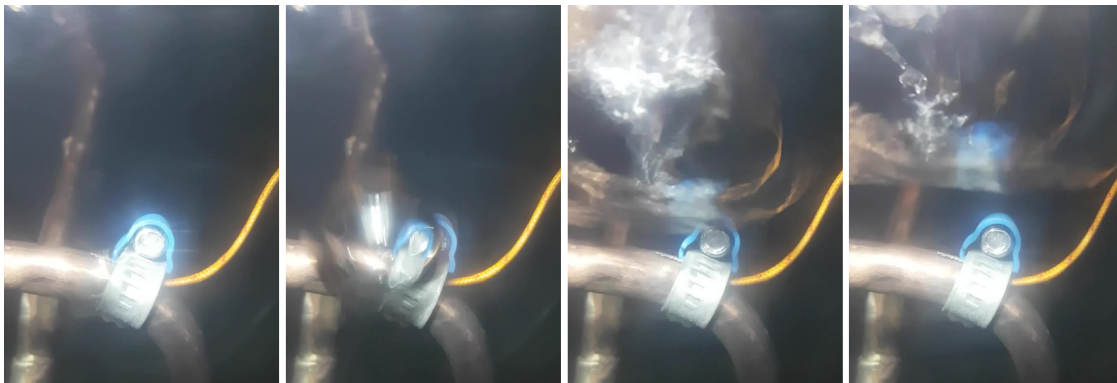


Figure A.1: Vapor bubble formation under the hose clamp. The time difference between the frames is 50 milliseconds.

The hose clamp creates a very narrow gap. It is explained in the theory presented in [subsection 3.4.1](#), that in this narrow gap the fluid will be superheated. The gap will function as a catalyst for bubble formation, because small remainders of vapor will remain behind after the bubble detaches, which are used to form new bubbles.

The conclusion was drawn that the thermocouples could not be attached to the heat exchanger surface without influencing its boiling behaviour. This would make it impossible to extrapolate the measured data over the total heat exchanger, since the boiling is locally improved. Also other attachments of the thermocouple, like soldering, would result in this effect. The solder would create small gaps and imperfections improving the boiling process.

Based on these reasons it was chosen not to measure the heat exchanger wall temperature, but to measure the bath of water at multiple heights. This can give more insight in the stratification of the water that might occur. Estimations of the excess temperature can be made by comparing the average of the inlet and outlet temperature to the bath temperature.

A.2 Upgrading the condenser

The first few experiments were done with a so called "cooling module" as condenser. This "cooling module" is a heat exchanger which was used in other projects to remove leftover fluids from a certain system. By heating the main module and cooling the "cooling module", last bits of fluid will be condensed and collected in the "cooling module". Since the main function of this "cooling module" is condensing it was chosen as the condenser for the experimental setup. This specific configuration is shown in [Figure A.2](#).

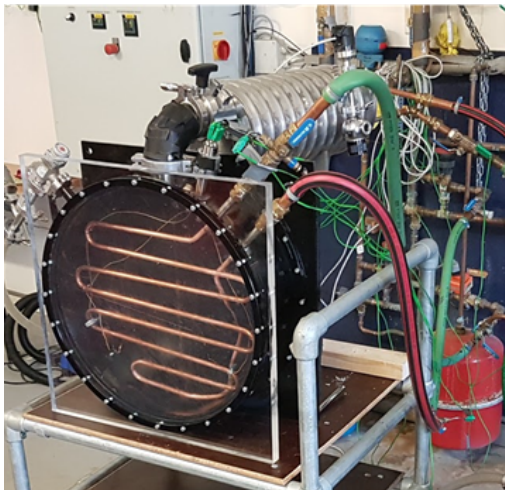


Figure A.2: Picture of the old condenser connected to the setup



Figure A.3: Picture of the new condenser connected to the setup

During the first few tests barely any bubble formation was observed. This is an indication that the temperature difference between heat exchanger and bath temperature is too low. This can have multiple reasons. By increasing the inlet temperature, the amount of bubble formation was increased slightly shortly after opening the valve. After a couple of seconds boiling activity could no longer be observed. In hindsight this boiling was only caused by the reduction of sensible heat of the water. It could be concluded that the capacity of the condenser was too small for the evaporator. An overdimensioned condenser is desired, since this would limit the influence of the condenser on the boiling performance of the evaporator. This makes the different measurement results more comparable. Since changes in boiling behavior are then caused by the evaporator only and not by the interaction between evaporator and condenser.

A condenser with a larger capacity was connected. This specific configuration is shown in [Figure A.3](#). The new condenser consists out of two spiral shaped heat exchangers, which are connected in series. In other projects it was determined that this condenser was suitable for condensing a 7kW -system.

The capacity of the new condenser is far greater than the capacity of the "cooling module". This can easily be concluded from an experimental comparison. The graph in [Figure A.4](#) gives the pressures in the condenser and evaporator for the old and new configuration. The pressure is visualized just before the valve is opened.

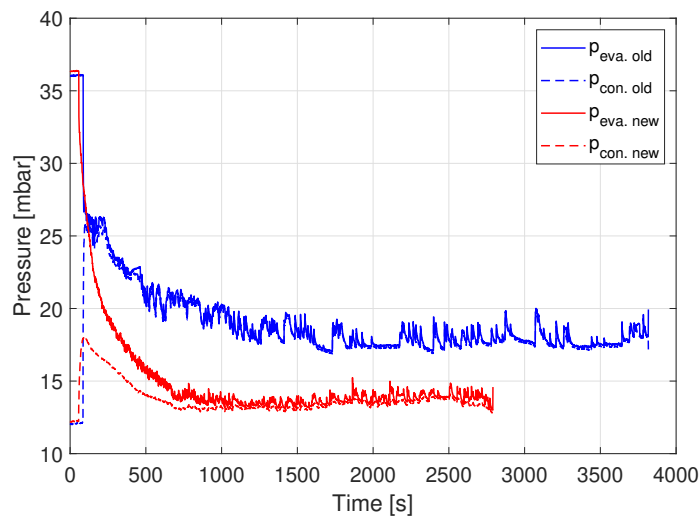


Figure A.4: Figure of the pressure development in the evaporator (solid line) and condenser (dashed line) when the valve is opened. The old configuration is given in blue and the new configuration in red. This data is collected with for the situation where $T_{in} = 30\text{ }^{\circ}\text{C}$ and $z_{start} = 16.9\text{ cm}$.

Two differences can be observed from the pressure development of the two systems in [Figure A.4](#). With the new condenser it takes far longer for the pressure difference between evaporator and condenser to disappear. This means that vapor is transported via pressure driven flow for a considerable period, which is fast. With the old condenser the pressure difference between evaporator and condenser is almost immediately small. This means that the vapor is transported mainly via diffusion, which is slow. Slow vapor transport will limit the formation of new vapor bubbles.

The second difference is the final pressure. Both systems start of at the same pressure. But the final pressure in the system with the new condenser is far lower. This is the result of the far greater condensing capacity, because the condenser is able to condense far more vapor than the evaporator can produce. If the valve is opened the evaporator pressure is drawn towards the condenser pressure. Whereas for the old condenser, the pressures meet somewhere in the middle. A lower evaporator pressure, results in a lower saturation temperature of the water. This will cause the bath temperature around the evaporator to be lower. This results in a larger excess temperature, while the inlet temperature remains the same. With the setup in [Figure A.3](#) higher boiling performances can be obtained without changing the inlet temperatures and the influence of the evaporator is more isolated. The results of the setup in [Figure A.2](#) say more about the interaction between evaporator and condenser, than the evaporator alone.

A.3 Additional isolation of the condenser

Another problem can already be seen in [Figure A.3](#). The hot flow going in and out of the evaporator is flowing through the green and red-black striped hoses. These hoses contact the outer surface of the condenser. The condenser operates at lower temperatures than the evaporator. This means that the hot hoses, connecting the evaporator to the testing environment, will give off heat to the condenser surface. This can be seen as thermal short-circuiting. Part of the heat destined for the evaporator is already absorbed by the condenser, before going in the evaporator. This short circuit will distort the measured powers of both the evaporator and condenser. To combat this effect the condenser is heavily isolated using *ArmaFlex* isolation material. A sheet of *ArmaFlex* is also placed between the two hoses to prohibit contact between the two. *ArmaFlex* is isolation material specifically designed for condensation purposes [63]. [Figure A.5](#) shows the isolated setup. This is the setup which will be used for all the experiments presented in this thesis.

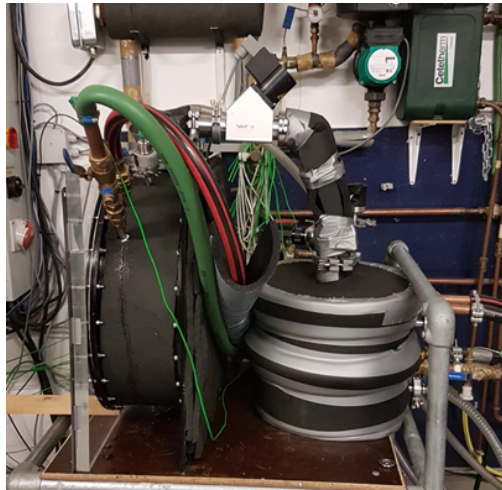


Figure A.5: ArmaFlex-isolation applied to the outer surface and edges of the condenser and vapor connection. Compare to [Figure A.3](#) to see the difference with the previous situation.

B

Finite Element Analysis of PMMA plate configuration

This appendix contains details about the Finite Element Analysis which was performed before building the test chamber assembly for the experimental set up. Based on this analysis it was concluded that the PMMA plate was thick enough and that the construction would withstand the forces caused by the vacuum in the vessel.

B.1 3D Model

SOLIDWORKS is used to do the finite element simulation. An advantage of *SOLIDWORKS*-simulations is that geometries can easily be created and different material properties can be appointed to different parts. A disadvantage is that the user has little influence over the simulation parameters.

For this study a 3D static simulation is performed using tetrahedral solid elements. The von Mises yield criterion is used to determine whether or not plastic deformation will occur in the structure under the stress. The von Mises stress converts stress in three dimensional to a scalar according to [Equation B.1](#).

$$\sigma_{vm} = \frac{1}{\sqrt{2}} \sqrt{[(\sigma_{11} - \sigma_{22})^2 + (\sigma_{22} - \sigma_{33})^2 + (\sigma_{33} - \sigma_{11})^2 + 6\sigma_{12}^2 + 6\sigma_{23}^2 + 6\sigma_{31}^2]} \quad (\text{B.1})$$

With σ_{vm} the von Mises stress (N/m^2). The other stresses are in tensor notation corresponding to the three dimensions 1, 2 and 3.

The von Mises yield criterion states that if the von Mises stress is larger than the yield stress of the material (σ_y) plastic deformation will occur. If the numerical calculated von Mises stress is below the yield stress everywhere, it means that the whole structure is in the elastic regime under the applied stress. In this case failure or plastic deformation is ruled out according to the von Mises yield criterion.

B.2 Problem formulation & Assumptions

Five parts are created in *SOLIDWORKS* closely resembling, the actual geometry of the plate configuration: the top ring with $D_{outer} = 525mm$, $D_{inner} = 496.2mm$ and a thickness of $2.5mm$, the square plate of $560 \times 560mm$ with a thickness of $25mm$ the bottom outer ring with the exact dimensions of the top ring, the bottom inner ring with $D_{outer} = 488mm$, $D_{inner} = 475mm$ and a thickness of $2.5mm$, and the flange with $D_{outer} = 525mm$, $D_{inner} = 475mm$ and a thickness of $8mm$. 24 equally spaced *M5* holes are extruded $255.3mm$ away from the centre. These holes are used to bolt the assembly.

The linear elastic material properties of stainless steel are appointed to the rings and flange. The linear elastic material properties of acrylic are appointed to the plate. The connected assembly according to the model is visualized in [Figure B.1](#). The fixed constrain is placed on the bottom surface of the flange. This is in close alignment with the actual situation. A pressure load is placed on the surface of the PMMA-layer encircled by the top ring. The pressure which is placed on this surface is 0.1013MPa which is exactly 1 atm . A fine mesh consisting out of roughly 179.000 elements is created. Elements of the rings and near the holes are locally refined. The mesh is visualized in [Figure B.2](#).

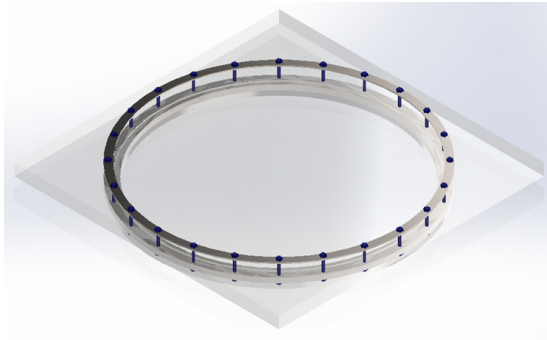


Figure B.1: Assembly with realistic colours

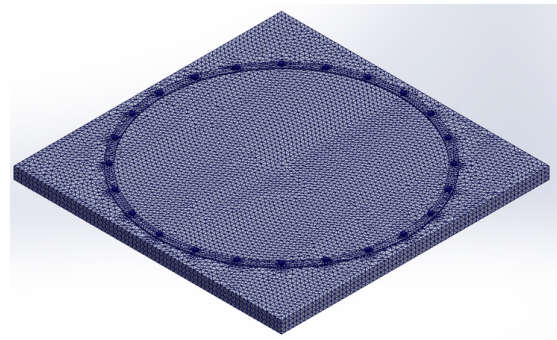


Figure B.2: Mesh of the assembly

There are three main differences between the assembly as seen in [Figure B.1](#) and the real configuration. In reality there is actually a rubber ring covered in vacuum grease between the bottom inner and outer ring. Since this will contribute little to the strength of the assembly, the rubber ring is not modelled. The second difference, is the hole sizes. In reality the holes are 6mm wide instead of 5mm . M5 bolts, with washers on both ends, are bolted in M6 holes. This is because there were no tools available to drill the holes so precisely that they would line up exactly. In this case a clearance fit is preferred over an interference fit. The third difference between model and real situation is the pressure applied on the plate. In the model it is assumed that there is an absolute vacuum in the vessel. A vacuum up to 4 mbar can be achieved. When water is present the water temperature will determine the pressure in the vessel and due to the hydrostatic pressure this pressure will also vary over the water height. But a higher pressure than is currently modelled can never be applied to the PMMA plate in reality.

B.3 Results & Conclusion

The deformation of the PMMA plate is visualized in [Figure B.3](#) and [Figure B.4](#). This is completely in line with the expectations. The center of the plate will displace furthest, and the part of the plate which is not in contact with the vacuum will barely deform. Although the ends of the plate are curled upwards slightly.

[Table B.1](#) contains the summary of the numerical static analysis per part. The maximum numerical von Mises stresses per part are compared to the yield stress of the material it is made from. In all parts the von Mises stress is far below the yield stress. This means that only elastic deformation will take place when there is a vacuum inside the vessel. This FEA concludes that no plastic deformation or failure will occur, when the inside of the vessel is in a vacuum.

Table B.1: Results of the numerical stress study compared to the yield stress per part

| Part | Maximum numerical von Mises stress (MPa) | Yield stress (MPa) | Percentage (%) |
|-------------------|---|---------------------------|-----------------------|
| Top ring | 85.6 | 292 | 29 |
| PMMA plate | 13.9 | 45.0 | 31 |
| Bottom outer ring | 151 | 292 | 52 |
| Bottom inner ring | 59.9 | 292 | 21 |
| Flange | 29.1 | 292 | 10 |

The highest stresses in the assembly occur in the bottom outer ring. This is visualized in [Figure B.5](#). The high stresses occur on the outside of the ring due to the high shear forces that occur there. The stress distributions of the bottom outer ring are very different from the top ring which has the exact same geometry. The stresses in the top ring are shown in [Figure B.6](#). This figure shows stress concentrations, which are typical around holes: high stresses in the direction of the force and low stresses perpendicular to the force.

The highest strains in the assembly occur under the PMMA layer. This is shown in [Figure B.7](#). Where the PMMA layer is pressed against the bottom inner ring high shear forces occur. PMMA has a much lower tensile strength than stainless steel. Resulting in high strain in the PMMA layer. Logically this is the same location where the highest stresses occur in the PMMA layer, as can be seen in [Figure B.8](#).

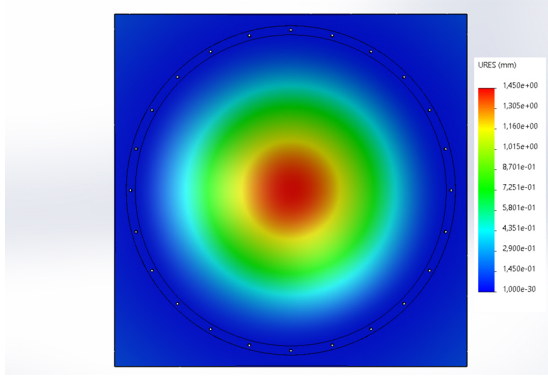


Figure B.3: Surface plot of displacement top view

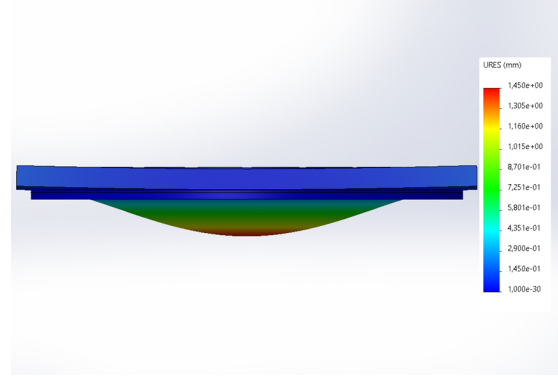


Figure B.4: Side view of deformation (scale: 39:1)

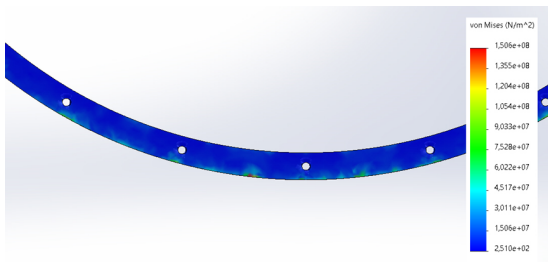


Figure B.5: Stress distribution on bottom ring

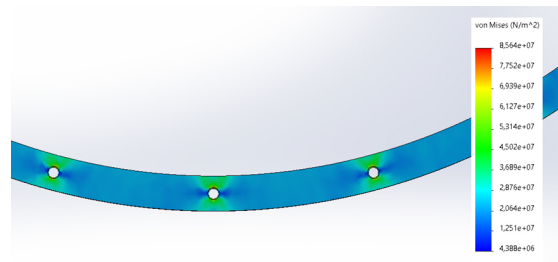


Figure B.6: Stress distribution on top ring

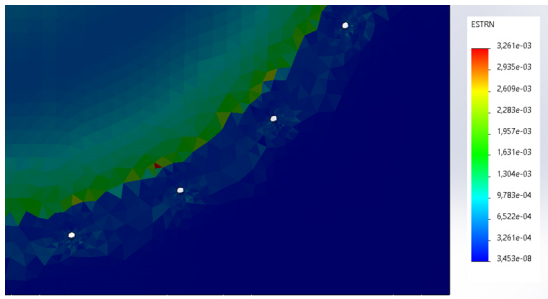


Figure B.7: Strain under PMMA plate

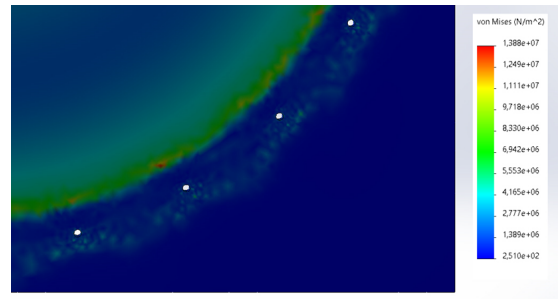


Figure B.8: Stress under PMMA plate

C

Heat exchanger area model

Because the heat exchanger has a rather complex shape, no mathematical expression can be constructed to relate the height of the water to the surface area of the heat exchanger. To calculate the heat flux and compare the boiling performance at different water heights the surface area of the heat exchanger is needed. An image recognition program was created using *MATLAB*, which will estimate the surface area based on pictures of the heat exchanger. This appendix will present the method which is used to create the relation between water level height and surface area and volume of the heat exchanger.

C.1 Preprocessing

This model will convert an image into information how much surface area is present at a particular height. The program will do this by counting and adding the number of surface area pixels at a certain height. To do this a clear distinction needs to be made between pixels belonging to the surface and pixels belonging to the background. A number of filters are applied to the original photo, to enhance the contrast between the heat exchanger and the background. Lastly the light spots on the heat exchanger due to the reflection of light are manually coloured. [Figure C.1](#) shows the original image. [Figure C.2](#) shows the black and white image after processing. This image is then rotated to fit an image of the final setup to make sure the image is saved at the correct angle.

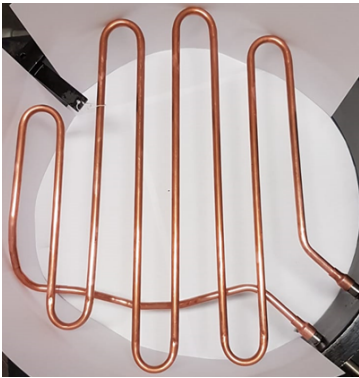


Figure C.1: Picture of the heat exchanger mounted in the vessel

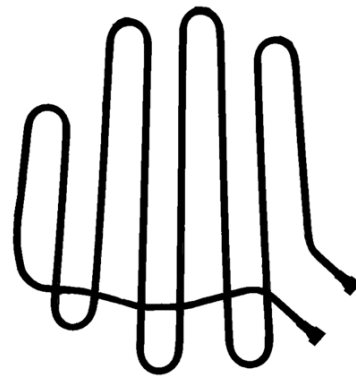


Figure C.2: Black and white image of the heat exchanger, made using photo editing software

C.2 Converting image in data

The model converts the images as seen in [Figure C.2](#) into a 256 bit grayscale image. This image is then converted in a binary image only consisting out of ones and zeros. The ones take the place of the heat exchanger pixels and the zeros are where there is no heat exchanger. The pixels in y-direction are then added per pixel in the x-direction. This is visualized in [Figure C.3](#). The x-direction in the image is the same direction as the height for the real heat exchanger. Note that there are regions where the heat exchanger overlaps. This will require compensation later on.

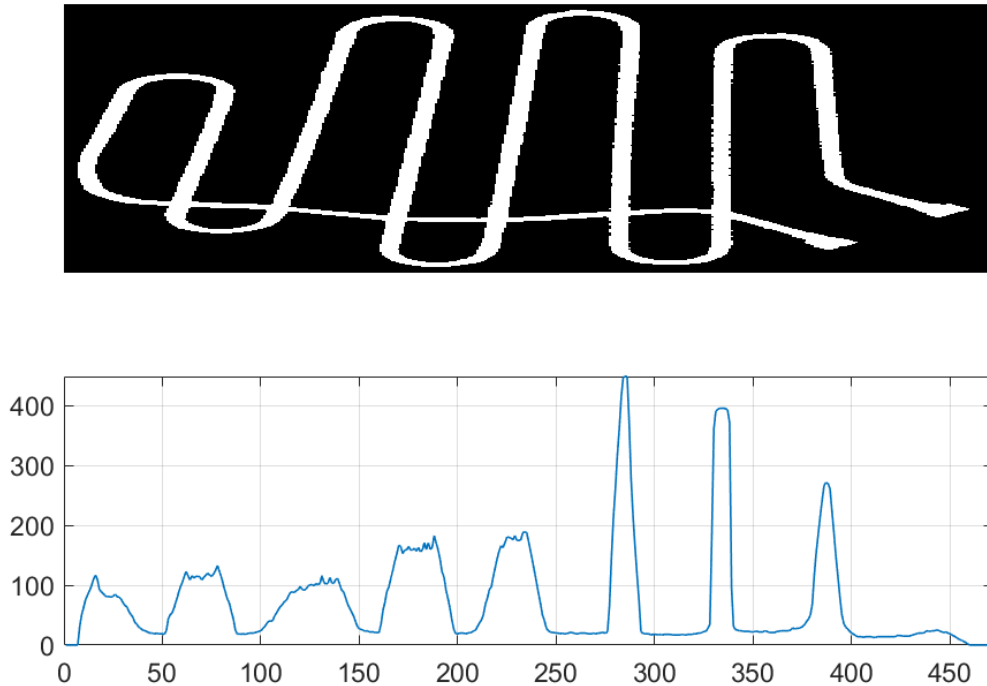


Figure C.3: Above: the binary image of the heat exchanger. Below: the summation of the white pixels in y-direction per pixel in x-direction.

The diameter of the pipe is 10mm and the average distance between the pipe centres is measured to be 49.03mm using a caliper. The total pipe length out of which the heat exchanger is constructed is 3.38m . These length units will be used to scale the pixel distribution as visualized in [Figure C.3](#).

A window smaller than the average distance between the pipe centres is defined. Using a local maxima finder function the positions of the pixel peaks are found within the defined window. It is assumed that these peaks correspond to the middle of the vertical pipes. The distance between these peaks is calculated and averaged. The distance between the peaks in the pixel domain is now known. The distance between the pipes of the real heat exchanger is known to be 49.03mm . Using these two values a ratio between the pixel domain and the real world can be made. By multiplying this ratio with the pixels in x direction the domain will be converted into millimeters instead of pixels.

The total length which overlaps in the image is assumed to be 6 times the pipe diameter, which is 60mm . It can be seen in [Figure C.2](#) that this is a reasonable assumption. An overlap function is created which consists out of 6 rectangular blocks which are 49.03mm apart and 10mm wide.

Using the equation for the lateral surface area of a cylinder, as seen in Equation C.1, the amount of overlap surface area can be calculated. The overlap function can now be scaled, such that the total area under the curve equals the calculated overlap surface area.

$$A = \pi DL \quad (C.1)$$

With A the surface area (m^2), D the pipe diameter (m) and L the pipe length (m).

The same approach is used for scaling the visible area curve. The visible length of heat exchanger equals $3.32m$. Using the equation for the lateral surface area of a cylinder given in Equation C.1. The pixel curve given in Figure C.3 can now be fitted such that the area under the curve equals the calculated visible area. The distributions of the overlap area and the visible area are visualized in Figure C.4. By adding these two curves the total area distribution is calculated. This gives a relation between the height and the area of the heat exchanger. Using cumulative trapezoidal numerical integration the total area of the heat exchanger can be estimated for every height.

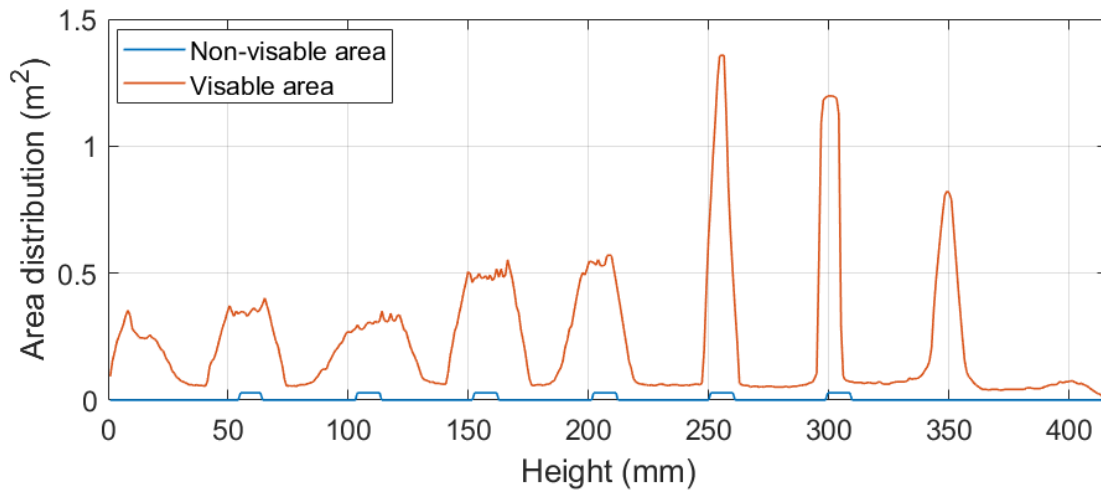


Figure C.4: Scaled area distribution of the overlapping area (blue) and the visible area (red). The sum of the two gives the real area.

Note that using the same scaling methods an expression for the heat exchanger volume per height can be calculated. Instead of using Equation C.1 to determine the scale factor for the curve of Figure C.3, the curve is scaled to the total volume. The volume can be calculated using the expression of a cylinder as given in Equation C.2.

$$V = \frac{1}{4}\pi D^2 L \quad (C.2)$$

With V the volume of the heat exchanger (m^3).

The heat exchanger volume per height can be used to calculate the amount of liquid present in the vessel at a certain height more accurately. The relation between height and volume of a cylindrical test vessel, depicted in [Figure 4.2](#), can be calculated using the expression in [Equation C.3](#).

$$V(z) = \frac{1}{4}D^2L \arccos\left(\frac{D-2z}{D}\right) - \left(\frac{1}{2}D - z\right)\sqrt{Dz - z^2} \quad (\text{C.3})$$

With D the diameter of the cylindrical vessel (m), L the length of the cylindrical vessel (m) and z the height (m).

By subtracting the heat exchanger volume per height relation from the vessel volume calculated by [Equation C.3](#), the amount of water can be determined more accurately.

C.3 Combining multiple data sets

To improve the precision of the relation between surface area and height multiple photos are taken of the heat exchanger like the one in [Figure C.1](#). A total of 8 pictures were deemed suitable. This means that 8 curves like the one presented in [Figure C.4](#) were constructed. By combining these curves errors are averaged out and the relation becomes more accurate. A separate *MATLAB* script is written to collect and combine the different data sets.

All 8 photos go through the previously described process. This will give 8 area distribution curves, like the one presented in [Figure C.4](#). These curves and the peak locations are saved in data files, which can be loaded by another *MATLAB* script. All these data files are then loaded. All peak locations are collected in one big matrix. The peak locations are now averaged. This results in the average location of the 9 peaks. Each curve is then shifted by an individual offset which is determined via a regression algorithm. This way the peaks of all curves align best with the average peak locations. A visualization of all 8 aligned area curves is given in [Figure C.5](#). These peaks are averaged. This average curve is then scaled again to make sure that the area under the curve equals the surface area calculated using [Equation C.1](#) with the total length of the pipe. This will lead to the final curve which is presented in [Figure C.6](#). To get the total surface area for a certain height, this curve needs to be numerically integrated.

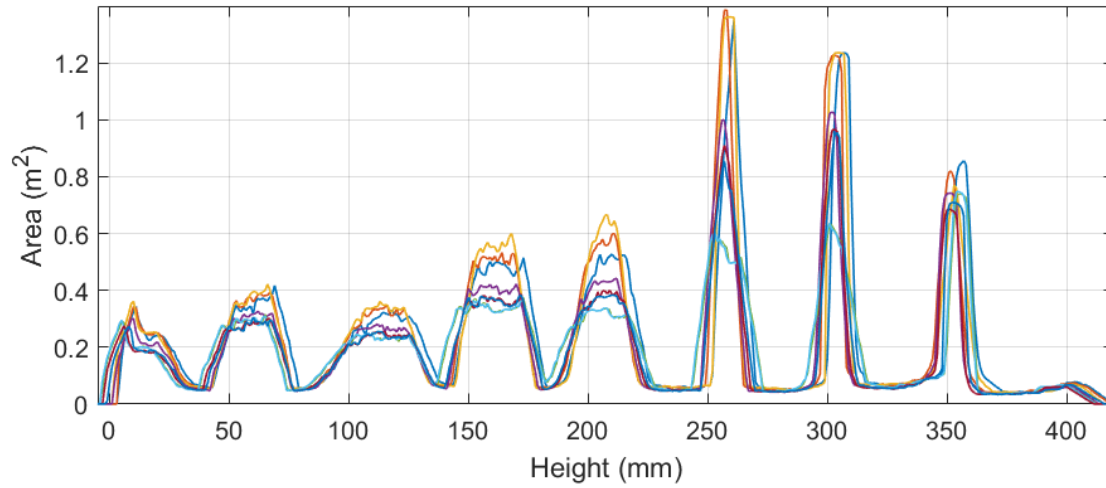


Figure C.5: Area vs height curves for all 8 images. The curves are all shifted slightly to better match the average peak locations

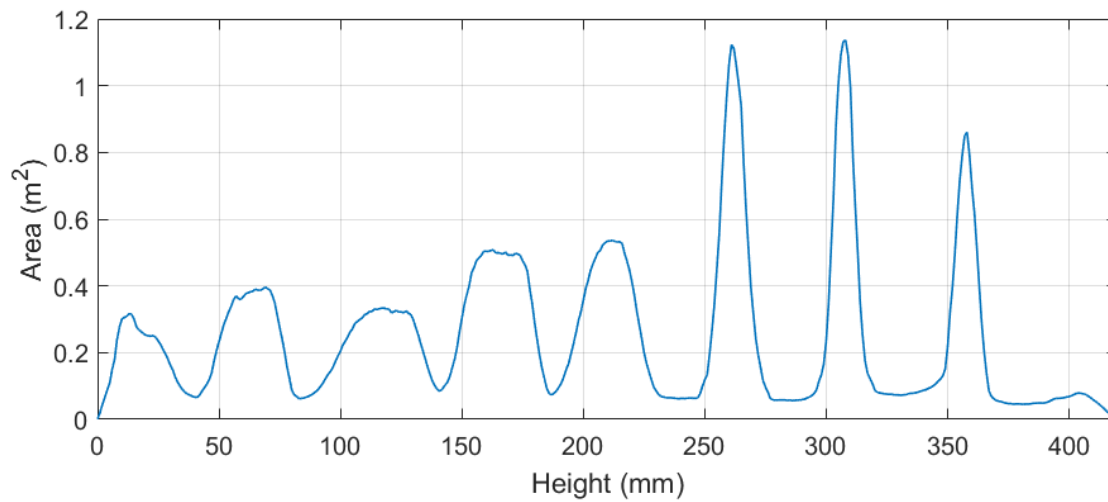


Figure C.6: Shows the final curve for surface area distribution against the height

D

Distributions of evaporator power

This appendix contains evaporator power distributions obtained during the steady regime of the experiments with the two dimensional heat exchanger (visualized in [Figure 4.3](#)). During the steady regime there are fluctuations in the power transferred between the heat exchanger and the water. The [Figures D.1 to D.8](#), all for different starting water heights (z_{start}), contain a histogram in blue. In this histogram the powers of one particular steady regime experiment are split up in 20 bars. On the left y-axis the frequency of every bar in the histogram is given. On the right y-axis in red, the probability density of the raw data is given. The probability distribution is constructed using a Epanechnikov kernel method. It can be seen that many figures cannot accurately be described by a normal distribution. Instead a bimodal distribution seems to fit much better for most steady regime power data.

The reason that the power in the steady regime can be described by a bimodal distribution is most likely caused by the subatmospheric boiling behaviour already seen in [Figure 3.11](#): The amount of heat transfer to the vapor bubble is relatively low, but when the vapor bubble detaches, cold water fills its place and the heat transfer is high. This will result in two modes for the heat exchanger power in the steady regime.

In the evaporator during the experiment two boiling phenomena are occurring: nucleate pool boiling and convection pool boiling. As explained the nucleate pool boiling could be responsible for the bimodal distribution. The steady regime convection pool boiling process can be categorized by a normal distribution. Fluctuations in inflow temperature and local bath water temperature will cause fluctuations in power, but these will on average cancel each other, resulting in a symmetrical normal distribution. Because both boiling phenomena are observed during the experiments. The [Figures D.1 to D.8](#) are assumed to be a combination of the bimodal and the normal distribution.

In [section 5.4](#) it was mentioned that nowhere deeper than 5.8cm under the water surface nucleate pool boiling was observed. So by increasing the water height the amount of water which takes part in convection pool boiling relatively increases. This theory is substantiated by the evaporator power distributions. The red kernel distributions of [Figures D.1 to D.5](#) (initial water heights from 6.6 to 19.0cm), appear to contain a bimodal distribution. While the distributions for higher water levels in [Figures D.6 to D.8](#) (initial water heights from 23.4 to 26.7cm), appear to be dominated by a normal distribution.

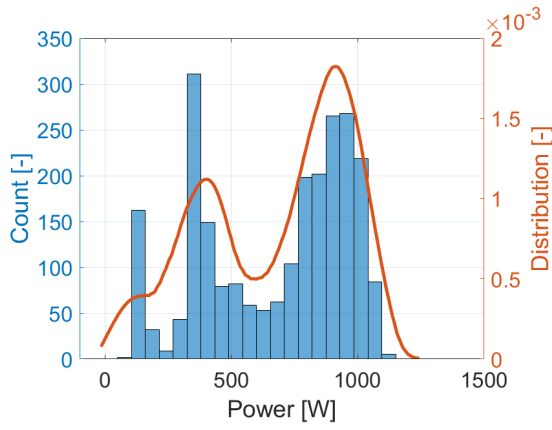


Figure D.1: Power distribution for $z_{start} = 6.6\text{cm}$

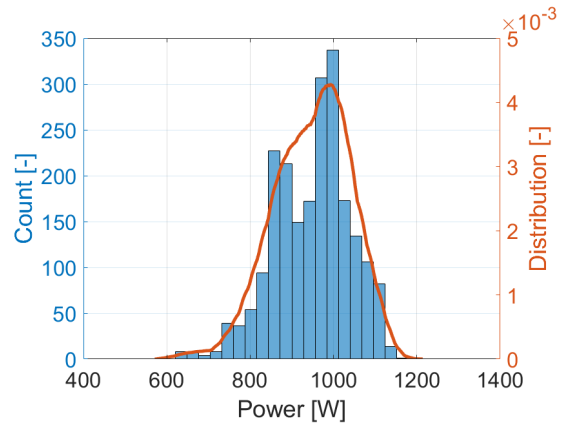


Figure D.2: Power distribution for $z_{start} = 8.5\text{cm}$

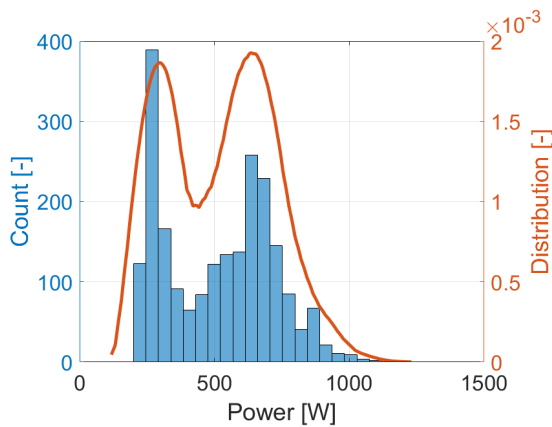


Figure D.3: Power distribution for $z_{start} = 15.3\text{cm}$

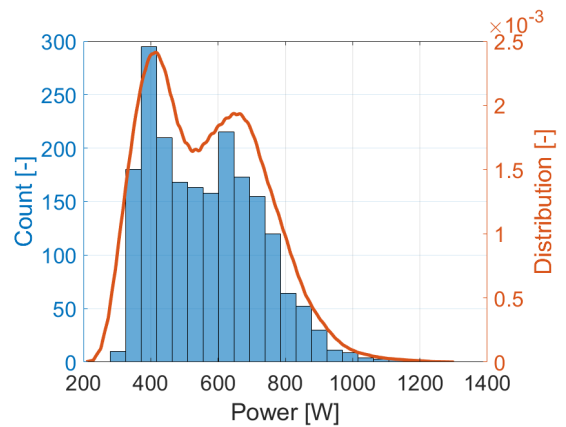
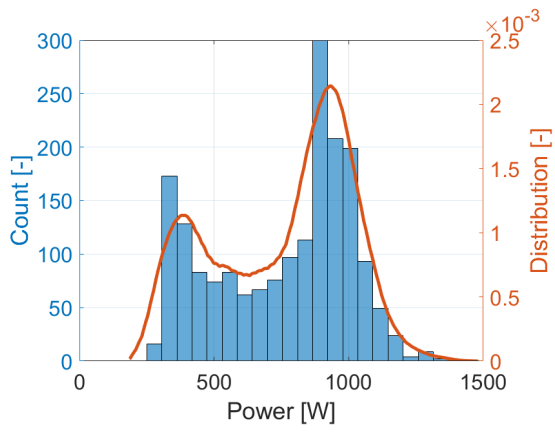
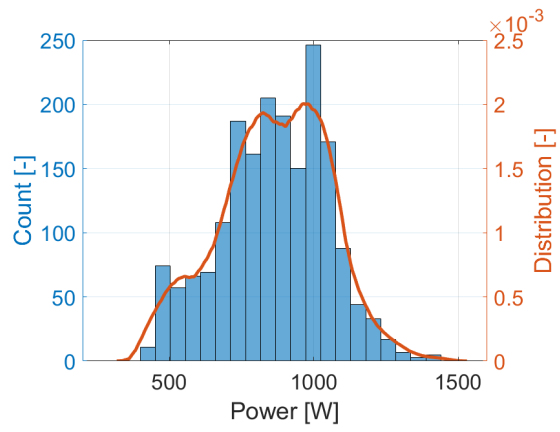
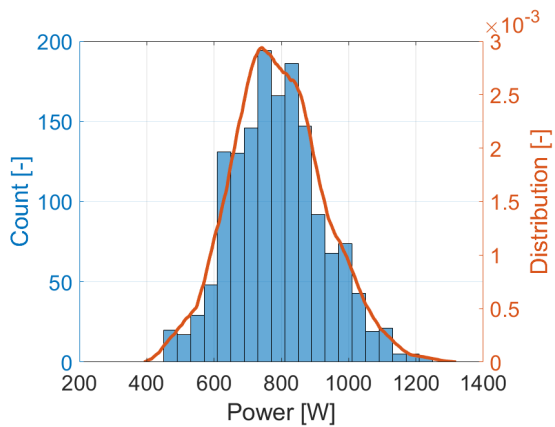
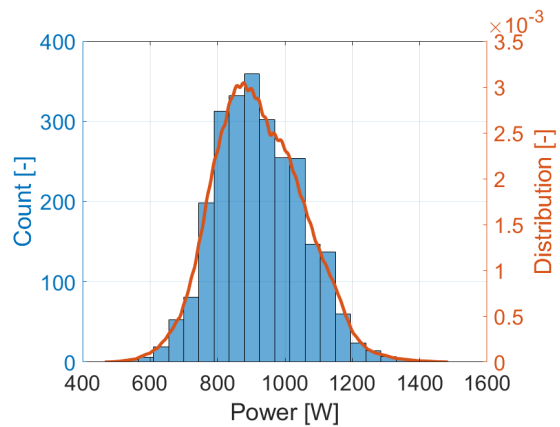


Figure D.4: Power distribution for $z_{start} = 16.9\text{cm}$

Figure D.5: Power distribution for $z_{start} = 19.0\text{cm}$ Figure D.6: Power distribution for $z_{start} = 23.4\text{cm}$ Figure D.7: Power distribution for $z_{start} = 24.2\text{cm}$ Figure D.8: Power distribution for $z_{start} = 26.7\text{cm}$

E

Influence of approximated parameters on numerical model

As seen in [subsection 6.2.2](#) the analytical model contains 3 parameters which need to be approximated to relate the model to the experiments. These parameters are: the volumetric mass transfer intensity factor β_e , the relaxation time τ and the steady state pressure difference Δp_{steady} .

E.1 Pressure difference

The pressure difference can easily be found from the experiment data. [Figure E.1](#) contains the experimental results for pressure difference as a function of time in blue. Eventually this pressure difference settles at a steady state value, indicating the end of the transient regime. The pressure difference between the two chambers is assumed to be mainly due to the pressure drop over the valve and pipe connection. The average value of the pressure difference in the steady regime was found to be 0.5mbar . This is the value which will be used as Δp_{steady} in the computations. This parameter is assumed to be constant by the assumptions given in [subsection 6.2.2](#). While in reality it is likely to be higher when the valve has just opened because of the higher vapor flux, so a higher pressure drop. $\Delta p_{steady} = 0.5\text{mbar}$ will be used for all simulations.

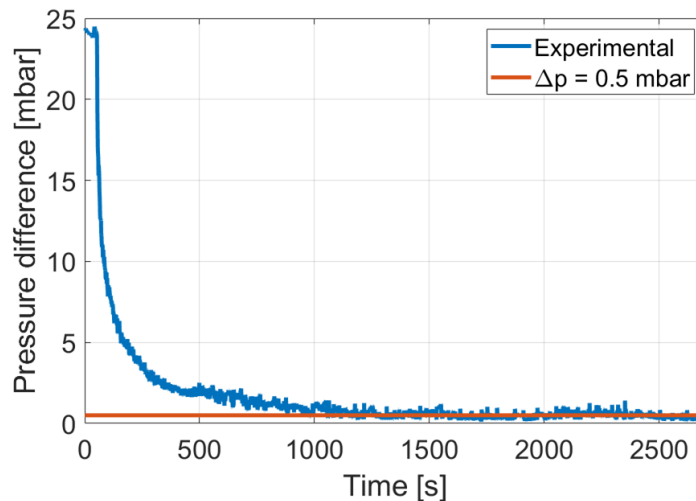


Figure E.1: Experimental data for the pressure difference between evaporator and condenser in blue. In red the average pressure difference in the steady regime.

E.2 Mass transfer intensity factor

[Figure E.2](#) shows a plot for the numerically calculated output power for different values of β_e . This figure also contains the experimental value in black. It can be seen in [Figure E.2](#) that with increasing β_e the output power increases. At $\beta_e = 0.001\text{m}^3/\text{s}$ the solution has become numerically unstable. After some further simulations it was found that for $\beta_e = 9.0 \cdot 10^{-5}\text{m}^3/\text{s}$ the numerical results resembled the experiment the most. This value is used for all simulations.

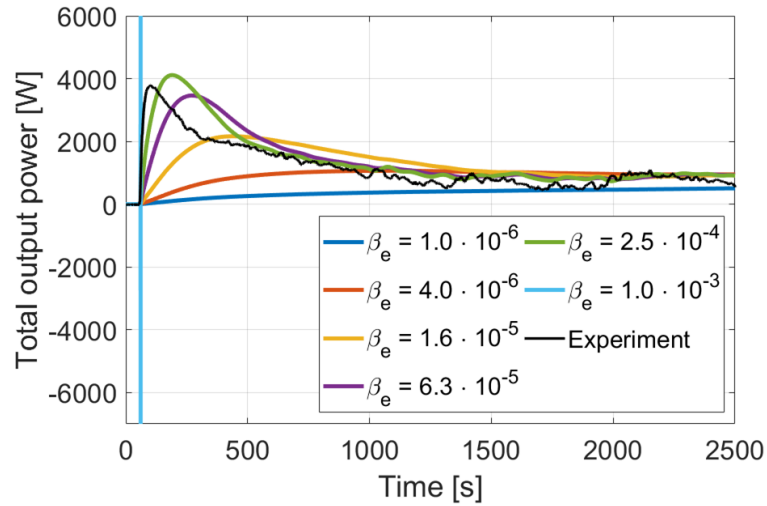


Figure E.2: Numerical results for the output power with different values for β_e , with in black the experimental result.

E.3 Relaxation time

Figure E.3 shows a plot for the numerically calculated output pressure for different values of τ . This figure also contains the experimental value in black. In Figure E.3 it can be seen that with increasing relaxation time the evaporator pressure decreases slower. At $\tau = 500$ s the evaporator pressure even slightly increases at the start. More simulations were done and it was found that for $\tau = 150$ s the numerical result represents the experimental result the most. This value is used for all simulations.

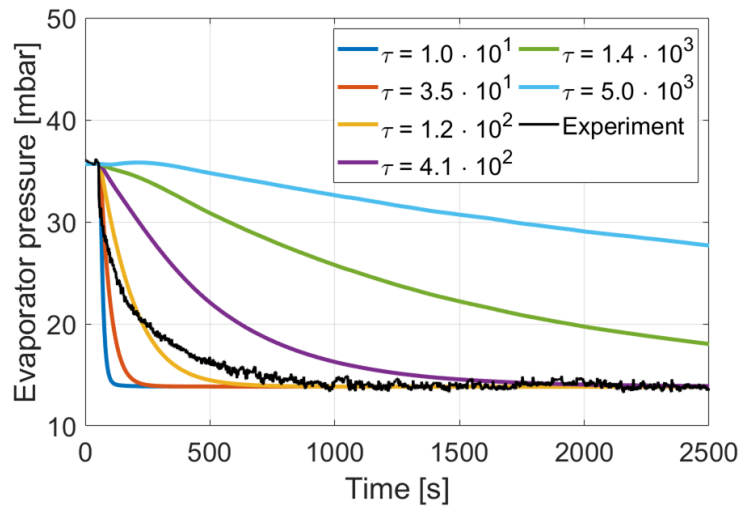


Figure E.3: Numerical results for the evaporator pressure with different values for τ , with in black the experimental result

Declaration concerning the TU/e Code of Scientific Conduct

I have read the TU/e Code of Scientific Conductⁱ.

In carrying out research, design and educational activities, I shall observe the five central values of scientific integrity, namely: trustworthiness, intellectual honesty, openness, independence and societal responsibility, as well as the norms and principles which follow from them.

Date

19-05-2021

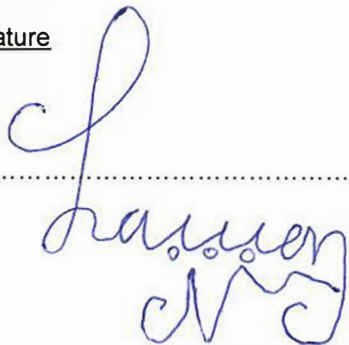
Name

Nicolaas Jacques Laumen

ID-number

0999222

Signature



Submit the signed declaration to the student administration of your department.

ⁱ See: <https://www.tue.nl/en/our-university/about-the-university/organization/integrity/scientific-integrity/>

The Netherlands Code of Conduct for Scientific Integrity, endorsed by 6 umbrella organizations, including the VSNU, can be found here also. More information about scientific integrity is published on the websites of TU/e and VSNU